Development of frequency division multiplexing readout for a large transition edge sensor array for space

Wang, Qian

DOI:
10.33612/diss.193636081

rijksuniversiteit
groningen

Development of frequency division multiplexing readout for a large transition edge sensor array for space

Proefschrift

ter verkrijging van de graad van doctor aan de
Rijksuniversiteit Groningen
op gezag van de
rector magnificus prof. dr. C. Wijmenga
en volgens besluit van het College voor Promoties.

De openbare verdediging zal plaatsvinden op

vrijdag 10 december 2021 om 12.45 uur

door

Qian Wang

geboren op 4 maart 1992
te Shandong, China

Promotor
Prof. dr. F.F.S. van der Tak

Copromotor
Dr. J.R. Gao

Beoordelingscommissie
Prof. dr. M. Dobbs
Prof. dr. G. Steele
Prof. dr. B. Jayawardhana

Dr. P. Khosropanah heeft als begeleider in belangrijke mate aan de totstan dkoming van het proefschrift bijgedragen.

Keywords: infrared astronomy, transition edge sensor, superconducting quantuam interference device, multiplexing, space telescope

Printed by: Gildeprint

Cover: Design from the insight of the similarity between frequency division multiplexing and cars in highway, draw by my wife Yuner.

To the people I love & To the days in the Netherlands...

Contents

Chapter 1
Introduction

In this chapter, the background of far-infrared astronomy as the scientific motivation of this thesis is briefly introduced in section 1.1. An overview of direct detection techniques and an introduction to transition edge sensors (TES) are given in section 1.2. The three most promising multiplexing techniques for TES arrays are described in section 1.3. Finally, the structure of this thesis is highlighted in Section 1.4.

1.1 Far-infrared astronomy

Far-infrared (FIR) radiation, defined usually as wavelengths between 30 and 300 μm or the frequencies between 1 and 10 THz, is used by astronomers to investigate and understand the origins of planets, stars, and galaxies [1-3]. In the night sky, William Herschel and Bart Bok have observed dark patches where starlight is obfuscated, which show the effect of dust in our Galaxy. The dust grains absorb and scatter starlight at ultraviolet (UV) and optical wavelengths. However, the FIR blackbody radiation is from the dust itself. Because FIR has a long-wavelength, thus, a low photon energy, which means no absorption, but emission from dust.

The FIR range contains an extremely abundant and diverse cluster of characteristic features, the most important of which are [2,3]:

(1) Atomic fine structure lines emission and absorption from the interstellar medium (ISM), the most prominent examples being [OI], [NII], [CI], [CII], as well as [OIII];

(2) Molecular gas features, especially CO, H_2O, etc, and gas that are unique to the FIR range like HD;

(3) Absorption and emission features which come from original and processed ices, as well as crystalline silicates;

(4) Continuous emission and absorption from dust grains with a temperature between ~15 K and ~100 K. The dust is heated by ultraviolet starlight while it cools through thermal emission in the FIR.

The diagnostic value of the FIR radiation makes it useful to understand a wide range of cosmic questions, among which the history of galaxies and the origins of stars and planets are attractive and important [3]. In particular, star formation is one aspect of the baryon cycle in galaxies, which is a key aspect of galaxy evolution [4-6].

The investigation of the ISM can help us understand the above questions since the ISM includes cool gas and dust between the stars, which emit mostly FIR photons. Astronomers observe FIR photons from the ISM to study its life cycle, which includes the information of forming stars. As shown in Fig. 1.1, the life cycle of gas in galaxies can be divided into five phases, each of which plays a role in the formation of galaxies and stars [4,5].

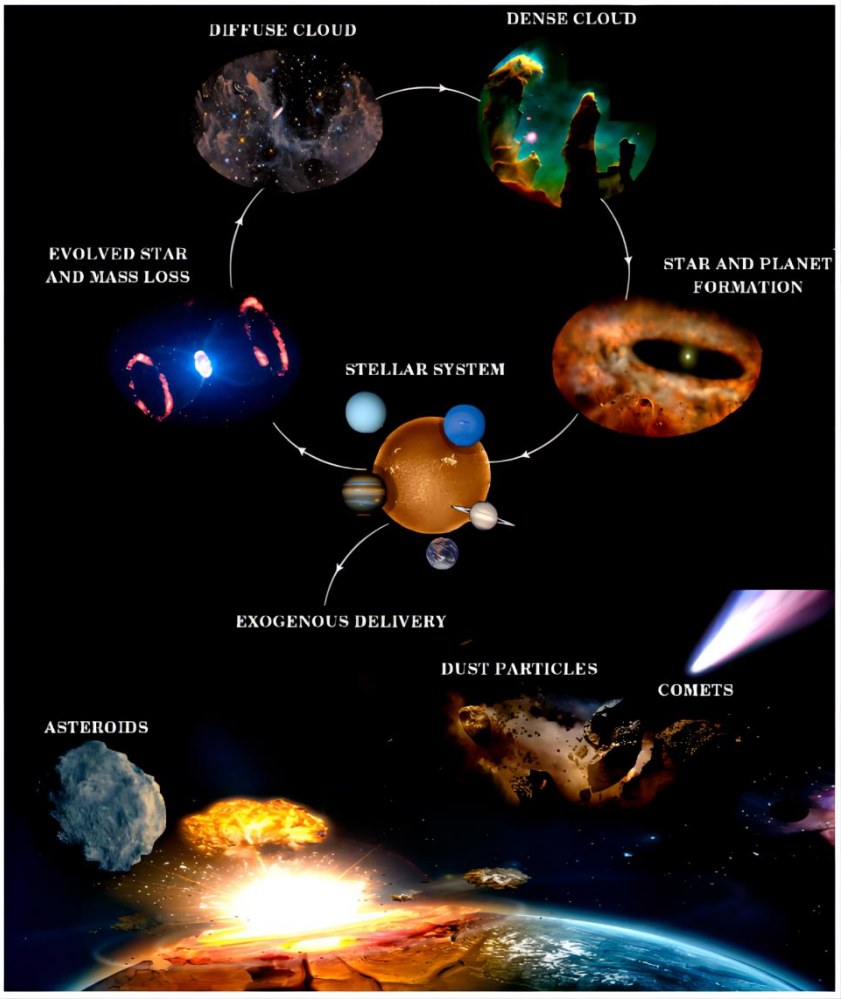

Fig. 1.1 The cycle of gas in galaxies from interstellar clouds to stars and planets (Figure courtesy of G. A. Cruz Díaz using NASA images). We can utilize FIR radiation to study the life cycle of gas in galaxies by detecting molecular rotational lines to get the information we need to answer fundamental questions of modern astronomy.

Since the Earth's atmosphere is opaque to FIR radiation, space-based observations are required, motivating the development of FIR space

telescopes. The capabilities of the next generation of FIR instrumentation could be largely enhanced by combining a large and cold telescope with instruments employing state-of-the-art sensitive detectors [7]. For example, by taking advantage of the cold telescope (~8K) with a low emissivity (~0.01%), the SPace Infrared telescope for Cosmology and Astrophysics (SPICA) mission (planned until 2020) is capable of detecting radiation in the sky-limited background, aiming to achieve extraordinarily high sensitivity. Such a cold telescope can achieve at least two orders of magnitude with better sensitivity than what has been reached to date as shown in Fig. 1.2, creating significant new possibilities for FIR astronomy [7,8]. Although the SPICA mission has been cancelled, the frequency division multiplexing (FDM) technology that is described in this thesis could be used in other FIR space telescopes as well as those in other wavelengths. For example, the Lite satellite for the studies of B-mode polarization and Inflation from cosmic background Radiation Detection (LiteBIRD) [9] is a cosmic microwave background (CMB) telescope that is being developed now. FDM is the technology to read out about 4000 TES bolometers operating within a frequency range between 40 and 400 GHz, requiring a multiplexing factor of 68 (68 pixels read by one superconducting quantum interference device (SQUID)-based channel). The operating frequencies for the LC filters are planned to be 1-5 MHz. In addition, the recently released US decadal survey describes TES together with SQUID-based readout as a potential technology for Origins Space Telescope (OST) or the flagship mission [10].

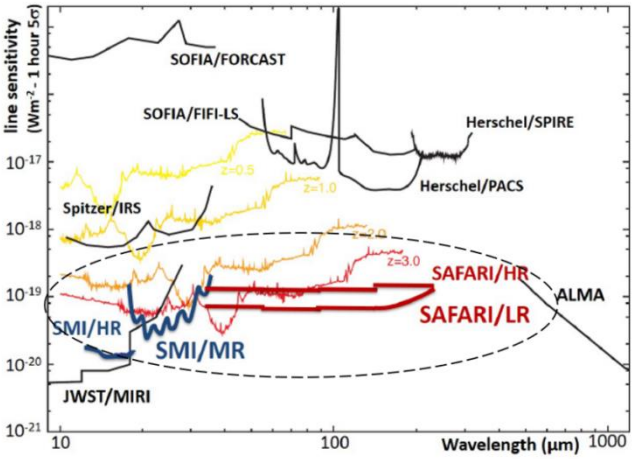

Fig. 1.2 The sensitivity comparison of the SPICA instruments (inside black dashed circle) with other infrared facilities [7]. Those facilities are space-based observations, for example, Herschel was a space telescope covering the far infrared and submillimeter waveband. The sensitivity of SPICA/SAFARI is 100 times greater than that of the Herschel space telescope.

1.2 Direct detection

We can use FIR detectors to detect radiation from our galaxy and other galaxies, which is critical to answer fundamental questions in modern astronomy [3,7]. There are two types of detection techniques: heterodyne detection, which means not only the radiation signal but also the spectral and phase information are detected. Heterodyne detection naturally achieves a very high spectral resolution (R) of $\geq 10^6$, but also suffers from the sensitivity limitation due to quantum noise [1]. Therefore it is usually used for the FIR observations of our Milky Way and nearby galaxies. Direct detection, which means the incident radiation power will be detected by a detector without spectral and phase information. It has some advantages over heterodyne detection with respect to the sensitivity and the pixel number, or the sensitivity and the field of view. Direct detectors, unlike the presence of quantum noise in heterodyne detection, can have extremely high sensitivity, characterized by the Noise Equivalent Power (NEP). Their sensitivity is often limited by the background noise of a warm telescope. Therefore, direct detection in combination with a cold telescope is the choice to detect, for example, the FIR radiation from distant galaxies, where the FIR radiation received by the telescope is extremely weak. This section describes three types of direct detectors that can measure low radiation power.

Three types of direct detectors are under development: superconducting transition edge sensors (TESs) [11,12], kinetic inductance detectors (KIDs) [13, 14], and quantum capacitance detectors (QCDs) [15,16]. The first two are more mature. For example, TES detectors have been used in Submillimetre Common-User Bolometer Array 2 (SCUBA-2) on the former James Clerk Maxwell Telescope (JCMT) [17], KIDs are being used in the New IRAM KID Array (NIKA) on the Institut de RadioAstronomie Millimétrique (IRAM) [18]. The next sections describe these detectors in more detail.

1.2.1 Brief introduction to KIDs and QCDs

KIDs are based on the sensitivity of the surface inductance of a superconducting film to the absorbed electromagnetic radiation power through the phenomenon of Cooper pair breaking. The detection processes of KIDs are shown in Fig. 1.3 [13]:

(a) Photons are absorbed in the superconducting film operated below its transition temperature, breaking Cooper pairs to create quasi-particles or electrons;

(b) The detector is essentially based on an LC resonator circuit, where the kinetic inductance can be changed by the absorbed photons;

(c) A dip is produced in the transmission of the LC circuit at the resonance frequency. This resonance is shifted to a lower frequency and its amplitude is reduced due to the change of the inductance and due to the presence of the dissipative electrons;

(d) It also produces a phase shift of a microwave probe signal transmitted through the circuit.

KIDs are suitable to form a large array because of their easy readout. Although KIDs apply frequency multiplexing similar to what has been developed for TES (the main topic of this thesis) they operate in the microwave GHz frequencies in combination with a wideband low noise amplifier (LNA). The latter allows for a high multiplexing factor of ~1000 pixels/per LNA. KIDs have progressed rapidly and have been used on several ground-based instruments [13] such as the Multicolor Submillimeter Inductance Camera (MUSIC) on a Sub-millimeter Telescope Caltech Submillimeter Observatory (CSO) in Hawaii. The sensitivities of KIDs are comparable with TES and have been fabricated in a larger array (more than 1000 pixels). Now the sensitivity of KIDs in a kilo-pixel array reaches an NEP of $\sim 3\times10^{-19}$ W/$\sqrt{\text{Hz}}$ [19]. However, for space applications, a few wide band LNAs (4-8 GHz) with sufficiently high gain (≥30 dB) may need a cooling power of > 4 mW at the 4K stage, which is still a challenge [20]. The total power dissipation is expected to be dozens of μW for thousands of TES using SQUIDs at 4K stage. KIDs have never been selected for a space mission, whereas TES bolometers have, therefore KIDs are considered as less mature than TES technology. The latter, for example, is the technology, indicated for the proposed National Aeronautics and Space Administration (NASA) space mission of OST [2].

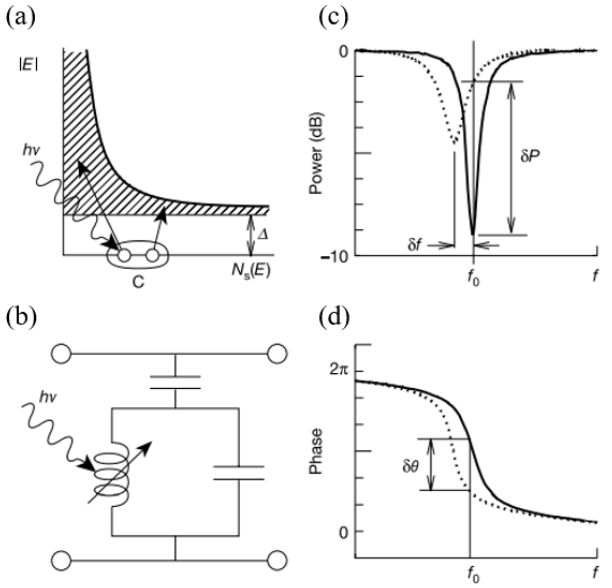

Fig. 1.3 The working principle of KIDs [13]. (a) Photons with energy $h\nu$ higher than 2Δ will break Cooper pairs. (b) The inductance of the LC resonator will be changed with changing the density of quasi-particles. (c) and (d) The changed inductance will shift the resonance frequency and also the phase.

QCDs rely on the extreme susceptibility of the single Cooper-pair box, a mesoscopic superconducting device, to pair-breaking radiation. As shown in Fig. 1.4 (a), the single pair box consists of a small island of superconductors connected to a ground electrode via a small tunnel junction. The island is biased with respect to the ground through a gate capacitor. Since it is sufficiently small to exhibit quantum behavior, its capacitance becomes a strong function of the presence or absence of a single free electron. Similar to a KID, the photons create electrons. Then a single electron entering or exiting the island in a QCD (via tunneling through the junction) produces a readily detectable frequency shift. The frequency shift is then sensed by a change in the phase of the microwave passing through the feedline. QCDs have demonstrated extraordinary high sensitivity, but they still need to show a large array and also have never been operated on a telescope. So in comparison with KIDs and TES, they have a lower TRL (technology readiness

level) than TES and KID [2]. The sensitivity of an QCD array of 25 pixels reaches an NEP of $\sim 2\times10^{-20}$ W/$\sqrt{\text{Hz}}$ at 200 μm wavelength [16].

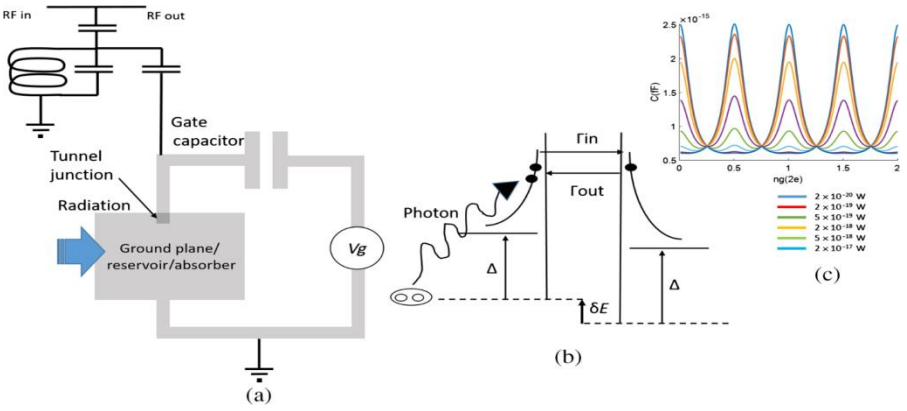

Fig. 1.4 The working process of QCDs [15]. (a) Radiation coupled to a reservoir via the antenna, and (b) By breaking Cooper pairs, photons generate quasiparticles which tunnel in and out of a small island which is capacitively coupled to the readout resonator. Changing the capacitance will in turn change the resonance frequency of the resonator. (c) Simulation of quantum capacitance signals for different radiation levels.

1.2.2 Brief introduction to TESs

A TES consists of a superconducting film with a steep resistive transition between the superconducting to the normal state, acting as a thermometer [11]. In practice, we usually bias the TES in its low transition region (See Fig. 1.5 (a)), where the resistance of the transition is proportional to the increased temperature.

When a TES is applied as a bolometer, it consists of a TES thermometer and an absorber, both of which are thermally well connected, but are poorly connected to the bath with a low thermal conductance (G). A TES bolometer is schematically shown in Fig. 1.5 (b). When radiation in the sub-mm or FIR is absorbed, the temperature of the absorber and TES increases. As a result, there is an increase of the TES resistance. Knowing the change of the TES resistance and thus the temperature, and the G, one is able to quantify the absorbed radiation power.

A TES can also be applied as a calorimeter, for example, to detect X-ray photons. A calorimeter is a device that measures the amount of heat deposited in a sample of material. A calorimeter differs from a bolometer. The former measures energy, while the latter measures power. By applying different absorbers and radiation-coupling schemes, a TES can be used in a wide range of wavelengths from millimeters to X-rays.

TESs either for bolometers or calorimeters need an external readout circuit as shown in Fig. 1.5 (c). The TES is voltage biased through the shunt resistance, and the low level signal from the TES is first amplified by a low noise SQUID, which is the amplifier suitable for the TES that has an unusually low impedance of roughly ~100 mΩ.

For a practical TES, the measured transition width in the presence of operational bias current is usually a few mK and is really narrow. For example, in a typical Ti/Au TES as shown in Fig. 1.5 (d), its normal resistance is 150 mΩ and it has a T_c of ~90 mK. Here the bilayer Ti/Au is a superconductor, whose T_c is adjustable by choosing a correct combination of thicknesses of Ti and Au. When the temperature changes by 1 mK around T_c, the resistance of this TES will change more than 10 mΩ. So, its resistive transition width is extremely narrow. There are a number of reasons that can affect the transition characteristic of a TES and the non-uniformities in the T_c of the bilayer. They include an external magnetic field, the transport current densities when approaching the critical current density, the magnetic field induced by the transport current, and the changes in temperature within the TES due to Joule heating or other sources of power. The transition characteristic of a TES can also be influenced by its geometry, by the defects in the boundaries of the bilayer, and by imperfections in the film itself. However, the transition width is finite even though the TES film is uniform with near-zero applied current and no external field [11].

The transition temperature T_c of a TES must be chosen in order to achieve the needed sensitivity and response time, and also to match a practical cryogenic system. The sensitivity and response time of a TES depends strongly on the transition temperature due to the T_c dependence of the heat capacity, thermal conductance, thermal noise, and other factors. Fortunately, the transition temperature can be altered to a desired value by using the bilayer, based on the proximity effect in a normal/superconducting bilayer [11,21,22]. A transition temperature of ~100 mK is chosen for space missions, such as SPICA because of the adiabatic demagnetization refrigerator (ADR), and ~ 400

mK if a ^{3}He cooler is used. More details about the mechanism of the TES will be discussed in Chapter 2.

TES technology has been used for a number of ground-based observatories. The third generation South Pole Telescope (SPT-3G) for the CMB has 16,000 bolometers with a NEP of $\sim 3\times10^{-17}$ W/$\sqrt{\text{Hz}}$ [23]. SCUBA-2 on the former JCMT has an array of 5120 pixels for each band (450/850μm in the wavelength) with a NEP of $\sim 2\times10^{-16}$ W/$\sqrt{\text{Hz}}$ [24]. The Electron Capture Decay of ^{163}Ho to Measure the Electron Neutrino Mass with sub-eV sensitivity (HOLMES) applies TES calorimeters to detect the spectrum of the Holmium (^{163}Ho) between 0.05 and 3 keV [25].

TESs were used for the High-resolution Airborne Wideband Camera Plus (HAWC+) with an NEP of $\sim 6.6\times10^{-17}$W/$\sqrt{\text{Hz}}$ and were selected for the HIgh-Resolution Mid-infrarEd Spectrometer (HIRMES) with an NEP of 2.2×10^{-17} W/$\sqrt{\text{Hz}}$ [26,27], at the airborne, Stratospheric Observatory for Infrared Astronomy (SOFIA) observatory [28].

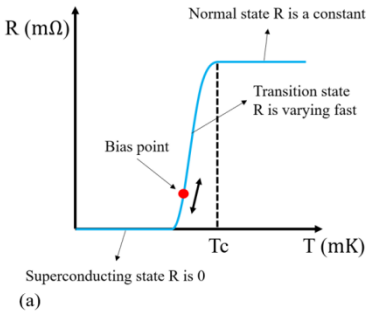

(a)

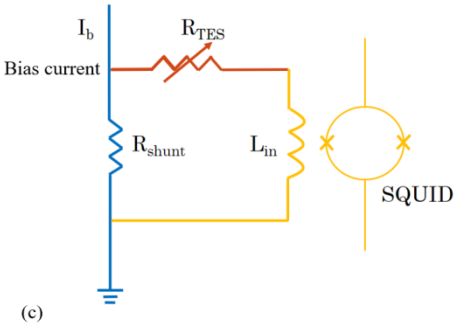

(c)

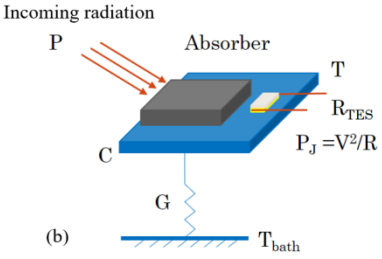

(b)

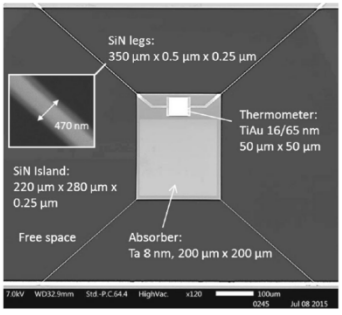

(d)

Fig. 1.5 (a) The typical RT (resistance-temperature) curve of a TES. The transition of the superconducting film from zero resistance to normal resistance, the sharpness of the transition line indicates its use as a sensitive thermometer, and the bias point is obtained by applied-voltage or magnetic field to make best use of the transition region. (b) Thermal model for a TES thermometer. TES-based bolometers and calorimeters consist of structures performing three crucial functions: thermalization of the input radiation, measurement of the variation in the temperature as a result of input radiation, and thermal isolation and mechanical support of the measurement structures. (c) Electrical model for a TES thermometer. The temperature change of the TES is transferred to the current change of the electrical circuit, which is read out by a SQUID. (d) A scanning electron microscope (SEM) picture of a Ti/Au TES detector [21].

TESs are selected for the 4500 bolometers with a NEP $\sim 1\times10^{-17}$ W/$\sqrt{\text{Hz}}$, to be prepared for the space mission of the Lite satellite for the studies of B-mode polarization and Inflation from cosmic background Radiation Detection (LiteBird) [9]. TES calorimeters of more than 3500 detectors with energy resolution 2–2.5 eV are being developed for Advanced Telescope for High ENergy Astrophysics/X-ray Integral Field Unit (ATHENA/XIFU) [29]. TES calorimeters are also candidates for the Hot Universe Baryon Surveyor (HUBS), which plans to have 3600 pixels with an energy resolution 0.6-2 eV (at 0.1-2 keV) [30].

TES bolometers were also planned for the use in the SpicA FAR infrared Instruments (SAFARI) on board of SPICA [6-8]. Unfortunately, SPICA as one of ESA M5 mission candidates was cancelled by the European Space Agency (ESA) in 2020. As for the sensitivity of SAFARI, the SRON bolometer team and a Jet Propulsion Laboratory (JPL) team have demonstrated TES bolometers with a NEP down to 1×10^{-19} W/$\sqrt{\text{Hz}}$ [21,31].

1.3 Multiplexing readout of TES array

In the FIR, TES detectors are approaching the photon statistics limit, which means their performance is dominated by the fluctuations in the arrival rate of photons at the detector, and not by the intrinsic noise of the detectors themselves [32]. Therefore, to increase the mapping speed and field of view in an instrument, the number of detectors should be increased instead of further

improving the sensitivity of the detectors, leading to the demand for TES arrays. Besides lower noise and a larger field of view, array receivers improve the image quality because sensitivity differences between pixels are washed out by scanning the array across the sky. This is especially important for ground-based instruments, but it helps those in space too. The SQUID amplifiers, the readout, and bias wiring will introduce heat load, which in turn will need more cooling power to cool down the detectors. So, to minimize the heat load on the detector cold stage and reduce the complexity of the cold wiring, a multiplexing readout technique is a must.

SQUID current amplifier multiplexing commonly makes use of time division multiplexing (TDM) [33,34], frequency division multiplexing (FDM) [35-37], and Walsh code division multiplexing (CDM) [38]. The state of the art of all of the three readout techniques are partly related to the need of applications. Therefore, the choice of each type of the readout system should be based on the requirements of a real instrument, such as mass, volume, power consumption, electrical-magnetic shield, and harness length [39]. The GHz frequency division multiplexing technique using microwave SQUID (MW-Mux) is maturing for TES [40], especially for ground-based applications. The next subsections will describe the various multiplexing schemes.

1.3.1 Time division multiplexing (TDM) and code division multiplexing (CDM) readout

TDM is one of the most mature techniques for reading out a TES array until now, in which TES detectors are DC-biased. Each TES connects with a SQUID that acts as an on/off switch. For a TES array with N × M pixels, N rows of detectors are read out one by one by switching on its SQUID sequentially, and detectors in M columns are read out in parallel. The readout signal then is amplified by a series of second-stage SQUIDs and a LNA. Since the detectors in N rows are biased with the same bias voltage, TDM requires high uniformity of an TES array. Hundreds of TES pixels can be read out within the sampling time of the TES array if the switching speed of the TDM is fast enough. The latest TDM technique development at the National Institute of Standards and Technology (NIST) shows a fast switch of rows with 128 ns and a total row time of 160 ns [41]. A TDM system with a total of 128 multiplexing factors is reported for bolometers [34]. A NIST 8 columns × 32 rows TDM readout system for a TES calorimeter has been developed with an energy resolution 2.16 eV at 6.9 keV [42]. A major disadvantage of TDM is the noise penalty with the increase of multiplexing factors in each column. The unfiltered noise above

the Nyquist frequency, at which rate all pixels in one column are sampled, is aliased into the signal band. Therefore, the SQUID noise level will increase by a factor of $\sqrt{N}$ with an increasing multiplexing number N. This sets a fundamental limit for the maximum multiplexing number for a large TES array of the noise. Another disadvantage of TDM is its architectural complications. The TDM system needs wiring for the columns and rows between channels, whereas the FDM system needs just one set of wires per channel, thus there is no coupling between channels. For FDM, the channels are fully parallel and independent. If one wire fails, then the readout system will lose only one channel. However, in a TDM system, if one wire fails, then the readout system will lose a whole column of channels. Until now, the TDM-based readout system, like FDM, has not been flown in space yet.

The CDM readout system diminishes the SQUID noise level that comes from the aliasing effect, which is an advantage compared with current TDM technique [43,44]. In CDM, Walsh matrices are applied for TES encoding, and instead of measuring one TES at a time, the signal from all TES detectors in one column is summed together simultaneously with different polarity patterns. In CDM, as in TDM, the TES detector is DC-biased, and the bandwidth of the SQUID must also be much larger than the Nyquist sampling frequency, which increases the SQUID noise level by a factor of $\sqrt{N}$. However, CDM will not suffer from an increase of the noise. Because pixels in the same column are read out simultaneously with different polarities, each input signal has N different independent samples, which increases the signal to noise ratio (SNR) by a factor of $\sqrt{N}$. The improvement of SNR compensates for the increase of the SQUID noise. The challenge for CDM is the complexity of the SQUID fabrication due to the encoding and coupling polarity [39]. CMD has the potential to achieve a large multiplexing factor [38] with further improvement of the fabrication of the SQUID. So far, a 32 channel CDM readout system for calorimeters is reported with an energy resolution of 2.7 eV at 5.9 keV [44]. Until now, the CDM has not been used in a telescope to perform science measurements in the sky.

1.3.2 Frequency division multiplexing (FDM) readout

In an FDM readout system, TES detectors are voltage-biased by sinusoidal carriers at different frequencies ranging usually from 1 to 5 MHz. Each TES has a unique resonance frequency set by its own high-quality factor (high-Q) inductor-capacitor (LC) bandpass filter, which limits the out of band noise and

provides the single frequency AC bias voltage to the TES [11,32,35]. A digital to analog converter (DAC) built in demultiplexer (DEMUX) electronics at room-temperature is used to produce the comb of the AC bias voltages to the LC filters. Each LC circuit filters out all AC bias currents except for the one at the resonant frequency for the TES. First of all, all the signals from an TES array are summed in the sum-point before being amplified by a SQUID amplifier. Then, the signal is amplified by an LNA, which is located in the front-end electronics (FEE) at 300 K. After the signal is transported through an analog to digital converter (ADC) that is also located on the DEMUX board, one can demodulate the combined signals to provide their information of both intensity I and phase Q. Finally, the re-modulated signal is sent to the sum-point of the SQUID, performing as the baseband feedback (BBFB) to increase the dynamic range of the SQUID and to reduce the input impedance of the SQUID [34]. More information about the FDM working principle is shown in Fig. 2.4 in Chapter 2.

There is no noise penalty of the FDM system with an increase of the multiplexing factor. Compared with TDM and CDM, where the SQUID acts as a switch, the LC filters are passive elements that have less power consumption, which is especially crucial for space applications. Theoretically, there is zero power dissipation on the mK stage by the FDM cold electronics, unless the SQUID is also located in the mK stage. The FDM system has a much easier cryogenic scheme than TDM and CDM since it has only one (or the first-stage) SQUID to sum signals from all TES detectors. FDM also has a higher effective usage of the bandwidth compared to the other two readout techniques. It was a challenge for the fabrication of high-Q LC filters with precisely designed resonance frequency, but following progress in lithography and design, now LC filters with high uniformity and high accuracy of resonance frequency can be used in an FDM readout system [45]. Since TES detectors are voltage-biased in MHz, the non-linear Josephson effect influences the performance of the TES (especially for calorimeters), which becomes an issue for the FDM readout system. Recently, the understanding of the physical process of TES under AC bias leads to an optimization design of the TES calorimeter, which minimizes the influence from the non-linear Josephson effect [39]. The state of the art of an FDM for calorimeter is the readout of 37 pixels simultaneously with an energy resolution of 2.2 eV at 5.9 keV [46]. For the FDM readout for bolometers, the demonstration of 60 pixels is reported with an NEP as low as 0.45 $\mathrm{aW}/\sqrt{\mathrm{Hz}}$ [47]. More detailed information of the FDM readout technique will be reported in this thesis Chapter 2 and 5-7.

1.3.3 Microwave SQUID multiplexing (MW-Mux) readout

Compared with the MHz bandwidth readout techniques, such as the TDM, CDM, and FDM, an MW-Mux system provides a much larger multiplexing factor for TES detectors per readout channel due to the use of a GHz bandwidth LNA[48]. An MW-Mux system makes use of a frequency division multiplexing mechanism. But, TES detectors are DC-biased, while each TES is coupled to a radio-frequency SQUID (rf-SQUID) that has a resonance frequency modulated by a high-Q resonator, which is inductively coupled to a common microwave feedline. All the signals in TES detectors are read out simultaneously and amplified by a rf-SQUID first, then go through a high bandwidth (4–8 GHz) cryogenic high-electron-mobility transistor (HEMT) amplifier. Although there are some challenges for the MW-Mux, for example, the complexity of the design of rf-SQUID operating at mK temperatures and the difficulties of the fabrication of resonators, the MW-Mux has the potential to offer a readout system for a very large (>1,000,000 pixels) TES array. So far, a gamma-ray TES detector array readout with a 128 multiplexing factor has been reported [40]. Recently, 38 TES calorimeters with an energy resolution 3.3 eV at 5.9 keV are read out with a MW-Mux readout [48]. Recently, both KIDs and MW-Mux need a Giga sample per second (GSPS) ADCs and DACs. The power consumption of GHz ADCs and DACs is much higher than MHz ADCs and DACs that are used in FDM systems. Therefore, there are challenges in building room temperature readout electronics for KIDs and MW-Mux with power consumption that is acceptable for space applications. A brief summary of different multiplexing techniques and their states of the art are shown in Table.1.1.

Table 1.1 Summary of multiplexing systems

Multiplexing technique	Readout bandwidth	Bias	TES number per SQUID	Multiplexing factor
TDM	1-5 MHz	DC voltage	one	32 × 8 for calorimeter [42] 32 × 4 for bolometer [34]
CDM	1-5 MHz	DC voltage	one	32 for calorimeter [44] -

FDM	1-5 MHz	AC voltage	multiple (~10-100)	37 for calorimeter [46] 60 for FIR bolometer [47]
MW-Mux	4-8 GHz	DC voltage	one	128 for Gamma-ray calorimeter [40] 38 for calorimeter [48]

1.4 Thesis outline

The research in this thesis enriches our knowledge of the FDM technique for reading out TES bolometer arrays. Developing and understanding an FDM system, which is eventually capable of reading out a large TES bolometer array (>1000) for space applications, specifically for SPICA/SAFARI, is the main goal of my Ph.D research. The following steps are taken to reach the main goal:

(1) A fundamental requirement of a FDM readout system is the readout noise level that is lower than the signal of the detectors. Therefore, the first step is to quantify the noise level of the readout chain using a noise model since the warm electronics usually contribute a considerable amount of readout noise.

(2) In an FDM system where a number of pixels are read out by a SQUID amplifier, all the signals from TES detectors will be summed up and amplified by the SQUID. Step 2 is to optimize the SQUID performance during the operation with the help of the calibration tone method.

(3) Electrical crosstalk (ECT) among pixels in an array is unavoidable when they are read out by an FDM system. Minimizing ECT is essential. The third step is to map the ECT within an array using an FDM demonstrator, and is also to understand different mechanisms, which cause ECT and determine the amplitude of ECT.

(4) As a successful demonstration, the performance of detectors read out in multiplexing mode (all the pixels are measured simultaneously) should be the same as what is measured in single pixel mode. Step 4 is to demonstrate an FDM readout of a 60-pixel array by comparing the measured NEP in both single-pixel mode and multiplexing mode. Within step 4, we also repeat the experiment by replacing it with a new TES array, which has microstrip wiring

and has TESs with a longer response time in order to reduce the ECT and also to allow operation at the preferred biasing points.

The thesis is organized as follows: Chapter 2 introduces the theory behind TES bolometers and FDM readout. Chapter 3 describes a noise model to characterize warm electronic noise. Chapter 4 reports a calibration tone method used for SQUID setting's optimization. Chapter 5 describes a new method used to map the electrical crosstalk of an FDM system. Chapter 6 reports the demonstration of an 60-pixel FDM readout system for low NEP TES bolometers. Chapter 7 shows the FDM readout of 43 pixels using slow TESs and also micro-strip wiring structures. Chapter 8 gives a summary of the whole thesis and an outlook.

References

[1] C. K. Walker, “Terahertz Astronomy”, **Chap 1**, (2016).

[2] D. Farrah, K. E. Smith, D. Ardila, C. M. Bradford, M. J. DiPirro, C. Ferkinhoff, et al., “Review: far-infrared instrumentation and technological development for the next decade”, J. Astron. Telesc. Instrum. Syst. **5**, 1– 34 (2019).

[3] D. Rigopoulou, F. Helmich, L. Hunt, J. Goicoechea, P. Hartogh, D. Fedele, et al., “The European far-infrared space roadmap”, arXiv:1701.00366, 2017.

[4] F. van der Tak, "The first results from the Herschel-HIFI mission", Adv. Space Res. **49**, 1395-1407 (2012).

[5] H. Dole, G. Lagache, J.-L. Puget, K. I. Caputi, N. Fernández-Conde, E. Le Floc'h, et al., "The cosmic infrared background resolved by Spitzer", A&A. **451**, 417 - 429 (2006).

[6] F. Van der Tak, S. Madden, P. Roelfsema, L. Armus, M. Baes, J. Bernard-Salas, et al., "Probing the Baryon Cycle of Galaxies with SPICA Mid- and Far-Infrared Observations", Publ. Astron. Soc. Aust. **35**, E002 (2018).

[7] P. R. Roelfsema, H. Shibai, L. Armus, D. Arrazola, M. Audard, M. D. Audley, et al., “Spica-a large cryogenic infrared space telescope: Unveiling the obscured universe”, Publ. Astron. Soc. Aust. **35,** E030 (2018).

[8] P. Roelfsema, M. Giard, F. Najarro, K. Wafelbakker, W. Jellema, B. Jackson, et al., “SAFARI new and improved: extending the capabilities of SPICA’s imaging spectrometer”, Proc. SPIE. **91431K**, (2014).

[9] G. C. Jaehnig, K. Arnold, J. Austermann, D. Becker, S. Duff, N. W. Halverson, et al., “Development of space-optimized TES bolometer arrays for LiteBIRD,” J. Low Temp. Phys. **199,** 646 (2020).

[10] National Academies of Sciences, Engineering, and Medicine 2021, " Pathways to Discovery in Astronomy and Astrophysics for the 2020s", Washington, DC: The National Academies Press.

[11] K. Irwin and G. Hilton, “Transition-Edge Sensors”, Berlin, Heidelberg: Springer. 63–150 (2005).

[12] J. E. Sadleir, S. J. Smith, I. K. Robinson, F. M. Finkbeiner, J. A. Chervenak, S. R. Bandler, et al., “Proximity effects and nonequilibrium superconductivity in transition-edge sensors”, Phys. Rev. B. **84,** 184502 (2011).

[13] P. K. Day, H. G. LeDuc, B. A. Mazin, A. Vayonakis and J. Zmuidzinas, “A broadband superconducting detector suitable for use in large arrays”, Nature. **425,** 817–821 (2003).

[14] B. Jochem, “Kinetic Inductance Detectors”, J. Low Temp. Phys. **167,** 292-304 (2012).

[15] F. R. Giorgetta, E. Baumann, M. Graf, Q. Yang, C. Manz, K. Kohler, et al., "Quantum Cascade Detectors", IEEE J. Quantum Electron. **45,** 1039-1052 (2009).

[16] P. M. Echternach, A. D. Beyer, C. M. Bradford, "Large array of low-frequency readout quantum capacitance detectors", J. Astron. Telesc. Instrum. Syst. **7(1),** 011003 (2021).

[17] M. I. Hollister, "SCUBA-2 instrument: an application of large-format superconducting bolometer arrays for submillimetre astronomy", PhD thesis, Univ. Edinburgh (2009).

[18] A. Catalano, M. Calvo, N. Ponthieu, R. Adam, A. Adane, P. Ade, et al., “Performance and calibration of the NIKA camera at the IRAM 30 m telescope”, Astron. Astrophys. **569,** 9 (2014).

[19] J. Bueno, V. Murugesan, K. Karatsu, D. J. Thoen and J. J. A Baselmans “Ultrasensitive Kilo-Pixel Imaging Array of Photon Noise-Limited Kinetic Inductance Detectors Over an Octave of Bandwidth for THz Astronomy”, J. Low Temp. Phys. **193,** 96–102 (2018).

[20] J. Schleeh, G. Alestig, J. Halonen, A. Malmros, B. Nilsson, P. A. Nilsson, et al., "Ultralow-Power Cryogenic InP HEMT With Minimum Noise Temperature of 1 K at 6 GHz", IEEE Electron Device Lett. **33,** 664-666 (2012).

[21] P. Khosropanah, T. Suzuki, M. L. Ridder, R. A. Hijmering, H. Akamatsu, L. Gottardi, J. van der Kuur, J-R. Gao, B. D. Jackson, “Ultra-low noise TES bolometer arrays for SAFARI instrument on SPICA”, Proc SPIE. **99140B**, (2016).

[22] M. D. Audley, G. de Lange, J-R. Gao, P. Khosropanah, R. Hijmering, M. Ridder, et al., "Optical performance of an ultra-sensitive horn-coupled transition-edge-sensor bolometer with hemispherical backshort in the far infrared", Rev. Sci. Instrum. **87,** 043103 (2016).

[23] J. Montgomery, A. J. Anderson, J. S. Avva, A. N. Bender, M. A. Dobbs, D. Dutcher, et al., "Performance and characterization of the SPT-3G digital frequency multiplexed readout system using an improved noise and crosstalk

model", Proc. SPIE. **114530X,** (2020).

[24] W. S. Holland, D. Bintley, E. L. Chapin, A. Chrysostomou, G. R. Davis, J. T. Dempsey, et al., "SCUBA-2: the 10 000 pixel bolometer camera on the James Clerk Maxwell Telescope", Mon. Notices Royal Astron. Soc. **430,** 2513–2533 (2013).

[25] A. Nucciotti, B. Alpert, M. Balata, D. Becker, D. Bennett, A. Bevilacqua, et al., "Status of the HOLMES Experiment to Directly Measure the Neutrino Mass", J Low Temp Phys. **193,** 1137–1145 (2018).

[26] C. Dowell, J. Staguhn, D. Harper, T. Ames, D. Benford, M. Berthoud, et al., "HAWC+: a detector, polarimetry, and narrowband imaging upgrade to SOFIA's far-infrared facility camera", Am. Astron. Soc. Meeting Abstr. **221,** 345.14 (2013).

[27] S. N. Richards, S. H. Moseley, G. Stacey, M. Greenhouse, A. Kutyrev, R. Arendt, et al., "SOFIA-HIRMES: Looking Forward to the HIgh-Resolution Mid-infrarEd Spectrometer", J. Astron. Instrum. **7,** 1840015 (2018).

[28] P. Temi, P. M. Marcum, E. Young, J. D. Adams, S. Adams, B.-G. Andersson, et al., "The SOFIA observatory at the start of routine science operations: mission capabilities and performance", Astrophys. J. Suppl. Ser. **212,** 24 (2014).

[29] D. Barret, T. L. Trong, J.-W. den Herder, L. Piro, M. Cappi, J. Houvelin, et al., "The ATHENA X-ray Integral Field Unit (X-IFU)", Proc. SPIE. **10699,** 324–338 (2018).

[30] W. Cui, J. N. Bregman, M. P. Bruijn, L.-B. Chen, Y. Chen, C. Cui, et al., "HUBS: A Dedicated Hot Circumgalactic Medium Explorer", Proc. SPIE. **114442S**, (2020).

[31] T. Suzuki, P. Khosropanah, M. L. Ridder, R. A. Hijmering, J. R. Gao, H. Akamatsu, et al., "Development of ultra-low-noise TES bolometer arrays," J. Low Temp. Phys. **184,** 52–59 (2016).

[32] M. A. Dobbs, M. Lueker, K. A. Aird, A. N. Bender, B. A. Benson, L. E. Bleem, et al., "Frequency multiplexed superconducting quantum interference device readout of large bolometer arrays for cosmic microwave background measurements", Rev. Sci. Instrum. **83,** 073113 (2012).

[33] W. B. Doriese, J. A. Beall, S. Deiker, W. D. Duncan, L. Ferreira, G. C. Hilton, et al., "Time division multiplexing of high-resolution x-ray microcalorimeters: Four pixels and beyond", Appl. Phys. Lett. **85,** 4762–4764 (2004).

[34] D. Prêle, F. Voisin, M. Piat, T. Decourcelle, C. Perbost, C. Chapron, et al., "A 128 multiplexing factor time-domain SQUID multiplexer", J. Low Temp. Phys. **184,** 363–368 (2016).

[35] B. D. Jackson, P. A. J. de Korte, J. van der Kuur, P. D. Mauskopf, J. Beyer, M. P. Bruijn, et al., "The SPICA-SAFARI detector system: TES detector arrays with frequency division multiplexed SQUID readout", IEEE Trans. Terahertz Sci. Technol. **2,** 12–21 (2012).

[36] R. H. den Hartog, M. P. Bruijn, A. Clenet, L. Gottardi, R. Hijmering, B. D.Jackson, et al., "Progress on the FDM Development at SRON: Toward 160 Pixels", J. Low Temp. Phys.**176,** 439–445 (2014).

[37] H. Akamatsu, L. Gottardi, J. van der Kuur, C.P. de Vries, M.P. Bruijn, J.A. Chervenak, et al., "Progress in the Development of Frequency-Domain Multiplexing for the X-ray Integral Field Unit on Board the Athena Mission", J. Low Temp. Phys. **199,** 737–744 (2020).

[38] W. B. Doriese, S R. Bandler, S Chaudhuri, C S. Dawson, E V. Denison, S M. Duff, et al., "Optimization of Time- and Code-Division-Multiplexed Readout for Athena X-IFU", IEEE Trans. Appl. Supercond. **29,** 1–5 (2019).

[39] L. Gottardi, K. Nagayashi, "A Review of X-ray Microcalorimeters Based on Superconducting Transition Edge Sensors for Astrophysics and Particle", Physics. Appl. Sci. **11,** 3793 (2021).

[40] J. A. B. Mates, D. T. Becker, D. A. Bennett, B. J. Dober, J. D. Gard, J. P. Hays-Wehle, et al., "Simultaneous readout of 128 X-ray and gamma-ray transition-edge microcalorimeters using microwave SQUID multiplexing", Appl. Phys. Lett. **111,** 062601 (2017).

[41] W. B. Doriese, P. Abbamonte, B. K. Alpert, D. A. Bennett, E. V. Denison, Y. Fang, et al., "A practical superconducting-microcalorimeter X-ray spectrometer for beamline and laboratory", Rev. Sci. Instrum **88,** 053108 (2017).

[42] S. J. Smith, J. S. Adams, S. R. Bandler, S. Beaumont, J. A. Chervenak, E. V. Denison, et al., "Performance of a Broad-Band, High-Resolution, Transition-Edge Sensor Spectrometer for X-ray Astrophysics", IEEE Trans. Appl. Supercond. **31,** 1–6 (2021).

[43] G. M. Stiehl, W. B. Doriese, J. W. Fowler, G. C. Hilton, K. D. Irwin, C. D. Reintsema, et al., "Code-division multiplexing for X-ray microcalorimeters", Appl. Phys. Lett. **100,** 072601 (2012).

[44] K. M. Morgan, B. K. Alpert, D. A. Bennett, E. V. Denison, W. B. Doriese, J. W. Fowler, et al., "Code-division-multiplexed readout of large arrays of TES microcalorimeters", Appl. Phys. Lett. **109,** 112604 (2016).

[45] M. P. Bruijn, A. J. van der Linden, L. Ferrari, L. Gottardi, J. van der Kuur, R. H. den Hartog, et al., "LC Filters for FDM Readout of the X-IFU TES Calorimeter Instrument on Athena", J. Low Temp. Phys. **193,** 661–667 (2018).

[46] H. Akamatsu, D. Vaccaro, L. Gottardi, J. van der Kuur, C. P. de Vries, K. Ravensberg, et al., "Demonstration of a simultaneous readout of 37 Transition Edge Sensors X-ray microcalorimeters with frequency domain multiplexing", unpublished work (2021).

[47] Q. Wang, P. Khosropanah, J. van der Kuur, G. de Lange, M. D. Audley, A. Aminaei, et al., "Frequency division multiplexing readout of 60 low-noise transition-edge sensor bolometers", Appl. Phys. Lett. **119**, 182602 (2021).

[48] Y. Nakashima, F. Hirayama, S. Kohjiro, H. Yamamori, S. Nagasawa, A. Sato, et al., "Low-noise microwave SQUID multiplexed readout of 38 x-ray transition-edge sensor microcalorimeters", Appl. Phys. Lett. **117,** 122601 (2020).

Chapter 2

Background of transition edge sensor and frequency division multiplexing system

In Chapter 1, a basic introduction of the definition and classification of the TES system is given. In the first section of this chapter, some aspects of the basic theory of TES physics are discussed, focusing on the performance of a single TES bolometer. In the second section of this chapter, the working principle of the FDM readout system, which aims to read out a TES bolometer array, is described. In addition, many practical techniques and suggestions for the FDM readout system are reported based on my own laboratory experience.

2.1 Transition edge sensor (TES) physics

In this section, the theories for TESs, specifically for the bolometers at Far Infrared (FIR), are discussed. However, the discussions can also be applied for another type of TES detectors, namely, calorimeters.

As described in section 1.2.2, a TES bolometer consists of three key structures to fulfill the requirement of a sensitive FIR detector. The first structure is the TES bilayer, which measures the change in the temperature as a result of the input radiation. By using the superconducting proximity effect [1], which usually has a combination of normal-metal/superconductor materials, the T_c of a TES can range from 50 to 150 mK. However, one can design a different range of T_c by choosing the thickness of each layer in the bilayer. Different types of TES bilayer have been reported for detection at submm, FIR and γ-ray wavelengths, for example, Ti/Au [2,3], Mo/Au [4,5] bilayers for bolometers and calorimeters. The second structure is an absorber, which receives the radiation power and then thermalizes it with the TES. The absorber should be thermally well connected with the TES detector, either by direct attachment with the TES or indirect connection with the TES via a thermal link. For an FIR bolometer, the absorber can be a superconducting film with a much higher critical temperature than the T_c of the TES, but with a low energy gap, which can absorb the targeted radiation. Such a thin film can have its normal sheet resistance to be the same as the impedance of free-space. In the example shown in Fig. 1.5 (d), the thin film Tantalum (Ta) absorber has a 200×200 μm^2 size and a thickness of 8 nm, which provides a 377 Ω/□ normal sheet resistance that matches the free-space impedance. The Ta absorber has a T_c of ~1 K and remains superconducting when it is at the low limit of radiation power, so the absorber does not affect the time constant when it is in the dark or at the low radiation limit. In this case, the radiation is coupled to the absorber through a feedhorn. There are also other ways to couple the radiation, such as an antenna for the bolometers in some CMB applications [6]. The CMB peaks at mm and submm wavelengths. The third structure is the thermal legs, which provide the thermal isolation and mechanical support of the detector structures. The thermal legs connect the suspension structure, typically a Si_3N_4 membrane, which holds the TES bilayer and absorber, with a heat sink at a bath temperature. The thermal conductance G is determined by the cross-section and length of the thermal legs. The long, narrow, and thin Si_3N_4 legs ensure the low thermal conductance of the detector, which is crucial to achieve an extremely low NEP, required by some space FIR applications

such as SAFARI. To further understand the performance of a TES bolometer, some physical parameters are described in the following subsections.

2.1.1 TES bolometer steady-state power

We discuss the TES bolometer to be read out by a SQUID current amplifier. In this case, we make use of the voltage-bias for the TES to minimize loading effects, which increase the SQUIDs amplifier noise [7]. The voltage-bias also minimizes the Johnson noise contribution of the load resistor.

In the electrical scheme shown in Fig. 1.5 (c), a bias current I_b is applied to a shunt resistor R_{shunt} in parallel with a SQUID input inductance L_{in}, and a TES. In practice, there is also a parasitic resistance of the wires in the circuit. Now we call "the series resistance" (R_{series}) that contains both the resistance of the shunt resistor and the parasitic resistance. Since the R_{series} ($\sim$1 mΩ) is much smaller than the resistance of the TES R_{TES} ($\sim$100 mΩ) if the bilayer is Ti/Au, the TES bolometer circuit can be represented by a Thevenin-equivalent circuit consisting of a bias voltage $V_{bias} = I_b R_{series}$. The discussions of TES's performance are based on the Thevenin-equivalent circuit.

The thermal and electrical response of a TES bolometer are essential for the detection performance as they determine the speed of a TES bolometer. There are two coupled differential equations, where the thermal equation defines the temperature T of the TES, while the electrical equation represents the current I [7].

Firstly, the state variable T is presented in a heat power-balance Equation (2.1):

$$C\frac{\delta T}{\delta t} = -P_{bath} + P_J + P_{signal}, \tag{2.1}$$

where C is the heat capacity, including both the capacity of the bilayer and the absorber. P_{bath} is the power flowing from the TES to the heat sink at a bath temperature, P_J is the Joule power dissipation according to V^2/R, and P_{signal} represents the power of the incoming signal.

Secondly, another state variable I is determined by an electrical Equation (2.2):

$$L\frac{\delta I}{\delta t} = V_{bias} - IR_{series} - IR_{TES}, \tag{2.2}$$

where L is the inductance, V_{bias} is the Thevenin-equivalent bias voltage, I is the electrical current across the TES, and R_{TES} is the DC resistance of the TES, which is generally a function of both temperature and current.

For TES bolometers, the incoming signal is relatively small [7], so it is suitable to use the small-signal limit around the steady-state values of the resistance R_0, temperature T_0, and current I_0 to linearize the nonlinear differential equations [7]. With the assumption of a power-law dependence of the power flowing into the heat bath, Equation (2.3) is obtained:

$$P_{bath} = K(T^n - T_{bath}^n), \tag{2.3}$$

where the pre-factor K is a parameter scaling with the heat flux, and n is a thermal conductance exponent that reflects the feature of the thermal legs, which usually ranges from 2 to 4. Since the thermal conductance $G \equiv \delta P_{bath}/\delta T = nKT^{n-1}$, $\delta T \equiv T - T_0$, K can be expressed as $G/n(T^{n-1})$, and the above equation can be expanded in small signal around T_0 to generate a linear expression:

$$P_{bath} \approx P_{bath0} + G\delta T. \tag{2.4}$$

The values of K and n are determined by the nature of the thermal link to the heat bath. The steady-state power flow to the heat bath $P_{bath} = P_J + P_{signal}$, where the steady-state Joule power is $P_J = V_0^2/R_0 = I_0^2R_0$ and the steady-state signal power is P_{signal}.

Therefore, a similar linearization for the resistance of a TES could be performed by expanding in small signal around R_0, T_0, I_0, and with $\delta I \equiv I - I_0$:

$$R_{TES} \approx R_0 + \frac{\partial R}{\partial T}|_{I_0}\delta T + \frac{\partial R}{\partial I}|_{T_0}\delta I. \tag{2.5}$$

In a TES bolometer, the two most important parameters used for calculating the signal-to-noise ratio (SNR) of the detector are the temperature sensitivity α as well as the current sensitivity β, both of which are unitless and logarithmic parameters. These two parameters are expressed in Equation (2.6) and (2.7) respectively:

$$\alpha \equiv \frac{\partial \log R}{\partial \log T}\Big|_{I_0} = \frac{T_0}{R_0}\frac{\partial R}{\partial T}\Big|_{I_0}, \tag{2.6}$$

$$\beta \equiv \frac{\partial \log R}{\partial \log I}\Big|_{T_0} = \frac{I_0}{R_0}\frac{\partial R}{\partial I}\Big|_{T_0}. \tag{2.7}$$

By rewriting Equation (2.5) with α and β, the new expression for the resistance of the TES is:

$$R_{TES} \approx R_0 + \alpha\frac{\partial R_0}{\partial T_0}\delta T + \beta\frac{\partial R_0}{\partial I_0}\delta I. \tag{2.8}$$

Equation (2.8) demonstrates the dependence of the resistance of a TES on both the temperature and the current.

Similar to the resistance of a TES, the Joule power can also be expanded in small signal around R_0, T_0, and I_0 as:

$$P_J = I^2R = (I_0 + \delta I)^2 R \approx P_{J_0} + 2I_0R_0\delta I + \alpha\frac{P_{J_0}}{T_0}\delta T + \beta\frac{P_{J_0}}{I_0}\delta I. \tag{2.9}$$

Knowing the linearization of differential equations, we can study the Current-Voltage (IV) curves to characterize the performance of a TES bolometer. The IV curves can be measured experimentally, and can give the basic properties of the TES bolometer and thus the noise performance.

Here we use the measurement results of a Ti/Au TES at a bath temperature of 90 mK to discuss the IV curve. The T_c of the TES is 113 mK. There is a tilt line in the first left part of the IV curve in Fig. 2.1 (a), which indicates the existence of the series resistance R_{series}. The designed shunt resistance is 1 mΩ, which is dominated in the series resistance.

The TES operates in the IV transition range instead of in the superconducting state. Therefore, it is essential to calibrate the raw IV curve by eliminating the voltage of the series resistor. In practice, the current through the TES and the series resistors is the same, and the change of the current I_{TES} in the TES will be detected by the SQUID as I_{SQUID}. The turn ratio R_{ratio} between the SQUID input and output mutual inductance determines the relation between those two currents as $I_{TES} = I_{SQUID}/R_{ratio}$. Usually, the resistance of a TES when it is in the normal state (R_n) will be determined by a Resistance-Temperature (RT) curve or a direct DC 4-points measurement above its T_c. With known parameters of bias voltage V_{bias}, current in SQUID I_{SQUID}, and normal resistance R_n, the calibration of the raw IV curve can be performed. The calibrated IV curve is shown in Fig. 2.1 (b), which demonstrates that in the transition region of the TES, when the voltage increases, the current of the TES decreases quickly, indicating that the resistance in the transition region increases steeply as shown in Fig. 1.5 (a).

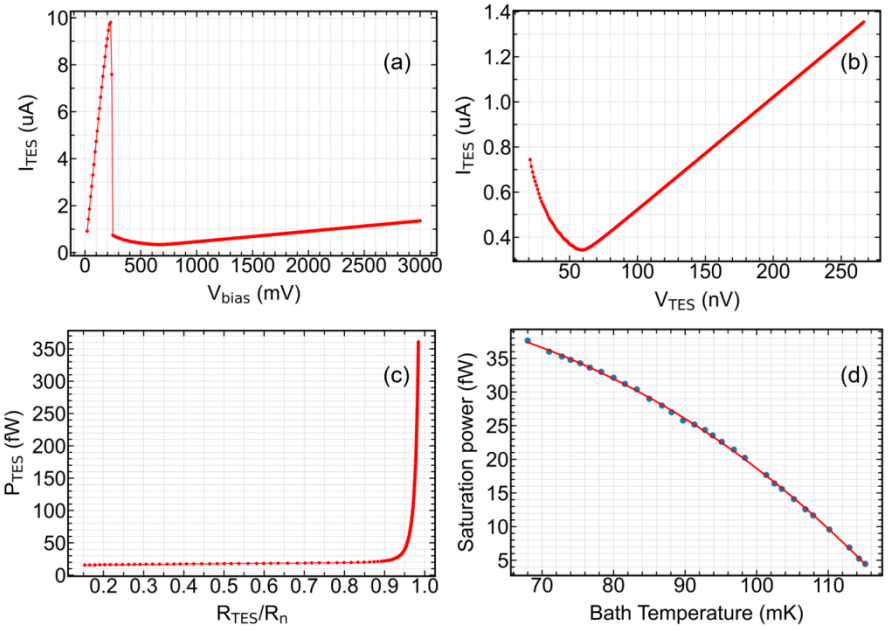

Fig. 2.1 (a) The raw IV curve of one TES detector measured at 90 mK. (b) The calibrated IV curve. (c) The power plot with TES biased at different positions.

(d) Fitting of power plateau of the TES as determined from the curves displayed in (c) at different bath temperatures ranging from 70 to 115 mK.

With the formula $P_{TES} = I_{TES} \times V_{TES}$, the calibrated IV curve can be transferred to a Power-Resistance (PR) curve also known as a power plateau, as shown in Fig. 2.1 (c). The value of R_{TES}/R_n represents the positions of a TES at transition, which equals 1 when a TES is normal. The saturation power denotes at which power a TES will go into normal state while the effective saturation power denotes the maximum incident power which brings the TES into the normal state. The values of the effective saturation power are usually determined by the first flat part of the power plateau.

Since the resistance of a TES will be influenced by not only current but also temperature, the R_{TES} will depend on bath temperature even at the same bias voltage. Therefore, the IV curve and PR curve, and thus the effective saturation power will be different at different bath temperatures, as shown in Fig. 2.1 (d). The effective saturation power of the TES decreases with an increase of the bath temperature. Because the total saturation power that makes the TES normal is the combination of power from the bath and effective saturation power, the higher power from the bath means a lower effective saturation power. By fitting the saturation power at different bath temperatures with Equation (2.3), the parameters T_c, K, and n can be determined, based on which the thermal conductance G can be derived.

The saturation power of a TES needs comprehensive consideration. If the saturation power is too high, a large bias-voltage is required to bring the TES into its transition region, causing a high current noise when it is read out. On the other hand, if the saturation power is too small, the TES will have a limited dynamic range to detect far-infrared radiation. Normally, the saturation power is approximately twice the maximal incident power.

2.1.2 Electro-thermal feedback and stability of TES

In this subsection, the influence of the electro-thermal feedback (ETF) and the stability criterion of a TES will be discussed since it needs to work stably. A TES is operated in the linear part of its transition range. Therefore, ETF is needed to make a TES system functional for sky observations, as TES devices would be highly non-linear without strong ETF.

Because the resistance of a TES has a dependence on both current and temperature, there is a feedback relation between electrical and thermal response, which is called ETF. The ETF can be positive or negative. A positive ETF feedback occurs under the condition of current-bias ($R_{series} \gg R_{TES}$), because, as the temperature increases, the resistance increases as well, causing an increase of the Joule power $P_J = I^2R$, leading to the TES detector being unstable.

A negative ETF occurs in the case of voltage-bias saturation ($R_{TES} \gg R_{series}$). With increasing temperature, the increased resistance causes a decrease in the Joule power $P_J = V^2/R$, causing the TES detector to be stable. There are significant advantages of negative ETF over a positive ETF. For example, when a positive ETF is used, the amplifier will easily become unstable due to the increasing Joule power. On the contrary, when the TES detector is operated with negative ETF, the increasing temperature is reduced by the decrease of the Joule power, making the TES detectors stable. The negative ETF makes the circuit more uniform and reproducible because the closed-loop gain is determined by the bias-circuit rather than the amplifier itself. Furthermore, the negative ETF can also speed up the TES detector response by accelerating the decrease process of the incident power. Meanwhile, the decrease in the response time will lead to an increase in the dynamic range of useful bandwidth of the TES. Another important advantage of negative ETF is the ability to keep the TES to be operated in a linear range, which is useful for astrophysics measurements.

A TES performs as a damped harmonic oscillator [8]. Therefore, without the consideration of an ETF, the intrinsic thermal time constant of a TES is:

$$\tau_0 = \frac{C}{G}. \tag{2.10}$$

A dimensionless parameter is derived from Equation (2.9) to describe the low-frequency loop gain of the ETF:

$$\mathcal{L} = \frac{P_{J0}\alpha}{GT_0}. \tag{2.11}$$

We are interested mostly in TESs that are voltage-biased and read out by SQUIDs. In this case, the inductance L of the TES is small, so that the rise and fall times (the time to come back to the steady state after the incident radiation) can be represented by the electrical time constant τ_{ele} of bias circuit and the effective thermal time constant τ_{eff}, respectively:

$$\tau_{ele} = \frac{L}{R_{series}+R_{TES}(1+\beta)}, \tag{2.12}$$

$$\tau_{eff} = \frac{\tau_0}{1+\frac{(1-R_{series}/R_{TES})\mathcal{L}}{1+\beta+R_{series}/R_{TES}}}. \tag{2.13}$$

When the rise time is equal to the fall time, the TES is in the critically-damped condition. If the rise time is shorter than the fall time, the TES is over-damped. In contrast, if the rise time is longer than the fall time, the TES is under-damped. The criterion for the stability of a TES when it is over-damped is:

$$R_{TES} > \frac{(\mathcal{L}-1)}{(\mathcal{L}+1+\beta)} R_{series}. \tag{2.14}$$

Since $\mathcal{L}$ and β are not smaller than 0, the criterion is automatically satisfied when the TES resistance $R_{TES} > R_{series}$, indicating that an over-damped, simple, linear, voltage-biased TES is always stable. Therefore, to keep a TES stable, one should avoid the under-damped behavior.

The general solution of the critical-damped equation is $\frac{\tau_{eff}}{\tau_{ele}} = 3 + 2\sqrt{2}$ with $\beta = 0$ [7,8], therefore, the stability criterion of a TES is:

$$\frac{\tau_0}{1+\frac{(1-R_{series}/R_{TES})\mathcal{L}}{1+R_{series}/R_{TES}}} \geq (3 + 2\sqrt{2})\frac{L}{R_{series}+R_{TES}}. \tag{2.15}$$

Equation (2.15) indicates that, to keep a TES in a stable operation condition, the fall time τ_{eff} should be at least a factor of $3 + 2\sqrt{2}$ times longer than the rise time τ_{ele}, which is essential to design TES detectors.

Fig. 2.2 (a), (b) show the fall time of a 'fast' TES detector with a heat capacity C of 4 fJ/K, while (c), (d) show the response time of a 'slow' TES with a C of 26 fJ/K. The thermal conductance G of the 'fast' and 'slow' TES is the same and equal to 0.8 pW/K. Therefore, the thermal time constant of the 'slow' TES is over 6.5 times longer than that of the 'fast' TES. The rise time $\tau_{eff} \sim 54$ μs with the inductance L of 3 μH, and R_{TES} of 88 mΩ at ~50% in transition, which indicates a stable fall time should be >0.2 ms. The fall time is smaller when the TES operates at a lower position in its transition due to the loop gain becoming higher.

Fig. 2.2 (b) shows the fit of the fall time of the 'fast' TES when it is biased at 70% in the transition. The fall time decreases from 0.9 ms to below 0.2 ms quickly when the 'fast' TES is biased below 50% in the transition, causing oscillations due to instability. Fig. 2.2 (d) shows the fall time of the 'slow' TES is 20 ms when it is biased at 70% in the transition, this value stays above 0.2 ms until very low (5%) in the transition. Therefore, compared to the 'fast' TES, the 'slow' TES can be biased lower in transition, leading to higher SNR and lower crosstalk [9].

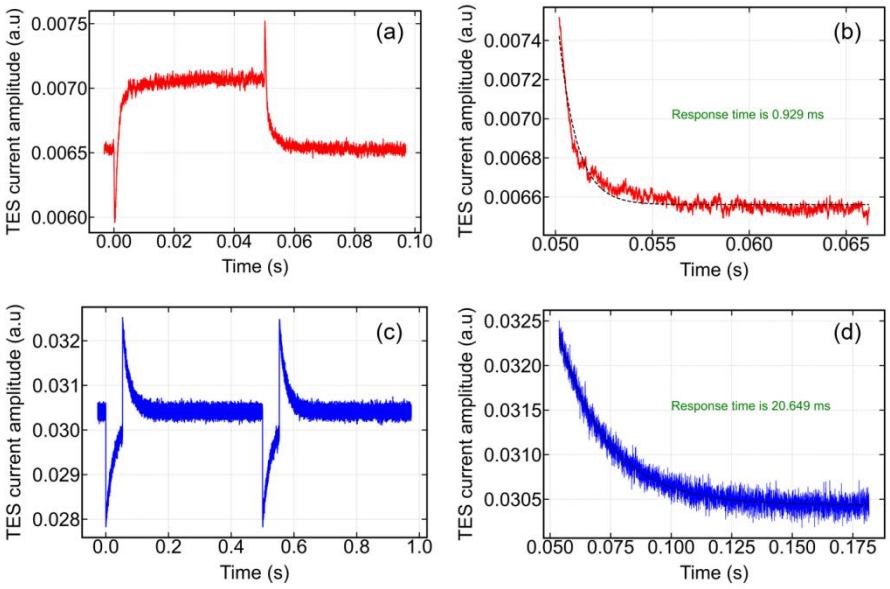

Fig. 2.2 (a) The time series data of a TES with a smaller response time when a TES is biased at 70% in the transition. An oscillation is about to happen. (b) The zoomed and fit plot of (a), the effective response time is 0.9 ms. (c) The time series data of a TES with a high response time value, which is also biased at 70% in the transition. (d) The zoomed and fit plot of (c), the effective response time is 20 ms.

We measured the fall time of 'slow' TES to be 20 ms when the TES is biased at 70% of R_{TES}/R_n in transition, while the 'fast' TES fall time is 0.9 ms when it was at the same transition. We measured a larger slow-down factor (20) than the designed one (6.5) , which is due to the fact that the effective time constant depends very strongly on the thermal responsivity (α) of a TES. Our detailed measurements of 'fast' and 'slow' TESs will be described in Chapter 6 and Chapter 7, respectively.

2.1.3 Responsivity and noise of TESs

In a SQUID-based readout system, the SQUIDs measure the change of current, therefore, the responsivity S, which defines the ability to transfer the incident power to the change of the current, is an important parameter. The current responsivity α described in subsection 2.1.2 only shows the properties of the TES itself, while S represents the characteristics of both the TES and the readout circuit.

In an AC voltage-biased circuit, the responsivity of a TES at low frequency ($\leq$ 100 Hz) can be expressed as:

$$S_{AC} = -\frac{1}{I_{TES}R_{TES}}\left(\frac{L}{\tau_{ele}R_{TES}\mathcal{L}} + \left(1 - \frac{R_{series}}{R_{TES}}\right)\right)^{-1}, \tag{2.16}$$

where $-\frac{1}{I_{TES}R_{TES}} = -\frac{1}{V_{TES}}$, by expanding τ_{ele} with Equation (2.12) $\frac{L}{\tau_{ele}R_{TES}\mathcal{L}} \sim \frac{1+\beta}{\mathcal{L}}$, and $1 - \frac{R_{series}}{R_{TES}} \sim 1$ with $R_{series} \ll R_{TES}$. The V_{TES} is the root mean square (RMS) value in the calculation. Therefore, in a system with a high loop gain (e.g. $\geq$ 20), the responsivity S_{AC} could be represented by the inverse of the TES voltage $\sim \frac{1}{V_{TES}}$.

In general, four types of noise sources can be detected in a TES bolometer. They are Johnson noise, phonon noise, photon noise, and excess noise. The current noise contributed by each noise type can be calculated by multiplying the noise equivalent power (NEP) with the responsivity S_{AC}.

Johnson noise is the electronic noise produced by the agitation of the electrons inside an electrical conductor under equilibrium conditions, even without applied voltage. The NEP and current noise of Johnson noise is described by two equations:

$$NEP_{Johnson} = \sqrt{\frac{4k_B T_{bath} I_{TES}^2 R_{TES}(1+2\beta)(1+(2\pi f\tau_0)^2)}{\mathcal{L}^2}}, \tag{2.17}$$

$$S_{I,Johnson} = NEP_{Johnson} \times S_{AC}, \tag{2.18}$$

where k_B is Boltzmann's constant, T_{bath} is the bath temperature for the TES, and f is the frequency of the noise.

Comparing with Johnson noise, phonon noise arises from the random exchange of phonons. Phonon noise is also referred to as thermal fluctuation noise, generated by the random exchange of the energy between a heated object and its surrounding environment. Each phonon has an energy of order $k_B T$. The NEP and current noise of phonon noise is given by [7]:

$$NEP_{phonon} = \sqrt{4\gamma k_B T_C^2 G}, \tag{2.19}$$

$$S_{I,phonon} = NEP_{phonon} \times S_{AC}, \tag{2.20}$$

where γ is a factor ranging from 0.5 -1 , depending on the thermal gradient along the thermal link to the bath, T_c is the critical temperature of the TES, and G is the thermal conductance between the TES and the bath. Since in a high loop gain electrical circuit, the $NEP_{Johnson}$ is usually negligible, the NEP_{phonon} dominates. The NEP_{phonon} of the TES is determined by the critical temperature T_c and the thermal conductance G, which means that a low T_c and a low G are needed for an extremely low NEP, such as what is required for SAFARI. How to design and fabricate a low NEP TES detector is described in detail in [10,11].

Photon noise describes the noise from the incident radiation power, which comes from the sky and/or other optical sources. This thesis will focus on experiments in the dark, without a targeted optical source, therefore, the photon noise described here mainly comes from stray light. The NEP and current noise of photon noise can be expressed as [12]:

$$\mathrm{NEP}_{\mathrm{photon}} = \sqrt{2\mathrm{P}_{\mathrm{signal}}\mathrm{h}\nu}, \tag{2.21}$$

$$\mathrm{S}_{\mathrm{I,photon}} = \mathrm{NEP}_{\mathrm{photon}} \times \mathrm{S}_{\mathrm{AC}}, \tag{2.22}$$

where $\mathrm{P}_{\mathrm{signal}}$ is the incoming radiation power, $\mathrm{h}\nu$ is the intensity-weighted average photon energy, h is the Plank constant, and ν is the frequency of the radiation.

As for the excess noises, they are the noise beyond the three types of noise described earlier. The first type of the excess noises is dependent on the thermal circuit model of the detector, which is referred to as the internal thermal fluctuation noise (ITFN); the second type has the same frequency dependence as Johnson noise voltage in the sensor, which is referred to as excess electrical noise; the third type is excess low-frequency noise in the TES, sometimes with a $1/f$ dependence, which is referred to as low-frequency noise. All the excess noise types, especially ITFN and low-frequency noise, must be kept as low as possible since they will increase the NEP [7].

In a dark measurement without optical signal, the NEP of a TES is dominated by the $\mathrm{NEP}_{\mathrm{phonon}}$, which can be estimated from the parameters T_{C} and G, and which can be determined from the measurement described in 2.1.1. However, in practice, since a TES is in an electrical circuit, $\mathrm{NEP}_{\mathrm{Electrical}}$ is determined by all noise sources discussed previously and can be calculated with the measured total current noise and responsivity. Since the current noise from the entire readout chain $\mathrm{S}_{\mathrm{I,readout}}$ will be quadratically added to the other current noises to form the total measured current noise $\mathrm{S}_{\mathrm{I,total}}$, the $\mathrm{NEP}_{\mathrm{Electrical}}$ can thus be written as:

$$\mathrm{NEP}_{\mathrm{Electrical}} = \sqrt{(\mathrm{S}_{\mathrm{I,total}}^{\ 2} - \mathrm{S}_{\mathrm{I,readout}}^{\ 2})} \times \mathrm{S}_{\mathrm{AC}}. \tag{2.23}$$

By taking all the types of noise into account, one can build a noise model to compare with the measured current noise data. An example is shown in Fig. 2.3. The red line is the total noise composed of phonon noise, Johnson noise, and readout noise, calculated with the measured parameters. The noise model matches well with the measured data except at frequencies below 10 Hz. This deviation probably is not only due to the low-frequency noise that comes from a Pulse Tube Cooler (PTC), which is a part of the mK cooler to operate a TES, but also some excess noise. More detailed information about the noise fit is discussed in Chapter 7. We focus on the study of detector performance between 10 Hz -100 Hz to analyze phonon noise and readout noise. The analysis and optimization of low frequency noise is important for a real flight module, however it is beyond the scope of this thesis.

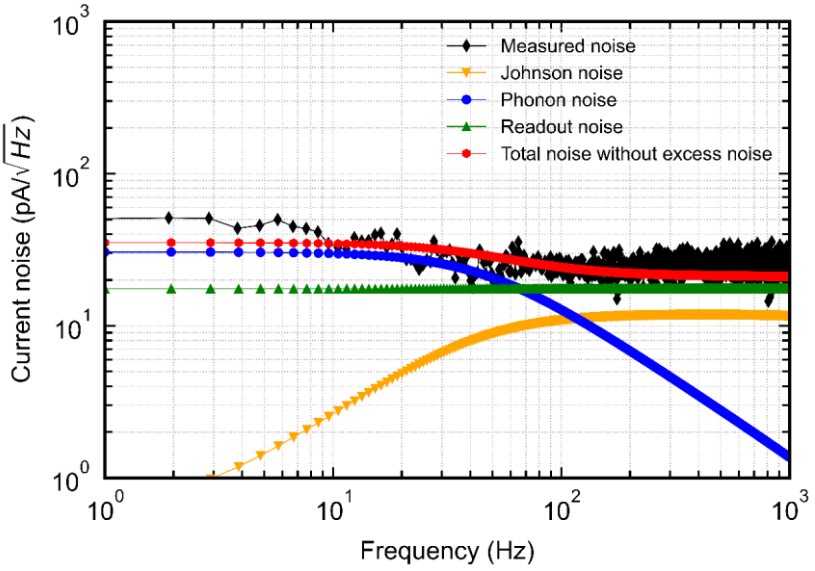

Fig. 2.3 The noise model compared to measured data. The noise model in red matches well to the measured data, only deviating below ~10 Hz due to low-frequency excess noise.

2.2 Frequency division multiplexing (FDM) readout system

The characteristics and performance of a TES bolometer have been discussed in the previous section. To have a high detection rate or mapping speed and achieve a large field of view through a telescope, a single TES is not sufficient, actually a TES array is needed, which needs a multiplexing technique to read out many pixels simultaneously. This thesis will focus on the frequency division multiplexing (FDM) readout system, which had been planned to be the readout system for SAFARI until 2020. A brief introduction to an FDM system is given in subsection 1.3.2, and this section introduces some key elements in the FDM readout chain from cryogenic to room temperature, including inductor-capacitor (LC) filters, superconducting quantum interference devices (SQUID), front-end electronics (FEE), and room-temperature demultiplexer (DEMUX).

A diagram of the SAFARI prototype FDM readout system is shown in Fig. 2.4. A TES bolometer array is connected in series with 88 narrow bandpass cryogenic LC filters. A local oscillator (LO) together with a digital-to-analog converter (DAC), both of which are located on DEMUX board at room temperature provides the MHz frequency, sinusoid bias voltages. After a voltage division between the large resistors at room temperature ($\sim$50 kΩ) and the shunt resistor, the bias voltage is applied to each TES with its resonance frequency defined by the LC filter. All the signals are summed up together in the SQUID, which is in the same bracket with the TES and LC filter chip. The advantage of putting the SQUID in the mK stage is to minimize the electrical loom length, which decreases the readout noise and crosstalk. The signal amplitude modulated by the SQUID is then amplified by a LNA at room temperature. After going through an analog-to-digital converter (ADC), the signals are demodulated to the amplitude and phase data, which are used for analysis. Meanwhile, the data summed together with the bias carrier after adjusting the phase that is due to the delay in electronics, will perform feedback to null the input signals in the SQUID.

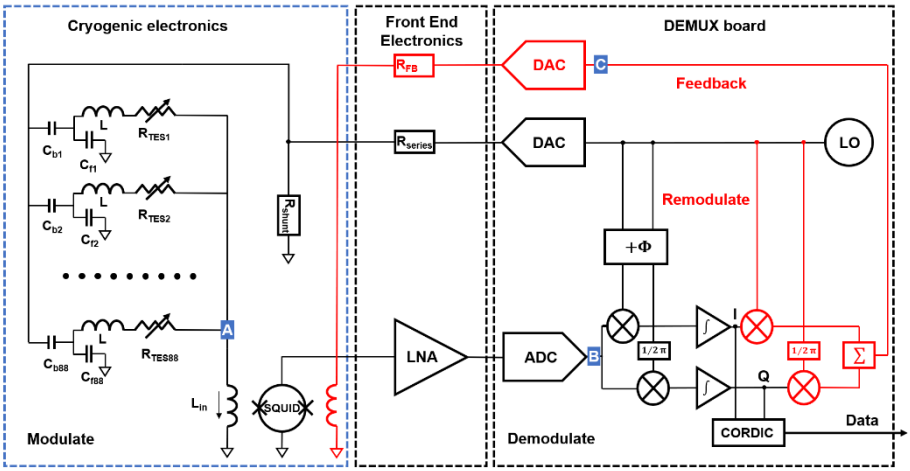

Fig. 2.4 Schematic figure of the FDM readout system. The TES array, the SQUID, and the high Q (>10^4 at 90 mK) LC filters are mounted at the mK stage inside the ADR cooler. The AC bias tones are summed up at the sum point (A) before amplification by the SQUID and the LNA (B). The re-modulation and delay correction is performed to cancel the input signal, namely, the baseband feedback (C). The modulated signal contains I and Q information for further analysis.

2.2.1 Cryogenic inductor-capacitor (LC) filters

The LC filters are a key element for the FDM system and for each pixel set an unique frequency. The purposes of the LC filters are:

(1) Filtering out all the applied comb AC bias currents for the other pixels in the TES array except for the one current. Because each LC filter has a different value capacitor, the difference of which is usually a few nF, it sets a unique frequency for each TES detector, so the different-frequency bias currents can be distinguished among TES pixels. For example, in the SAFARI FDM system, the inductance of each inductor is the same (3 μH), while the capacitance of the capacitors varies from 1 nF to 9 nF to set the unique frequency for each pixel and to keep the same frequency space (32 kHz) between two pixels [9].

(2) Making it possible to have a low-impedance voltage bias for each TES at the central frequency of its LC filter. The voltage bias of each TES pixel is

produced by the AC bias current in the shunt resistor, which is separately sent to each pixel at a different central frequency so as to bias the TES detector in its transition region and to make it possible not to interrupt other pixels even when it is broken [13].

(3) Blocking the wideband noise from other pixels. The LC filter can decrease the out-of-band noise from the other pixels in the FDM readout chain [14].

The key requirement for the LC filters is a high-quality factor Q to guarantee the voltage bias precision of the TES detectors, where the low dielectric loss capacitors and low magnetic loss inductors are needed [15]. The Q factor of an LC filter can be described as:

$$Q = \frac{\Delta f_0}{f_0} = \frac{2\pi f_0 L_{LC}}{R} = \frac{1}{R}\sqrt{\frac{L_{LC}}{C_{LC}}}. \tag{2.24}$$

where f_0 is the unique resonance frequency for the TES detector, R is the resistance of the TES circuit, which is dominated by R_{TES} when a TES is biased in transition and dominated by R_{series} when a TES is in the superconducting state, L_{LC} and C_{LC} are the inductance and capacitance of the LC filter, respectively.

The resonance frequency f_0 is determined by the parameters of an LC filter:

$$f_0 = \frac{1}{2\pi\sqrt{L_{LC}C_{LC}}}. \tag{2.25}$$

While the bias-current bandwidth of the TES is defined by the equation:

$$B = \frac{R}{2\pi L_{LC}}. \tag{2.26}$$

Therefore, the unique frequency of each TES pixel is designed by changing the value of the capacitance, while preserving the same frequency spacing and bandwidth of each TES by keeping the same inductance of each TES pixel.

Fig. 2.5 (a) shows a photo of an 88-LC filter chip used in the SAFARI FDM system, while Fig. 2.5 (b) is a diagram of one LC unit that contains two LC filters, which are far apart in resonance frequency. The design of the LC unit makes the LC filter chip more compact, which is essential for a space instrument like SAFARI [16]. The physical neighbors of the LC resonators are designed not as the frequency neighbors to eliminate mutual inductance. The inductors in the LC filter chip are formed by two Nb-based gradient spiral coils, while the capacitors consist of two Si:H-based capacitors, where one is for the bias and other is the main capacitor, the two of them having a ratio of 1:9. Detailed information about the design and fabrication can be found in [17-19]. The LC filter chip is connected with the TES chip via Al (superconducting) wire bonding.

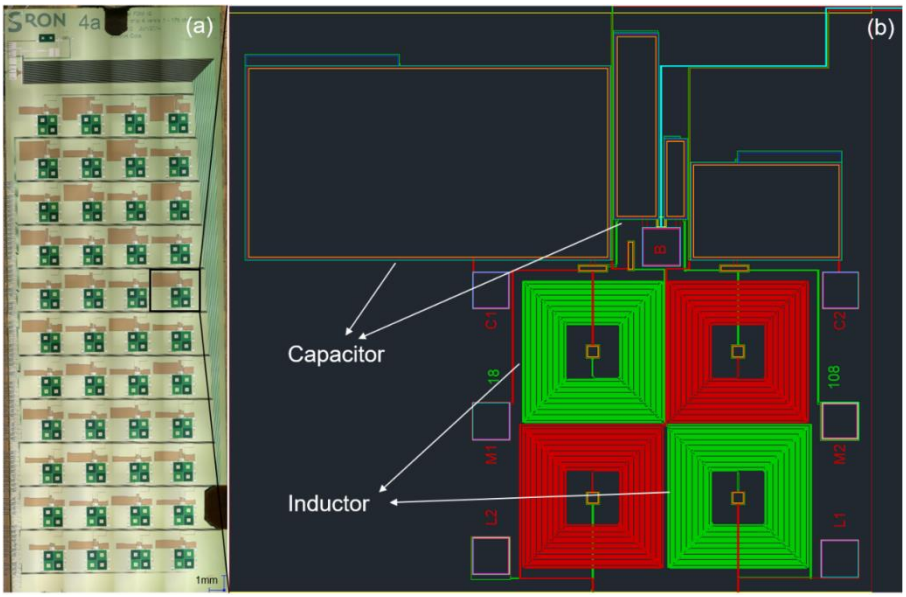

Fig. 2.5 (a) Photo of an 88-LC filter chip. There are 44 LC units where each contains two LC resonators that are not resonance frequency neighbors to keep the design compact and avoid mutual inductance. (b) Design diagram of one LC unit. Each inductor has two spiral coils, while each capacitor contains two capacitors with different values.

In the readout system, the resonance frequency ranges from 1 to 4 MHz, where the lower limit is set by the size of the capacitors and the upper limit is determined by the length of the harness wiring from the warm to the cold-stage in the setup [17]. A network analyzer (NWA) scan is performed via the AC bias line at 90 mK to detect all resonators in the readout chain, as shown in Fig. 2.6 (a). From the NWA scan, there are 65 peaks, indicating 65 resonators successfully coupled with TES and SQUID. Since at 90 mK the TESs are superconducting, the quality factor (Q) of the LC filter is limited by the series resistance.

A fine scan around the resonance peak is done to determine the resonance frequency as well as to calculate the Q factor, as shown in Fig. 2.6 (b). The calculation is done in a few steps: Firstly, apply a small amount of voltage (≤1 nV) to a TES, which acts as a signal and is low enough to keep the TES in a superconducting state. Secondly, scan the frequency of the small bias voltage over a small range (~1 kHz) around the rough peak found from the NWA scan. The peak frequency is the resonance frequency. Finally, normalize the measured data and then calculate the Q factor with Equation (2.24). With this method, the Q factors of all resonators can be quantified, as shown in Fig. 2.6 (c). The Q factors of LC filters $\geq 10^4$ indicate that these LC resonators meet the requirement of Q > 2350 f_0 (MHz) for our baseline Ti/Au based TES pixels in the arrays for the SAFARI instrument [18]. As expected from Equation (2.24), the Q factors increase with frequency since the inductance of LC filter L_{LC} and series resistance R_{series} are the same in all the resonators. Although all Q factors are higher than 10^4, there are a few resonators, whose Q factor drops from the typical values. In practice, those resonators will not be used in the measurements. The analysis of electrical crosstalk is described in Chapter 5.

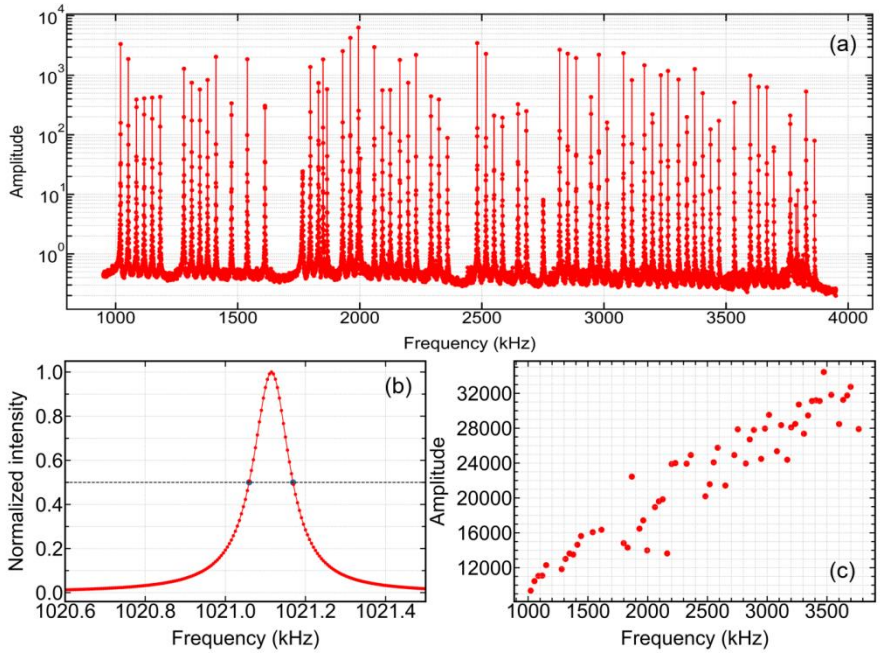

Fig. 2.6 (a) A NWA scan is applied via a bias line ranging from 900 kHz to 3900 kHz at 90 mK. There are 65 resonators detected in total. (b) Normalized fine scan data, where the peak is the resonance frequency, which can be used to calculate the Q factor. (c) The Q factors of all resonators.

2.2.2 Superconducting quantum interference devices (SQUIDs)

TES detectors are sensitive enough to detect extremely small levels of incident radiation (e.g. 1 aW), resulting in a small current change (~10 pA). Therefore, the change of the current needs to be amplified first to generate a high enough signal that can be further amplified by room-temperature electronics. DC Superconducting quantum interference devices (DC-SQUIDs) are current amplifiers that are easily impedance-matched to a low-resistance TES. SQUIDs not only can read out a single TES but also are capable of multiplexing the readout of a number of TES pixels, leading to the possibility for a large array of TES.

Flux quantization and Josephson tunneling are two physical phenomena of a SQUID amplifier [20]. Through the Josephson effect [21], a SQUID transfers a current change through the input inductor to superconducting Josephson junctions, thus generating a voltage [22]. Therefore, by applying a fixed bias current to a SQUID (DC current bias the Josephson junction), the current variation in the SQUID input coil can be measured by the change of SQUID output voltage. As shown in Fig. 2.4, a typical two-stage SQUID amplifier consists of four parts: the input coil that sums the current through the TES circuit; the Josephson junctions in a superconducting loop that generate voltage as the SQUID output; a series-array-SQUID amplifier that is used to obtain the larger voltage, which is enough to drive the room-temperature amplifier without an obvious increase in noise; and the feedback loop that is used for nulling the input signal in the SQUID.

Compared with a typical current amplifier that usually has a fixed gain, a SQUID amplifier has the non-linearity property due to its periodical and curved response function, as shown in Fig. 2.7 (a). The current in the input inductor can be calculated by the division of feedback current and turn ratio of the SQUID. The derivative of the output voltage with feedback current is shown in Fig. 2.7 (b), illustrating the non-linearity of the SQUID response. In practice, only a small, approximately linear range in the middle of positive/negative slope can be used to amplify the signal from the TES detector. Therefore, to have a larger operation range of the SQUID, feedback must be applied to null the signal in the SQUID. Details of the characterization of a SQUID by a calibration tone measurement are described in Chapter 4.

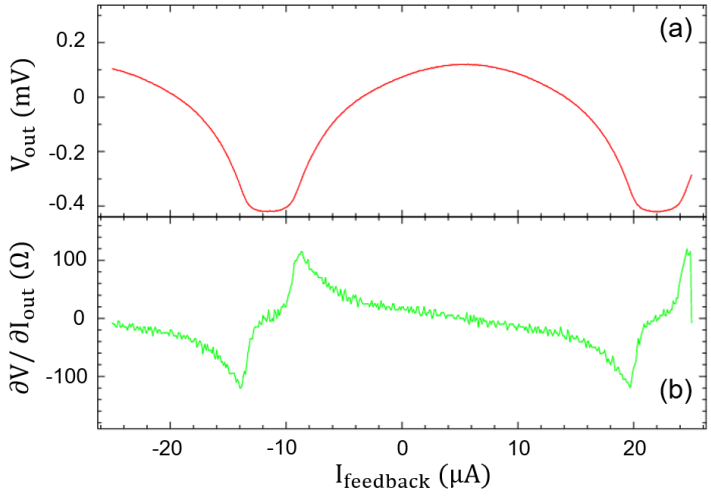

Fig. 2.7 (a) The SQUID output voltage is periodical and non-linear with the current in the input coil, which can be represented by the value of current in the feedback loop. (b) The derivative of the output voltage, which shows the non-linearity of the SQUID response.

Single-stage and two-stage SQUIDs have been used sequentially in the SAFARI FDM system [9,15,22,23]. The single-stage SQUID, which is fabricated by the National Metrology Institute of Germany (PTB) has a designed current noise of 8 pA/$\sqrt{\text{Hz}}$ [24], as shown in Fig. 2.8 (a). Fig. 2.8 (b) shows a two-stage SQUID made by the Technical Research Centre of Finland (VTT), which has a designed current noise of 3 pA/$\sqrt{\text{Hz}}$ [25,26]. In both cases, the SQUIDs are located on a designed Printed Circuit Board (PCB), operating at the same bath temperature as the TES (~50mK), which is connected to the TES chip by wire-bonds. To eliminate the out-of-band resonance (OBR), a Resistor-Capacitor (RC) low pass filter is in series with the SQUID circuit, with a resistance of 2 Ω and capacitance of 10 nF [24]. In practice, the readout noise of the single-stage SQUID is found to be 24.5 pA/$\sqrt{\text{Hz}}$, being a factor of 3 higher than the designed value. To have a higher SNR and eliminate the influence of back-action noise [9], the two-stage SQUID is then used in the SAFARI FDM system. With the same TES detectors and the warm electronics, the readout noise comparison of single-stage and two-stage SQUIDs is shown in Fig. 2.8 (c). The red lines show the measured current noise of a TES detector at different transitions while the blue lines indicate the measurement data of the same TES with a two-stage SQUID. The readout noise is 24.5 pA/$\sqrt{\text{Hz}}$ and 9.5 pA/$\sqrt{\text{Hz}}$ for the single-stage SQUID and two-stage SQUID, respectively. It is noticeable that the measured readout noise of both single-stage and two-stage SQUID are higher than the designed value. On the one hand, this is due to the additional noise from LNA, DEMUX, and excess noise in the readout chain. On the other hand, the settings of the SQUID are optimized for a stable performance other than aiming to minimize readout noise.

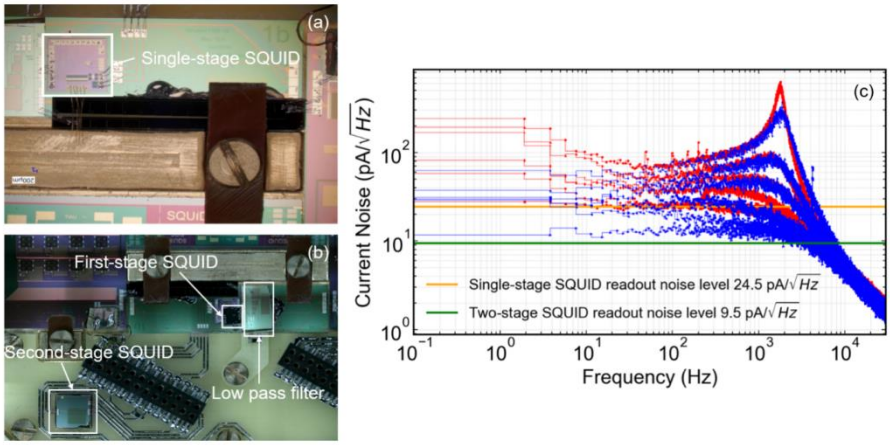

Fig. 2.8 (a) Photo of the PTB single-stage SQUID. (b) Picture of the VTT two-stage SQUID. Both SQUIDs are in the same bracket with the TES chip, and thus at the same bath temperature. (c) Noise comparison of the same TES between single-stage (red lines) and two-stage SQUID (blue lines). Different lines in the same color indicate the different noise level when the TES is biased in different transition positions. The readout noise of the single-stage SQUID is 24.5 pA/$\sqrt{\text{Hz}}$ while the readout noise of the two-stage SQUID is 9.5 pA/$\sqrt{\text{Hz}}$.

2.2.3 Room temperature electronics

The whole digital control unit (DCU) of SAFARI is described in [27,28]. In this subsection, we only focus on the warm electronics of the FDM readout system.

The warm electronics of the SAFARI FDM readout system contains mainly the Front-End-Electronics (FEE) and demultiplexer (DEMUX) board, which operate at room temperature. The core facility in the FEE box is an SiGe transistor based low noise amplifier (LNA), which has a tunable high-frequency and low-frequency gain ranging from 10 to 10000 and 10 to 1400, respectively. The LNA is connected to the SQUID via twisted pair wires from the room temperature to the mK stage. The field-programmable gate array (FPGA) in the DEMUX board controls one DAC for sinusoidal bias voltage to the TES array as well as another DAC for a feedback loop, and one ADC that transfers the measured signal to digital data [29]. A photo of the measurement

facilities is shown in Fig. 2.9 (a) while a schematic diagram of the warm electronics is shown in Fig. 2.9 (b). The connection between the DEMUX and the control computer is the optical fiber, which has better electromagnetic interference (EMI) shielding and less data loss compared to copper cables. The cables between the DEMUX and FEE are designed to have an EMI shield, and with additional EMI Noise Filter Cable Ring. The warm electronics are based on a VIRTEX V FPGA, which is for the lab demonstrator. At the moment, the warm electronics will dissipate totally about 130 W for a 3600-pixel bolometer array. For the space application, the power consumption can be considerably lowered by using an ASIC (Application Specific Integrated Circuit) based system. A discussion of the noise of the FEE and the DEMUX is reported in the next chapter.

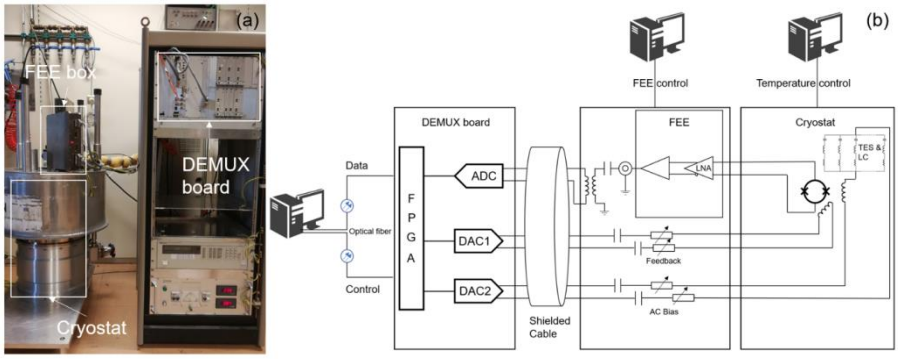

Fig. 2.9 (a) Photo of the measurement facilities in our lab, where the ADR cooler shares the same ground with the DEMUX, and the FEE box is set on the top of the cooler. (b) Diagram of the warm electronics and the cryostat.

References

[1] J. E. Sadleir, S. J. Smith, I. K. Robinson, F. M. Finkbeiner, J. A. Chervenak, S. R. Bandler, et al., "Proximity effects and nonequilibrium superconductivity in transition-edge sensors", Phys. Rev. B. **84,** 184502 (2011).

[2] R. Hijmering, P. Khosropanah, M. Ridder, M. Lindeman, L. Gottardi, M. Bruijn, et al., "Effect of Magnetic Fields on TiAu TES Bolometers for the SAFARI Instrument on the SPICA FIR Telescope", J Low Temp Phys **167,** 242–247 (2012).

[3] K. Nagayoshi, M. L. Ridder, M. P. Bruijn, L. Gottardi, E. Taralli, P. Khosropanah, et al., "Development of a Ti/Au TES Microcalorimeter Array as a Backup Sensor for the Athena/X-IFU Instrument", J. Low Temp. Phys. **199,** 943–948 (2020).

[4] J. G. Staguhn, S. H. Moseley, D. J. Benford, C. A. Allen, J. A. Chervenak, T. R. Stevenson et al., "Approaching the fundamental noise limit in Mo/Au TES bolometers with transverse normal metal bars", Nucl. Instrum. Methods Phys. Res. A. **520,** 336-339 (2004).

[5] L. Fabrega; I. F. Martinez; Ó. Gil; M. P. Borderias; A. Camon; J. L. Costa-Kramer et al., "Mo-Based Proximity Bilayers for TES: Microstructure and Properties", IEEE Trans. Appl. Supercond. **19,** 460–464 (2009).

[6] J. Montgomery, "Digital frequency domain multiplexing readout: design and performance of the SPT-3G instrument and LiteBIRD", PhD thesis, McGill University (2021).

[7] K. Irwin and G. Hilton, "Transition-Edge Sensors", Berlin, Heidelberg: Springer. 63–150 (2005).

[8] K. D. Irwin, G. C. Hilton, D. A.Wollman, and John M. Martinis. "Thermal-response time of superconducting transition-edge microcalorimeters", J. Appl. Phys. **83,** 3975-3978 (1998).

[9] Q. Wang, P. Khosropanah, J. van der Kuur, G. de Lange, M. D. Audley, A. Aminaei, et al., "Electrical crosstalk of a frequency division multiplexing readout for a transition edge sensor bolometer array", Rev. Sci. Instrum. **92,** 014710 (2021).

[10] M. L. Ridder, P. Khosropanah, R. A. Hijmering, T. Suzuki, M. P. Bruijn, H. F. C. Hoevers, et al., "Fabrication of Low-Noise TES Arrays for the SAFARI Instrument on SPICA", J Low Temp Phys. **184,** 60-65 (2016).

[11] P. Khosropanah, T. Suzuki, M. L. Ridder, R. A. Hijmering, H. Akamatsu, L. Gottardi, J. van der Kuur, J-R. Gao, B. D. Jackson, "Ultra-low noise TES bolometer arrays for SAFARI instrument on SPICA", Proc SPIE. **99140B**, (2016).

[12] D. Morozov, P. D. Mauskopf, P. Ade, M. Bruijn, P. A. J. de Korte, H. Hoevers, et al., "Ultrasensitive TES bolometers for space based FIR astronomy", AIP Conf Proc. **1185,** 48-51 (2009).

[13] M. A. Dobbs, M. Lueker, K. Aird, A. Bender, L. Bleem, J. Carlstrom, et al., "Frequency multiplexed superconducting quantum interference device readout of large bolometer arrays for cosmic microwave background measurements", Rev. Sci. Instrum. **83,** 073113 (2012).

[14] B. D. Jackson, P. de Korte, J. van der Kuur, P. Mauskopf, J. Beyer, M. Bruijn, et al., "The SPICA-SAFARI Detector System: TES Detector Arrays With Frequency-Division Multiplexed SQUID Readout", IEEE Trans. Terahertz Sci. Technol. **2,** 12–21 (2012).

[15] R Hijmering, R. den Hartog, M. Ridder, A. J. van der Linden, J van der Kuur, J. R. Gao, et al., "Readout of a 176 pixel FDM system for SAFARI TES arrays", Proc. SPIE. **99141C** (2016).

[16] M. D. Audley, G. de Lange, J. R. Gao, B. D. Jackson, R. A. Hijmering, M. L. Ridder, et al., "The SAFARI detector system", Proc. SPIE. **107080K** (2018).

[17] M. P. Bruijn, A. J. van der Linden, L. Ferrari, L. Gottardi, J. van der Kuur, R. H. den Hartog, . et al., "LC Filters for FDM Readout of the X-IFU TES Calorimeter Instrument on Athena", J Low Temp Phys. **193,** 661–667 (2018).

[18] M. P. Bruijn, L. Gottardi, R. H. Hartog, J. van der Kuur, A. J. van der Linden, and B. D. Jackson, "Tailoring the high-Q LC filter arrays for readout of kilo-pixel TES arrays in the SPICA-SAFARI instrument", J. Low Temp. Phys. **176,** 421–425 (2014).

[19] X. Yan, M. P. Bruijn, H. J. van Weers, R. A. Hijmering, J. van der Kuur, and J. R. Gao, "Modeling inductances of wiring for a TES array read by FDM", IEEE Trans. Appl. Supercond. **25,** 1–5 (2015).

[20] A. Braginski J. Clarke, "The SQUID Handbook: Fundamentals and Technology of SQUIDs and SQUID Systems", Wiley-VCH Verlag GmbH & Co. KGa, **1,** (2004).

[21] B. D. Josephson, "Possible new effects in superconductive tunnelling", Phys. Lett. **3,** 251–253 (1962).

[22] R. L. Fagaly, "Superconducting quantum interference device instruments and applications", Rev. Sci. Instrum. **77,** 101101 (2006).

[23] Q. Wang, P. Khosropanah, J. van der Kuur, G. de Lange, M. D. Audley, A. Aminaei, et al., "Frequency division multiplexing readout of 60 low-noise transition-edge sensor bolometers", submitted to Appl. Phys. Lett. (2021).

[24] M. Audley, Q. Wang, R. Hijmering, P. Khosropanah, G. de Lange, A. J. van der Linden, et al., "SQUID Noise in a 176-Pixel FDM Demonstrator for the SAFARI Far-Infrared Spectrometer", J. Low Temp. Phys. 199, 723–729 (2020).

[25] Q. Wang, P. Khosropanah, J. van der Kuur, G. de Lange, M. D. Audley, A. Aminaei, et al., "Frequency division multiplexing readout of a slow transition edge sensor bolometer array", to be submitted to Rev. Sci. Instrum. (2021).

[26] K. Mikko, G. Leif, and S. Hannu, "Two-stage locally linearized SQUID readout for frequency domain multiplexed calorimeter arrays", Supercond. Sci. Technol. **24,** 049501(2011).

[27] A. Clénet, L. Ravera, B. Bertrand, R. H. den Hartog, B. D. Jackson, B. J. van Leeuven, et al., "The DCU: the detector control unit for SPICA-SAFARI", Proc. SPIE. **914346** (2014).

[28] A. M. D. Giorgio, D. Biondi, B. Saggin, I. Shatalina, M. Viterbini, G. Giusi, et al., "The instrument control unit of SPICA SAFARI: a macro-unit to host all the digital control functionalities of the spectrometer", Proc. SPIE. **84423W** (2012).

[29] A. M. Di Giorgio, F. Nuzzolo, D. Biondi, M. D. Luca, P. C. Irelli, R. Orfei, et al., "The digital processing unit of the SPICA SAFARI instrument: an FPGA based architecture using the Leon2-FT", Proc. SPIE. **77314B** (2010).

Chapter 3

Noise Measurements of a Low-Noise Amplifier in the FDM Readout System for SAFARI

Based on

Q. Wang, M. Audley, P. Khosropanah, J. van der Kuur, G. de Lange, A. Aminaei, D. Boersma, F. van der Tak, and J. R. Gao, J. Low Temp. Phys. 199, 817-823 (2020).

The SPICA-SAFARI instrument requires extremely sensitive transition edge sensor (TES) arrays with a noise equivalent power of 2×10^{-19} W/$\sqrt{\text{Hz}}$ and a readout system with an output noise that is dominated by the detector noise. It is essential to ensure the frequency domain multiplexing (FDM) readout system in SAFARI meets the noise requirement. The FDM system in SAFARI consists essentially of LC filters, a superconducting quantum interference device, a room-temperature low noise amplifier (LNA), and a demultiplexer. Here we present a noise study of the LNA from a laboratory amplifier chain. We found the equivalent current and voltage noise of the LNA to be 5.4 pA/$\sqrt{\text{Hz}}$ and 315 pV/$\sqrt{\text{Hz}}$, respectively, which are low enough to read out SAFARI's TES arrays.

3.1 Introduction

SAFARI is a far-infrared (35–230 μm) spectrometer planned for the SPICA mission, which has a large (~2.5 m) and cold (~8 K) telescope [1]. Taking advantage of the low-temperature telescope with low emission, SAFARI is capable of detecting radiation in the sky-limited background, aiming to achieve an extraordinarily low-noise equivalent power (NEP) of 2×10^{-19} W/$\sqrt{\text{Hz}}$ [2]. SAFARI plans to use frequency domain multiplexing (FDM) to read transition edge sensor (TES) arrays [3]. Therefore, the key requirement of the readout system is that its noise should be lower than the detector signal. The readout noise of the FDM system is expected to be dominated by the current noise of the SQUID and the noise of the LNA.

To evaluate the noise contribution from the LNA, we need to measure the current noise and the voltage noise of the LNA. Extracting these noise sources from the measured output noise is complicated because the output noise depends not only on these noise sources but also on the SQUID noise and the loading impedance at the input of the amplifier, both of which are determined by the SQUID settings. So we need to measure the noise of the LNA separately. This paper reports the output noise of the LNA measured with different resistors ranging from 10 to 400 Ω at different temperatures (50 mK and 1.3 K) at the input. The current noise and voltage noise of the LNA are estimated from the fitting of the measurements with a noise model. To verify the fitting parameters, a room-temperature open- and shorted-circuit measurement is also taken.

3.2 Measurement Setup

The LNA used is homemade and is part of an SRON front-end electronics (FEE), which has 74 dB gain in the range 1–5 MHz and active input impedance for impedance match. The SQUID in our study is a single-stage PTB (The National Metrology Institute of Germany) SQUID which contains a 16-element SQUIDs array. The load resistors are placed in the mK stage of a Leiden Cryogenics (LC) dilution cooler and are connected with the LNA via a loom that goes from the top of the cooler to its bottom [4,5]. The load resistors are introduced to replace the SQUID, to simulate the dynamic impedance of the SQUID. In this way, there is no current noise contribution of the SQUID, and we can measure LNA noise contribution with a set of representative interfaces. As illustrated in Fig. 3.1, there are 10 load resistors on a homemade printed circuit board (PCB). By

connecting a different load resistor, we can simulate different load impedances of the SQUID at the input of the LNA. The measured output noise consists of the voltage noise and the current noise of the LNA, which are the aim of this work, and also the Johnson thermal noise from both the load resistors and the loom.

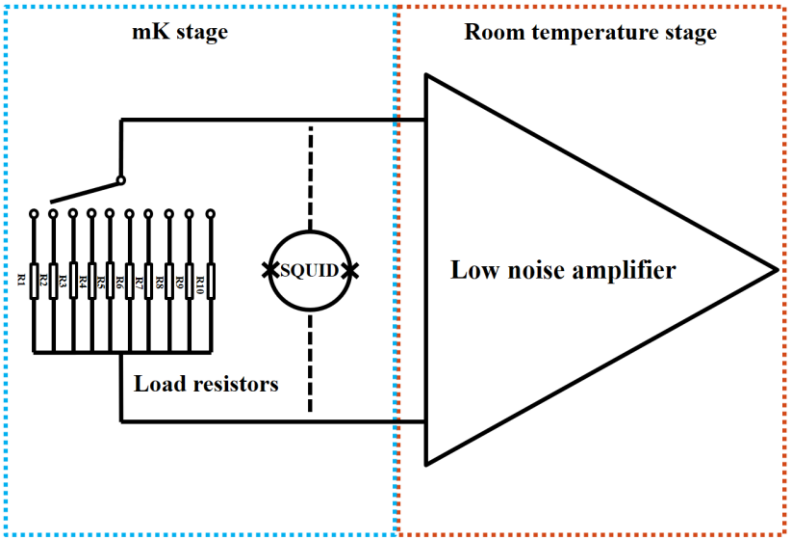

Fig. 3.1 Simplified circuit scheme between the LNA and the load resistors. The latter range from 10 to 400 Ω and are placed in the mK stage to simulate the SQUID. The dashed line means the SQUID is not connected.

3.3. Noise Measurement Results and Analysis

3.3.1. Offset Noise of DEMUX

In our FDM system, the DEMUX is used not only to provide a digital-to-analog converter (DAC), which supports the 1-4 MHz AC bias to TESs, but also has an analog-to-digital converter (ADC), which records the readout noise [6]. Hence, it is important to do a measurement first to quantify the noise from the DEMUX. The measurement can be realized by varying the high-frequency (HF) gain from the LNA.

If the noise from the DEMUX is zero, one could measure zero readout noise with the zero gain, but if there is a certain noise from the DEMUX, there will be an offset noise when the gain approaches zero. Fig 3.2 shows our measured readout noise as a function of the high-frequency (HF) gain of the LNA. The offset noise of the DEMUX is seen to dominate when the HF gain is lower than 1000. The offset noise is 173 $\pm$ 1 nV/$\sqrt{\text{Hz}}$ in our case. The noise data are obtained from the readout noise averaged in the range of 1 to 2 MHz, to be of interest in our FDM study. The fitted lines to the low-temperature (1.3 K) and higher-temperature (4 K) data of load resistors are identical within $\pm$1 nV/$\sqrt{\text{Hz}}$ error. Because of this offset noise, we always set the HF gain higher than 1000. Since we use a 2:1 transformer, the real gain is a factor of two lower than the setting gain.

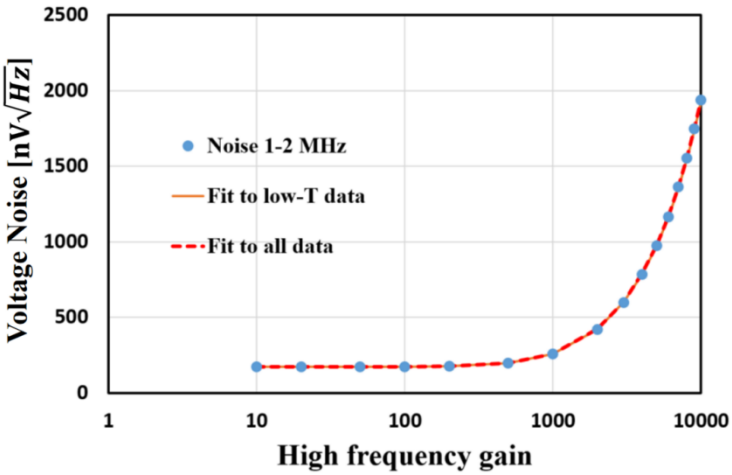

Fig. 3.2 Measured noise versus the HF gain, plotted on a logarithmic scale. The offset noise value of the DEMUX is 173 nV/$\sqrt{\text{Hz}}$. The measured noise depends linearly on the high-frequency (HF) gain when the gain is larger than 1000.

3.3.2. Noise Results and Model

Noise measurements of the LNA are performed under an open-loop condition (without feedback in the warm electronics) with the load resistance at 50 mK or 1.3 K, respectively. During these measurements, we change the value of the input

impedance R_{in} for the LNA, which has a value of 40, 50, 70, 88, 109, 129 Ω. The LNA noise consists of a voltage noise V_n and a current noise I_n.

The practical scheme of the LNA is rather complex, but we simplify it by modifying a common noise model [7] to calculate its noise, which is shown in Fig. 3.3. According to this noise model, the noise of the DEMUX is independent of the HF gain and increases the total readout noise level, so the V_{DEMUX} contributes an offset of the readout noise. Both the current noise and the voltage noise of the LNA, as well as the Johnson noise from the source resistance R_s, are amplified by the HF gain. The R_s consists of the load resistance and the resistance of the leads in the loom, both of which are known. One complication of R_s is that the load resistor and the electrical leads in the loom are at different cryogenic temperatures. So, the Johnson noise of the load resistor and the leads should be dealt with at two temperatures. The Johnson noise from input impedance can be negligible because it is not amplified by the LNA. This leads to Equation (3.1) to derive the LNA noise:

$$V_{measured} = \sqrt{V_{DEMUX}^2 + Gain^2 \cdot \left[(I_n^2 \cdot R_s^2 + V_n^2 + 4 \cdot k_B \cdot T \cdot (R_s - R_{lead}) + 4 \cdot k_B \cdot T_{lead} \cdot R_{lead}) \cdot \left(\frac{R_{in}}{R_{in} + R_s} \right)^2 \right]}, \quad (3.1)$$

where k_B is the Boltzmann constant, T is the temperature of the load resistance, and T_{lead} is the average temperature of the leads. When it is not at room temperature, the average temperature of the leads is 100 K, as estimated from the different lengths in different temperature stages.

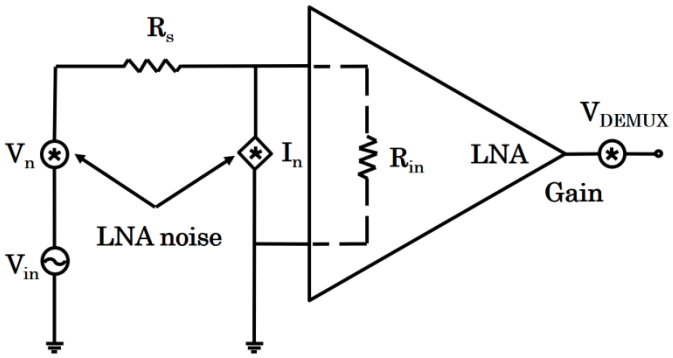

Fig. 3.3 Simplified noise model for the LNA. A current noise source and a voltage noise source are considered.

3.3.3. Fit Line of the Measured Output Noise at 50 mK and 1.3 K

We plot the measured voltage noise versus source resistance at 50 mK (HF gain 1000) and 1.3 K (HF gain 5000) in Figs. 3.4 and 3.5, respectively, together with the fits using Equation (3.1). The different gain values are chosen to test whether the equation holds for various gain settings. The current noise and voltage noise are the fitting parameters. The best fits in Fig. 3.4 give the current noise and voltage noise of the LNA to be 5.4 ± 0.1 pA/$\sqrt{\text{Hz}}$ and 315 ± 10 pV/$\sqrt{\text{Hz}}$, respectively.

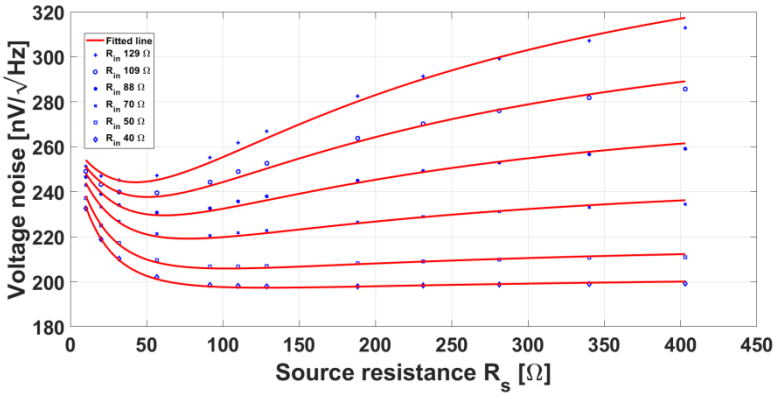

Fig. 3.4 At 50 mK, output noise as a function of R_s with different R_{in}. The fit line corresponds to R_{in} ranging from 40 to 129 Ω. The data measured at 50 mK fit well with the noise model by modifying the value of the current noise and voltage noise of the LNA. The fitted current noise is 5.4 ± 0.1 pA/$\sqrt{\text{Hz}}$, while the fitted voltage noise 315 ± 10 pV/$\sqrt{\text{Hz}}$.

The best fits in Fig. 3.5 illustrate the identical (within the uncertainty) current noise and the voltage noise of the LNA as what we found from 50 mK data, confirming the model. Thus, we have now derived the noise data of our LNA.

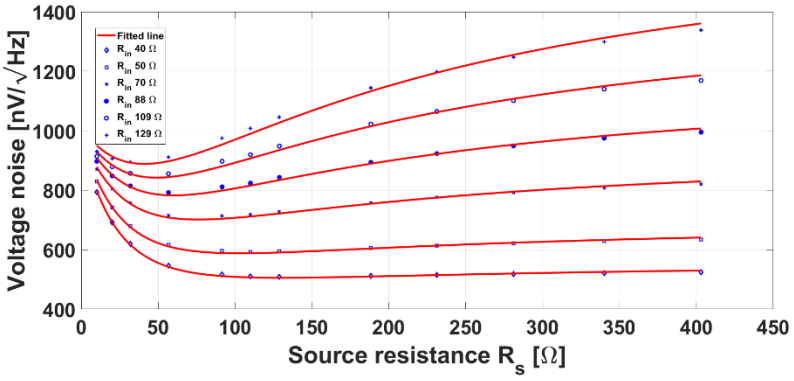

Fig. 3.5 At 1.3 K, the output noise as a function of R_s with different R_{in}. The fitted current noise is 5.4 ± 0.1 pA/$\sqrt{\text{Hz}}$, while the fitted voltage noise 315 ± 10 pV/$\sqrt{\text{Hz}}$, both identical to the fitted parameters at 50 mK.

3.3.4. Open and Shorted Measurement at Room Temperature

Either an open- or shorted-circuit room-temperature measurement is taken to verify the noise model (HF gain 5000). The fitted current noise and voltage noise of the LNA are 5.4 pA/$\sqrt{\text{Hz}}$ and 303 pV/$\sqrt{\text{Hz}}$, as illustrated in Fig. 3.6. The current noise estimated from the fit of the open-circuit measurement is identical to the LNA noise extracted from the low-temperature measurements. However,

the fitted voltage noise has a 10 pV/$\sqrt{\text{Hz}}$ difference with the estimated voltage noise, which is probably due to the nonzero resistance in the shorted circuit and a systematic error in the estimation of the cable noise contribution.

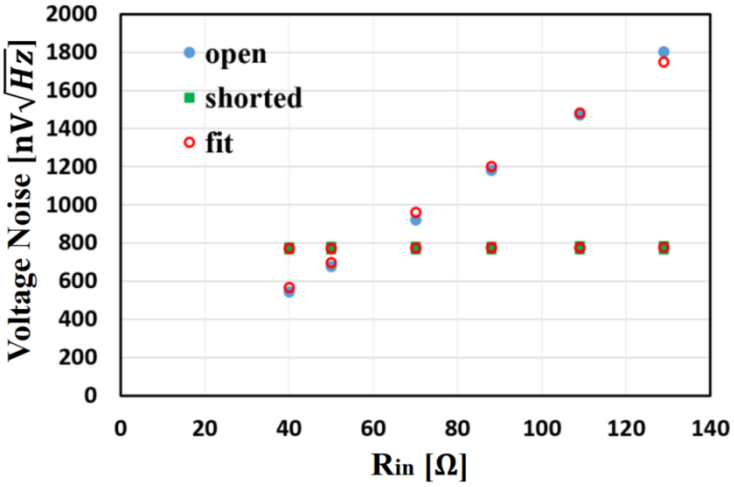

Fig. 3.6 Readout noise as a function of input impedance in open- and shorted-circuit measurement at room temperature. The resistance of open and shorted circuit is about 3 MΩ and 0.5 Ω , respectively. The fitted current noise is 5.4 pA/$\sqrt{\text{Hz}}$ and voltage noise 303 pV/$\sqrt{\text{Hz}}$.

3.3.5. Noise Temperature of LNA and SQUID Noise

The noise temperature of the LNA can be calculated by Equation (3.2):

$$T_n = \frac{(V_n^2 + I_n^2 \cdot R_c^2)}{4 \cdot k_B \cdot R_c}. \tag{3.2}$$

Using the voltage noise and current noise estimated from the fitted lines and the R_s of 100 Ω (~SQUID transresistance), the noise temperature of the LNA is 80 K. With a SQUID dynamic resistance of ~150 mΩ, the voltage noise of LNA (310 pV/$\sqrt{\text{Hz}}$) is transferred to 2 pA/$\sqrt{\text{Hz}}$ current noise. Therefore, the total

current noise of LNA is 7.4 pA/$\sqrt{\text{Hz}}$. The estimated intrinsic SQUID current noise is 5 pA/$\sqrt{\text{Hz}}$, which is smaller than the noise of LNA. The estimated current noise of the SQUID corresponds to approximately 100 Ω SQUID transresistance at < 80 K, thus, our initial idea is that the noise of the readout is dominated by the LNA noise. However, as described in [8], the total readout noise referred to the input of the SQUID is about 18 pA/$\sqrt{\text{Hz}}$, depending on the operating conditions and the presence of the LC filters. This total readout noise is calculated by quadratically adding LNA noise and SQUID noise, which indicating the noise from SQUID is 16 pA/$\sqrt{\text{Hz}}$. Therefore, our readout noise is dominated by the noise from the SQUID.

If we use relatively slow (time constant ~40 ms) TES devices and bias them to the low-transition region, the output noise of the TES will be well above the noise of the readout.

3.4. Conclusion

The noise measurements of the LNA can be well explained with a simple noise model with equivalent noise sources as fitting parameters. The extracted current noise and the voltage noise of the LNA are 5.4 ± 0.1 pA/$\sqrt{\text{Hz}}$ and 315 ± 10 pV/$\sqrt{\text{Hz}}$, respectively. The noise temperature of the LNA is 80 K with 100 Ω resistance. The offset voltage noise of the DEMUX is 173 ± 1 nV/$\sqrt{\text{Hz}}$. We found that the noises of the LNA are low enough to read out SAFARI's TES arrays.

References

[1] P. R. Roelfsema, H. Shibai, L. Armus, D. Arrazola, M. Audard, M. D. Audley, et al., "Spica-a large cryogenic infrared space telescope: Unveiling the obscured universe", Publ. Astron. Soc. Aust. **35,** E030 (2018).

[2] B. D. Jackson, P. de Korte, J. van der Kuur, P. Mauskopf, J. Beyer, M. Bruijn, et al., "The SPICA-SAFARI Detector System: TES Detector Arrays With Frequency-Division Multiplexed SQUID Readout", IEEE Trans. Terahertz Sci. Technol. **2,** 12–21 (2012).

[3] R Hijmering, R. den Hartog, M. Ridder, A. J. van der Linden, J van der Kuur, J. R. Gao, et al., "Readout of a 176 pixel FDM system for SAFARI TES arrays", Proc. SPIE **99141C** (2016).

[4] M. D. Audley, G. de Lange, J. R. Gao, P. Khosropanah, R. Hijmering, M. Ridderet, et al., "Optical performance of an ultra-sensitive horn-coupled transition-edge-sensor bolometer with hemispherical backshort in the far infrared", Rev. Sci. Instrum. **87,** 043103 (2016).

[5] M. D. Audley, G. de Lange, L. Ferrari, J.-R. Gao, R. A. Hijmering, P. Khosropanah, et al., "Performance of a Low-Noise Test Facility for the SAFARI TES Bolometer Arrays", J. Low Temp. Phys. **167,** 208 (2012).

[6] R. Hijmering, R. H. den Hartog, A. J. van der Linden, M. Ridder, M. P. Bruijn, J. van der Kuur, et al., "The 160 TES bolometer read-out using FDM for SAFARI", Proc. SPIE **9153,** 91531E (2014).

[7] B. I. Ivanov, M. Trgala, M. Grajcar, E. Il'ichev, and H. G. Meyer, "Cryogenic ultra-low-noise SiGe transistor amplifier", Rev. Sci. Instrum. **82,** 104705 (2011).

[8] M. Audley, Q. Wang, R. Hijmering, P. Khosropanah, G. de Lange, A. J. van der Linden, et al., "SQUID Noise in a 176-Pixel FDM Demonstrator for the SAFARI Far-Infrared Spectrometer", J. Low Temp. Phys. **199,** 723–729 (2020).

Chapter 4

SQUID Noise in a 176-Pixel FDM Demonstrator for the SAFARI Far-Infrared Spectrometer

Based on

M. Audley, Q. Wang, R. Hijmering, P. Khosropanah, G. de Lange, A. J. van der Linden, M. L. Ridder, and E. Taralli, J. Low Temp. Phys. ***199,*** *723–729 (2020).*

We are developing the frequency-domain multiplexing (FDM) readout for the SAFARI far-infrared spectrometer on board the SPICA space observatory. Each readout channel comprises a set of ~160 TESs and LC filters and is read out with a SQUID preamplifier. Baseband feedback is applied to overcome the dynamic range limitations of the SQUID. We have carried out extensive characterization of a test readout system coupled to a 176-pixel TES bolometer array in order to understand and optimize the system. We present our latest measurements of this 176-pixel FDM demonstrator, focusing on the noise contribution from the SQUID.

4.1. Introduction

The Space Infrared Telescope for Cosmology and Astrophysics (SPICA) [1], a candidate mission for the European Space Agency (ESA) M5 program, will use a large (2.5 m diameter) primary mirror cooled to ≤ 8 K to enable high-spectral-resolution, sky-background-limited observations of the cold dusty Universe in the mid- and far-infrared. SPICA's prime instrument is the SAFARI (SPICA Far-infrared Instrument) spectrometer. SAFARI will cover the spectral range $\lambda = 34–230\ \mu m$ simultaneously with four grating modules, each containing a diffraction grating and linear detector array to sample the dispersed spectrum [2]. The dispersed spectra are measured with linear arrays of transition-edge sensor [3] (TES) bolometers. The four detector arrays will contain a total of ~3500 TES detectors. We have demonstrated the required NEP ($\leq 2 \times 10^{-19}\ W/\sqrt{Hz}$) [4] and optical efficiency (≥ 50%) [5] for single detectors fabricated at SRON [6].

SAFARI's TES bolometers are biased with an AC voltage and read out with SQUID preamplifiers. To reduce the wire count and the heat load on the system, SAFARI uses frequency-domain multiplexing (FDM) with baseband feedback [7, 8]. There are 24 readout channels, each reading out 160 detectors using a two-stage SQUID preamplifier and a higher-temperature low-noise amplifier (LNA). The current noise

contribution (referred to the input coil of the SQUID preamplifier) from the flight readout is required to be less than $\sim 10\ pA/\sqrt{Hz}$ [7].

This paper describes measurements of the noise in a 176-pixel demonstrator for the SAFARI FDM readout. Because we are using a single-stage SQUID, we do not expect to meet SAFARI's readout noise requirement in this setup. The noise requirements for this setup are looser than the flight case; we require the readout noise of our experimental setup to be low enough for us to measure the intrinsic noise in the TESs, i.e., less than $\sim 30\ pA/\sqrt{Hz}$.

4.2. The SAFARI FDM Readout with Baseband Feedback

The FDM readout scheme is shown in Fig. 4.1. The TESs are connected in series with narrow band-pass cryogenic lithographic LC filters designed and fabricated at SRON [9]. The room-temperature SRON Demux electronics generate a comb of tones with frequencies ranging from ~1 to ~4 MHz. Each of

these tones is tuned to match the resonant frequency of one of the LC filters and provides an AC voltage bias to the corresponding TES. The LC filters also reject wideband Johnson noise in the circuit. All the TES bias signals can be adjusted independently so that all detectors are biased optimally, mitigating the effects of detector non-uniformity across an array.

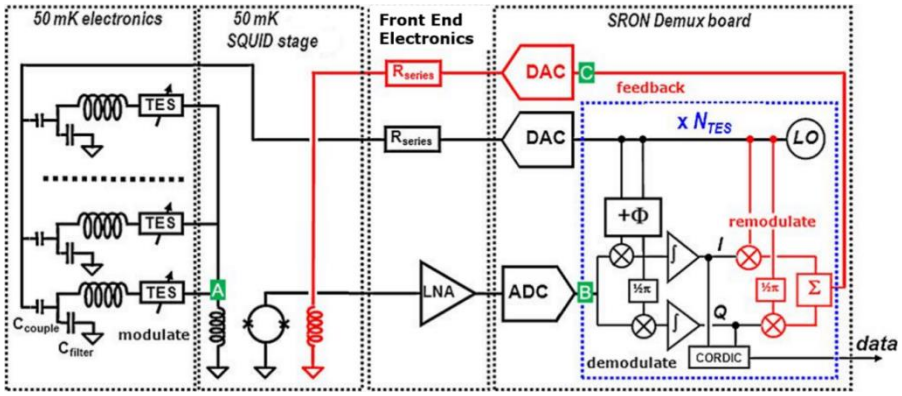

Fig. 4.1 FDM readout scheme.

The TES currents are summed at the input coil of a SQUID preamplifier (point A in Fig. 4.1). In the FDM demonstrator setup described in this paper, the TES currents are read out with a single-stage SQUID at the base temperature (50 mK). In the final instrument, a second SQUID amplifier stage on the 1.8 K temperature level of the grating module provides additional amplification. The signal that appears at the output of the SQUID is essentially an amplitude-modulated version of the AC bias signal, with a phase shift due to the electronics. After further amplification by an LNA at a higher temperature, the signal (point B in Fig. 4.1) is demodulated and a comb of frequencies is generated with the appropriate phases and amplitudes to cancel out the SQUID output when applied to the feedback coil of the front-end SQUID. This feedback signal (point C in Fig. 4.1) is linearly proportional to the power absorbed by each TES bolometer. The feedback is carried out on the amplitude of the generated tones. Since this amplitude varies no faster than the bandwidth of the TES, this scheme is known as baseband feedback.

4.3. 176-Pixel FDM Demonstrator

4.3.1. Experimental Setup

The resonance frequencies are distributed alternately between two LC filter chips on either side of the TES array to improve the isolation of frequency neighbors. This reduces crosstalk due to the mutual inductance of the coplanar wiring. The carrier separation is 16 kHz. The 176-pixel array contains 163 usable TES bolometers plus eight resistors for calibration. The TES bolometers are Au/Ti bilayers on silicon nitride membranes with Ta absorbers. The TESs have a transition temperature $T_c \approx 107$ mK and a design saturation power of 20 fW for a bath temperature of 65 mK and an NEP of 7×10^{-19} W/$\sqrt{\text{Hz}}$. The 176-pixel experiment is mounted in a cryogen-free adiabatic demagnetization refrigerator in a lighttight box with magnetic shielding. The array is read out with a single-stage SQUID [10] fabricated at Physikalisch-Technische Bundesanstalt (PTB) in Berlin, and the SQUID is read out using SRON room-temperature electronics. We have previously demonstrated multiplexed readout of 132 pixels using this setup [11].

4.4. Readout Noise Measurements

Recently, we have been investigating the noise contributions in the readout of the 176-pixel FDM demonstrator. We started by characterizing the noise in the room temperature LNA of the SRON front-end electronics (FEE) [12]. Given the intrinsic flux noise ($\sim 0.2\ \mu\Phi_0/\sqrt{\text{Hz}}$) of the SQUID and the measured LNA noise, we would expect the readout noise in this 176-pixel demonstrator to be LNA-dominated. To investigate this, and to obtain a global picture of the SQUID noise, we carried out systematic measurements of the output voltage noise of the system for a range of SQUID bias and feedback current values.

In order to compare our measurements with the expected flux noise of the SQUID, we used the SRON room-temperature electronics to apply a MHz-range AC signal to the SQUID feedback. The peak-to-peak amplitude of this calibration tone was chosen so that it caused a flux excursion in the SQUID of about 1% of a magnetic flux quantum (Φ_0). This enabled us to calculate the flux noise from the output voltage noise (integrated over a small line-free region of the spectrum near the calibration tone). The calibration tone was chosen to be large enough to be visible in the output spectrum, but small enough that the SQUID response

would be nearly linear, minimizing power loss into harmonics. We set the calibration tone amplitude as follows. First, we applied a small-amplitude tone to the SQUID feedback coil and observed the output of the LNA (point B in Fig. 1) in the time domain. For small tone amplitudes, the SQUID response was approximately linear so the output was sinusoidal. As the amplitude was increased, the output became distorted and we began to see dips at the peaks and troughs of the output sinusoid where the tone was sweeping past a maximum or minimum of the sinusoidal V– Φ curve of the SQUID.

In this way, it was possible to adjust the amplitude of the tone so that it swept out a complete flux quantum. The amplitude was then reduced by a factor of 100 to give a tone with a flux amplitude of 0.01 Φ_0. Since we wanted to measure the broadband noise level, we chose the frequency of the calibration tone (typically ~1.55 MHz) to lie in a line-free region of the noise spectrum, avoiding the LC resonances and other features. The noise level was taken as the mean over a small line-free region (1.6–1.7 MHz) near the calibration tone. This enabled us to measure the flux noise, which could be converted into current noise referred to the SQUID input coil using the known mutual inductance of the SQUID input coil.

The noise measurements were taken in open-loop mode, i.e., without the baseband feedback applied. These noise measurements were taken for three different configurations: nothing connected to the input coil of the SQUID ("Bare SQUID"); one half of the LC filters and TESs connected ("Half Array"); and the Half-Array configuration with a lowpass filter across the SQUID input coil ("Half Array with Snubber").

4.4.1. Bare SQUID Versus Half Array

In order to isolate the causes of readout noise in the demonstrator, we first disconnected the SQUID from the LC filters and then reconnected one of the LC filter chips (88 resonators). As shown in Fig. 4.2, reconnecting the Half Array increases the voltage noise and reduces the AC transfer. The effect is much larger at mK temperatures, especially at the peaks and troughs of the V– Φ curve. The cause of this temperature dependence is unclear. We see the same noise below and just above the transition temperature of the TESs, so it does not appear to be due to the quality factor of the LC resonators changing. A possible cause is that there is less damping at mK temperatures because the Al wire bonds are superconducting. This led us to suspect that out-of-band resonances in the SQUID input circuit might be involved. The performance of SQUID amplifiers is

known to be affected by parasitic capacitance in the input circuit as well as loading of the input circuit [13]. The parasitic capacitance leads to resonances in the SQUID loop and hysteresis in the I–V curves accompanied by excess noise [14].

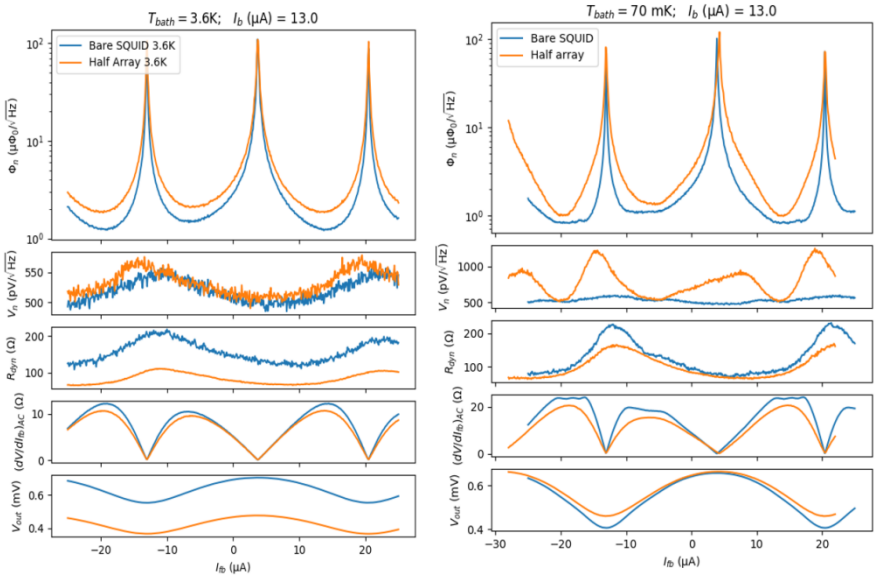

Fig. 4.2 SQUID noise vs feedback current for Bare SQUID and Half-Array configurations at two different temperatures. Left: 3.6 K. Right: 70 mK. From top: SQUID flux noise; output voltage noise; DC dynamic resistance; AC transresistance; and DC V– Φ curve.

4.4.2. Half Array with Snubber

We added an RC snubber, i.e., a low-pass RC filter (2 Ω, 10 nF), across the summing point at the SQUID input coil in order to block the out-of-band resonances. This approach has previously been found to result in smoother V– Φ curves and lower noise [14]. As shown in Fig. 4.3, the snubber reduces the readout noise so that we recover the performance of the Bare-SQUID configuration at the high-transfer bias points. At 3.6 K, the voltage noise is higher than for the Bare SQUID (except at the V– Φ curve minimum), but the higher AC

transresistance compensates for this. The behavior is different at mK temperatures: The snubber suppresses the excess voltage noise almost completely near the maximum of the V– Φ curve, but we still see significantly increased voltage noise near the minimum of the V– Φ curve.

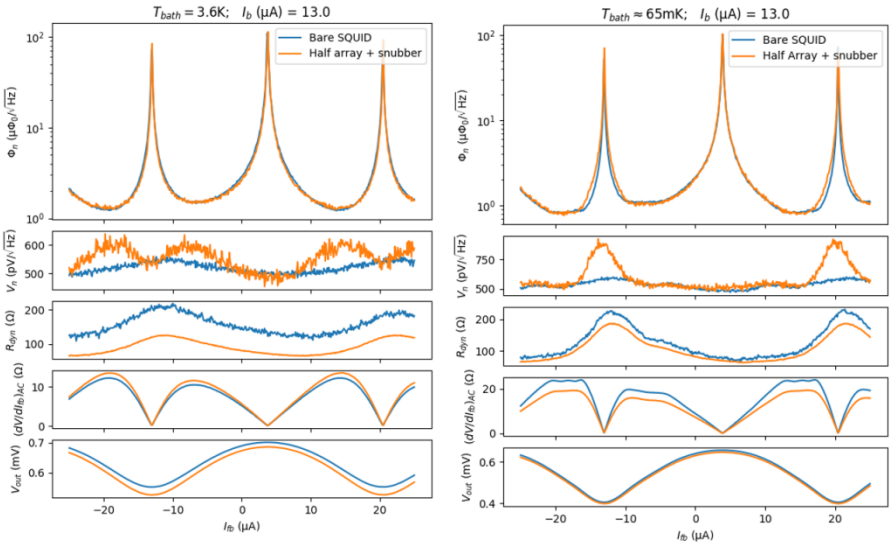

Fig. 4.3 SQUID noise versus feedback current for the Bare-SQUID and Half Array with Snubber configurations measured at two different temperatures. Left: 3.6 K. Right: 65 mK.

4.5. Discussion and Conclusions

Connecting the LC filters and TESs to the SQUID input coil results in an increase in output voltage noise, which is worse at mK temperatures where the quality factor is higher. Since the snubber mitigates this, we conclude that this excess noise is likely due to out-of-band resonances. With the snubber installed, we recover the Bare-SQUID performance at the high-transfer set points.

Fig 4.4 shows usable bias points with input-referred current noise of 15 – 20 pA/$\sqrt{\text{Hz}}$, meeting our requirement of 30 pA/$\sqrt{\text{Hz}}$ and allowing us to measure the intrinsic TES noise comfortably. We plan to replace the single-stage SQUID

with a two-stage SQUID to improve this further. LNA noise can account for the output voltage noise at the high-transfer set points if the MHz dynamic resistance is slightly higher than the DC value. We know from measurements of this LNA that the current noise is significant in addition to the voltage noise [12]. We intend to investigate this further by modeling the circuit and by reconfiguring the readout so that we can measure the AC dynamic resistance. However, there is still excess noise at the minimum of the V– Φ curve that cannot be accounted for by a high AC dynamic resistance (Fig. 4.4).

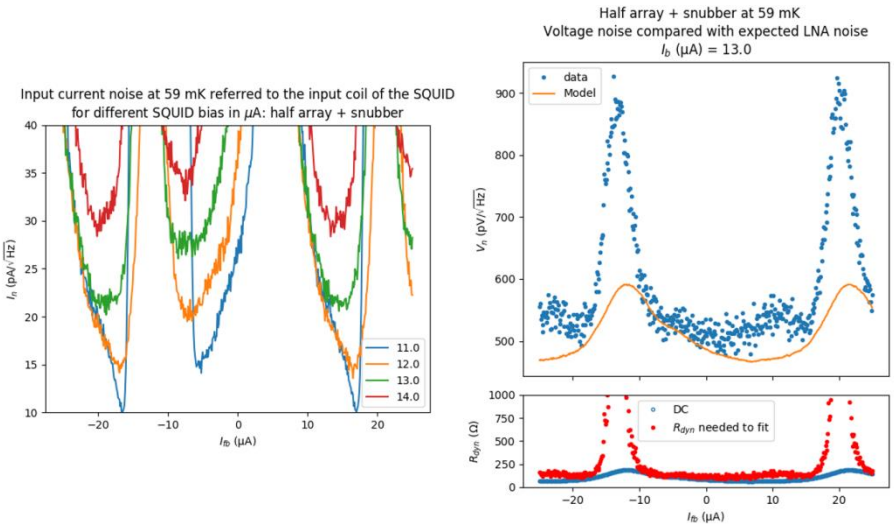

Fig. 4.4 Noise for Half Array with Snubber. Left: input-referred current noise. Upper right: measured and expected [12] voltage noise. Lower right: dynamic resistance measured and needed to account for measured voltage noise.

In practice, this does not affect the operation of the SQUID amplifier, as it occurs where the AC transfer is low. Nevertheless, it is unclear why we recover the Bare-SQUID noise performance at the peaks of the V– Φ curve, but not at the troughs. The interaction between input circuit resonances and the SQUID is complicated [15], and a detailed analysis is outside the scope of this work. However, we note that the circulating currents in the SQUID at the peak and trough will be different and speculate that this may be involved.

References

[1] P. R. Roelfsema, H. Shibai, L. Armus, D. Arrazola, M. Audard, M. D. Audley, et al., "Spica-a large cryogenic infrared space telescope: Unveiling the obscured universe", Publ. Astron. Soc. Aust. **35,** E030 (2018).

[2] M. D. Audley, G. de Lange, J. R. Gao, B. D. Jackson, R. A. Hijmering, M. L. Ridder, et al., "The SAFARI detector system", Proc. SPIE. **107080K** (2018).

[3] K. Irwin and G. Hilton, "Transition-Edge Sensors", Berlin, Heidelberg: Springer. 63–150 (2005).

[4] P. Khosropanah, T. Suzuki, M. L. Ridder, R. A. Hijmering, H. Akamatsu, L. Gottardi, J. van der Kuur, J-R. Gao, B. D. Jackson, "Ultra-low noise TES bolometer arrays for SAFARI instrument on SPICA", Proc SPIE. **99140B**, (2016).

[5] M. D. Audley, G. de Lange, J. R. Gao, P. Khosropanah, R. Hijmering, M. Ridderet, et al., "Optical performance of an ultra-sensitive horn-coupled transition-edge-sensor bolometer with hemispherical backshort in the far infrared", Rev. Sci. Instrum. **87,** 043103 (2016).

[6] M. L. Ridder, P. Khosropanah, R. A. Hijmering, T. Suzuki, M. P. Bruijn, H. F. C. Hoevers, et al., "Fabrication of Low-Noise TES Arrays for the SAFARI Instrument on SPICA", J Low Temp Phys. **184,** 60-65 (2016).

[7] R. den Hartog, M. D. Audley, J. Beyer, D. Boersma, M. Bruijn, L. Gottardi, et al., "Low-Noise Readout of TES Detectors with Baseband Feedback Frequency Domain Multiplexing", J. Low Temp. Phys. **167,** 652-657 (2012).

[8] R. den Hartog, M. D. Audley, J. Beyer, M. P. Bruijn, P. de Korte, L. Gottardi, et al., "Frequency division multiplexed readout of TES detectors with baseband feedback", Proc. SPIE. **8452,** 84520F (2012).

[9] M. P. Bruijn, L. Gottardi, R. H. den Hartog, J. van der Kuur, A. J. van der Linden, and B. D. Jackson, "Tailoring the High-Q LC Filter Arrays for Readout of Kilo-Pixel TES Arrays in the SPICA-SAFARI Instrument", J. Low Temp. Phys. **176,** 421–425 (2014).

[10] D. Drung, C. Abmann, J. Beyer, A. Kirste, M. Peters, F. Ruede, et al., "Highly Sensitive and Easy-to-Use SQUID Sensors", IEEE Trans. Appl. Supercond. **17,** 699-704 (2007).

[11] R Hijmering, R. den Hartog, M. Ridder, A. J. van der Linden, J van der Kuur, J. R. Gao, et al., "Readout of a 176 pixel FDM system for SAFARI TES arrays", Proc. SPIE **99141C** (2016).

[12] Q. Wang, M. Audley, P. Khosropanah, J. van der Kuur, G. de Lange, A. Aminaei, et al., "Noise Measurements of a Low-Noise Amplifier in the FDM Readout System for SAFARI", J. Low Temp. Phys. **199,** 817-823 (2020).

[13] C. Hilbert, and J. Clarke, "Measurements of the dynamic input impedance of a dc SQUID", J. Low Temp. Phys. **61,** 237–262 (1985).

[14] J. Knuutila, A. Ahonen, and C. Tesche, "Effects on DC SQUID characteristics of damping of input coil resonances", J. Low Temp. Phys. **68,** 269–284 (1987).

[15] T. Ryhänen, and H. Seppä, "Effect of parasitic capacitance and inductance on the dynamics and noise of dc superconducting quantum interference devices", J. Appl. Phys. **71,** 6150 (1992).

Chapter 5

Electrical crosstalk of a frequency division multiplexing readout for a transition edge sensor bolometer array

Based on

Q. Wang, P. Khosropanah, J. van der Kuur, G. de Lange, M. D. Audley, A. Aminaei, R. Hijmering, M. L. Ridder, S. Ilyas, A. J. van der Linden, M. P. Bruijn, F. van der Tak, and J. R. Gao, Rev. Sci. Instrum. 92, 014710 (2021), which is one of the editor pick papers.

We have characterized and mapped the electrical crosstalk (ECT) of a frequency division multiplexing (FDM) system with a transition edge sensor (TES) bolometer array, which is intended for space applications. By adding a small modulation at 120 Hz to the AC bias voltage of one bolometer and measuring the crosstalk response in the current noise spectra of the others simultaneously, we have for the first time mapped the ECT level of 61 pixels with a nominal frequency spacing of 32 kHz in a 61× 61 matrix and a carrier frequency ranging from 1MHz to 4 MHz. We find that about 94% of the pixels show an ECT level of less than 0.4%. Only the adjacent pixels reach this level, and the ECT for the rest of the pixels is less than 0.1%. We also observe higher ECT levels, up to 10%, between some of the pixels, which have bundled long, parallel coplanar wires connecting TES bolometers to inductor–capacitor filters. In this case, the high mutual inductances dominate. To mitigate this source of ECT, the coplanar wires should be replaced by microstrip wires in the array. Our study suggests that an FDM system can have a relatively low ECT level, e.g., around 0.4% if the frequency spacing is 30 kHz. Our results successfully demonstrate a low electrical crosstalk for a space FDM technology.

5.1. Introduction

Direct detection of the cosmic radiation that contains abundant information about the universe is an important way to address fundamental astronomical questions such as the history of the universe and the origins of galaxies, stars, and planets [1,2]. Cosmic radiation covers the full electromagnetic (EM) spectrum, ranging from the radio, the microwave, the sub-mm, and the far-infrared to gamma and X-rays. The Transition Edge Sensor (TES) is one of the most promising direct detectors because of its high sensitivity and its wideband response to EM radiation. TES based receiver instruments have been widely used for ground-based telescopes and are also candidates for future space telescopes. TES bolometers operating in the sub-mm and far-IR range approach the photon noise limit, in which the detection performance is limited by fluctuations in the arrival rate of photons at the detector instead of the intrinsic noise of the detectors. Consequently, increasing the number of detectors can enable higher mapping speeds, as well as covering a large field of view. Large TES arrays with thousands of pixels are needed for future ground and spaceborne telescopes [3–5]. A key challenge in realizing such large arrays has been multiplexing the signals between the detectors on the cold stage at the extremely low cryogenic temperature of ≤100 mK and the electronics at room temperature. Multiplexing limits the number of cold wires and, thus, minimizes the heat load on the cold stage, which is particularly vital for space telescopes, where the cooling power is limited by the available electrical power and the restrictions on the total mass.

Frequency division multiplexing (FDM) is one of the readout systems used for multi-pixel readout [6] of TES arrays. The other popular readout technology is time division multiplexing (TDM) [7,8]. In an FDM readout system, the detectors are in series with inductor–capacitor (LC) filters and are AC biased simultaneously, where the bias frequencies are the resonance frequencies of their corresponding LC filters [9]. The FDM system has several advantages, for example, there is no noise penalty with the increasing number of detectors per readout channel, the LC filters are passive elements with no power dissipation, and each detector bias can be adjusted independently so that all the detectors can be biased optimally, mitigating the effects of detector non-uniformity, e.g., the superconducting critical temperature (T_c) across the array.

FDM readout systems are being used in a number of instruments for ground-based telescopes for detecting cosmic microwave background (CMB) and sub-mm wavelength radiations, such as the Atacama pathfinder experiment Sunyaev-Zel'dovich (APEX-SZ) [10], the South Pole Telescope (SPT) [11] and the Polarization of Background Radiation (POLARBEAR) [12]. They are also being considered

for balloon-borne mission Large-Scale Polarization Explorer (LSPE) [13,14] and future spaceborne instruments such as Space Infrared telescope for Cosmology and Astrophysics/SpicA FAR infrared Instruments (SPICA/SAFARI) [15,16], Advanced Telescope for High ENergy Astrophysics/X-ray Integral Field Unit (ATHENA/XIFU) [17,18] and Lite satellite for the studies of B-mode polarization and Inflation from cosmic background Radiation Detection (Lite-Bird) [19]. Usually, fewer readout channels are available in spaceborne instruments than in ground-based ones. This means that the number of pixels per readout channel (i.e., multiplexing factor) is higher, which leads to a narrower frequency spacing between two neighboring resonators and makes it more difficult to keep the electrical crosstalk (ECT) level low.

The ECT is defined as the undesired signals that a detector receives from the electrical circuits instead of the signal from the sky or an optical source in the lab. A high ECT can induce errors in the detected signal, decrease the dynamic range, and even destabilize the detector to impede the multiplexing. It is, therefore, important to characterize and understand the ECT across an array using any new FDM readout system. However, few experimental studies are found in the literature. An ECT study on a TES array with an FDM readout system with carrier frequencies between 350 kHz and 850 kHz and a frequency spacing of 75 kHz has reported a maximum ECT level of 0.4%, where one TES was excited by LED light and responses of five dark pixels were measured [6]. If two systems have the same capacitance and same frequency spacing, the higher carrier frequency means a lower inductance, which can lead to a higher carrier leakage. A preliminary measurement was also reported that characterized the ECT by introducing X-ray pulses to TES micro-calorimeters, reading the other five pixels with a frequency spacing of at least 200 kHz [20]. The importance of the wiring to TES bolometers on the array chip has been simulated to relate high mutual inductance to the ECT in our lab [21], but no dedicated experiments on the effect of the wiring have been reported so far.

In this paper, we experimentally study the ECT in our FDM system that reads out 61 TES pixels with a nominal frequency separation of 32 kHz. We present a method to measure and map the ECT among all the pixels connected, identify the major sources of the ECT, and discuss ways to improve them.

5.2. FDM with Baseband Feedback

Fig 5.1 shows an electrical schematic diagram of the FDM readout with baseband feedback (BBFB) that we used for the ECT study. TES bolometers are connected in series with narrow bandpass cryogenic LC filters [22]. The room-temperature demultiplexer (DEMUX) electronics generates a comb of tones (i.e., carriers) with frequencies ranging from 1MHz to 4 MHz. Each of these tones is tuned to match the resonance frequency of one of the LC filters and provides an AC voltage bias to the corresponding TES. The LC filters also reject the wideband Johnson noise in the circuit. The TES currents are summed at the input coil of a superconducting quantum interference device (SQUID) amplifier. The signal at the output of the SQUID amplifier is essentially an amplitude-modulated version of the AC bias signal with a phase shift due to the electronics and wire harness. After further amplification by using a low noise amplifier (LNA) at room temperature, the output signal is demodulated to recover the bolometer electrical signals or optical signals if there is a sky source. These signals are then re-modulated using the same carrier tones with appropriate phase shifts and added to cancel out the SQUID output when applied to the feedback coil of the SQUID. This scheme is known as BBFB. A common shunt resistor (R_{shunt}) of 100 mΩ is used to provide a bias voltage for all the bolometers. The cryogenic electronics, including TES bolometers, LC filters, and SQUID, are at a temperature below the critical temperature (T_c) of a TES, typically at the base temperature of a cooler, while both the front-end electronics and DEMUX board are at room temperature.

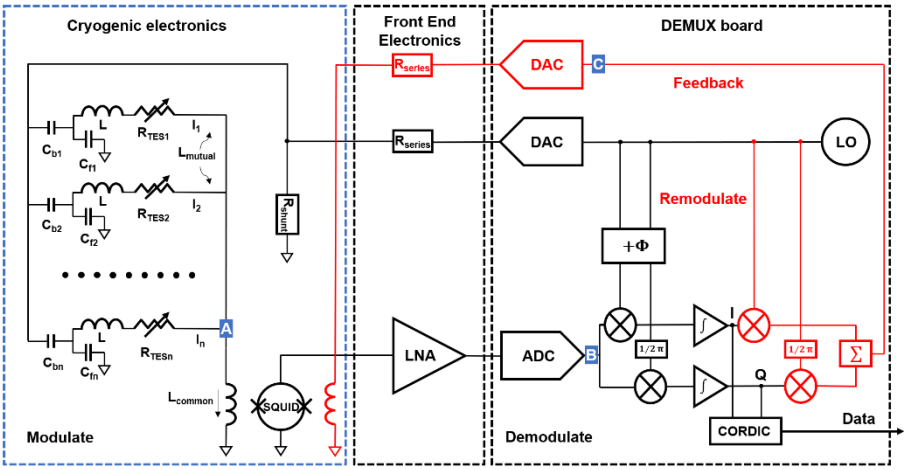

Fig. 5.1 FDM readout electrical schematic with baseband feedback (BBFB). The DAC provides AC bias voltages in the frequencies corresponding to the resonance frequencies of LC filters for the TES bolometers. The currents through TES bolometers are summed at the input coil of the SQUID amplifier, indicated by point A. The SQUID amplifies the amplitude-modulated signals at its output. After further amplification by the room-temperature LNA, the signal (at point B) is demodulated to I and Q information, then collected by using a CORDIC (COordinate Rotation DIgital Computer). In the feedback process, these signals are re-modulated and applied to the feedback coil (at point C) of the SQUID with appropriate phase shifts to cancel out the SQUID output.

All the measurements described in this paper are performed in an environment, intended to be dark, i.e., with no designed optical signals to the bolometers. However, there might be some influence of stray light that contributes to photon noise, which could increase the noise level in the measured noise spectrum. In this paper, the signals we use for the electrical crosstalk study are well above the detector noise, so the presence of stray light has negligible influence on our conclusions. The signals in the TES array are only electrical, AC bias tones from the DAC (digital-to-analog) device in an SRON home-made DEMUX board. All the signals are added in the summing point and then amplified by the SQUID. We demodulate the output signal to I and Q parameters to analyze and re-modulate them with a delayed carrier for

the BBFB [23]. We expect the ECT to happen mainly in the cold part of the FDM readout system. The ECT can be caused by a number of mechanisms [6], but here, we focus on the most important sources to introduce the ECT in an FDM system.

The ECT described in this paper can be attributed in general to a combination of carrier leakage, mutual inductance (L_{mutual}), and common inductance (L_{common}). Carrier leakage occurs when part of the current at the specific frequency that is intended for one detector leaks out to the other detectors because the LC filters are not perfect. Mutual inductance and common inductance are indicated in the cryogenic electronic part of Fig. 5.1. The mutual inductance is the magnetic coupling between two TES bias circuit branches [21], which can happen not only between the wires but also between the coils in the LC filters. The common inductance is the total sum of the inductance after the summing point, including the inductance of the input coil of the SQUID. The presence of common inductance makes the resonance frequencies of the circuit slightly different than those of the LC filters, which effectively means that the detectors are biased slightly off-resonance. Table 5.1 contains some of the main parameters of our FDM readout system.

Table 5.1 FDM system parameters

TES normal state resistance: 200 mΩ	SQUID input inductance: 1.5 nH
TES critical temperature:110 mK	Inductance of LC filters: 3 μH
TES Ti/Au bolometer size: 50 × 50 μm^2	Capacitance of LC filters: 1 nF–9 nF
TES Ta absorber size: 100 × 100 μm^2	Carrier frequency f_0: 1 MHz–4 MHz
TES Si_3N_4 legs volume: 400 × 2 × 0.25 μm^3	Frequency spacing Δf: 32 ± 3 kHz
Designed NEP level: 0.7 $aW/\sqrt{Hz}$	$\Delta f / f_0$: 0.08–0.32
SQUID mutual inductance: 27 $\mu A/\Phi_0$	Readout current noise: 20 $pA/\sqrt{Hz}$

5.3. Experimental Setup

Fig 5.2 shows the cold electronics part of our FDM setup, designed as a prototype of the SAFARI instrument on SPICA [24] It contains a 176-pixel TES array chip in between two LC chips with 88 resonators each and a SQUID amplifier as indicated. These are mounted inside a copper bracket, which is designed to be light-tight. It also holds a Helmholtz coil to eliminate the background magnetic field (not visible in Fig. 5.2). A Janis adiabatic demagnetization refrigerator (ADR) [25] is used to cool down the bracket. The lowest temperature it can reach is 50 mK, but with a relatively short operating duration. When it is operated at 90 mK, the ADR can run for more than 10 h, stabilized with a temperature variation of less than 0.01 mK. Thus, most of our measurements were performed at 90 mK.

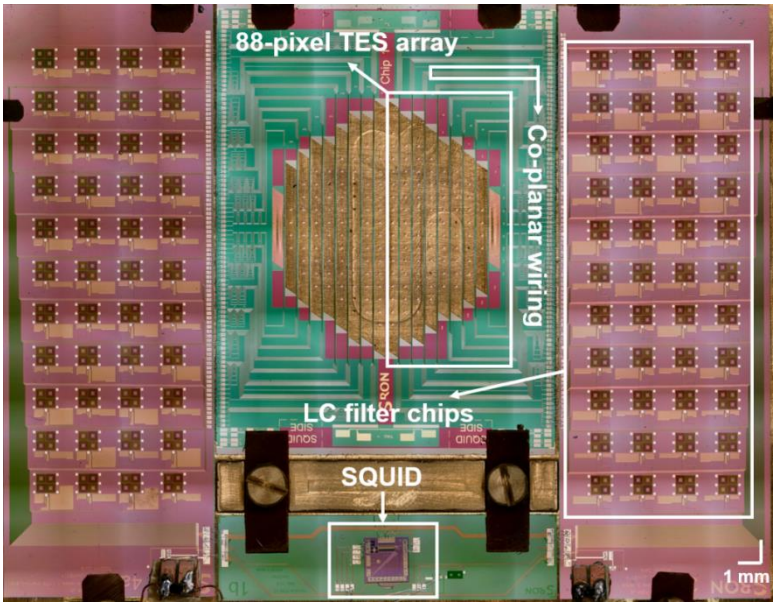

Fig. 5.2 Photo of the cold electronics part of the FDM readout system with the TES array chip in the middle, LC filter chips on the two sides, and the SQUID chip at the bottom. The array contains 176 pixels. The half array of 88 pixels, 84 bolometers, and four resistors is connected to simplify our measurement and analysis. The LC filters connect with the TES array via microstrip lines in

the LC filter chip, bonding wires, long coplanar wiring, and wires around TESs in the TES array chip. All the chips are mounted inside a light-tight copper bracket at 90 mK, which is not shown in the figure.

In the 176-pixel bolometer array, each bolometer has a Ti/Au TES with an area of 50×50 μm^2 and a 100×100 μm^2 thin Ta optical absorber. Both are defined on a Si_3N_4 membrane island, which connects with the Si substrate at the bath temperature through four long (400 μm), narrow (2 μm), and thin (0.25 μm) Si_3N_4 legs [24], which determine the thermal conductance between the TES and the thermal bath. The bolometers have a T_c of about 110 mK. The designed Noise Equivalent Power (NEP) of the TESs is

0.7 aW/$\sqrt{\text{Hz}}$. With a similar TES structure, we can provide an ultra-low NEP of 0.2 aW/$\sqrt{\text{Hz}}$ [26]. It is worth mentioning that eight of the pixels in the array are just simple resistors for calibration purposes.

The LC filters consist of low-loss dielectric capacitors and inductors and have a Q-factor of 10 000 or higher at 90 mK. The inductance of all the inductors is designed to be 3 μH, while the capacitance of the capacitors varies from 1 nF to 9 nF in order to adjust the frequency for each pixel, targeting an equal frequency spacing of 16 kHz. In reality, the total capacitance of an LC filter is a combination of the capacitance of a bias capacitor (e.g., C_b) and that of the capacitor in the filter (e.g., C_f), as illustrated in Fig. 5.1. The ratio between the filter and bias capacitances is 10 nominally, and each pair acts as a voltage divider in the bias circuit. The bias frequency ranges from 1MHz to 4MHz for the full array using two LC chips. To simplify the experiment, we choose to connect only half of the TES array to one LC filter chip (88 pixels connected) so that the frequency spacing is doubled (32 ± 3 kHz). Aluminum wire bonds

are used for connecting the chips in the mK stage.

The SQUID amplifier used is a single-stage SQUID developed at the National Metrology Institute in Germany (PTB), and the readout current noise of the SQUID-LNA chain is 20 pA/$\sqrt{\text{Hz}}$ [27,28].

Before starting a multiplexing readout measurement, we use a network analyzer (NWA) to measure the resonance frequencies of all the LC filters. Eventually, we selected 61 TES pixels that are connected to LC filters with a Q-factor higher than 10 000 for ECT measurements. Fine tuning of a resonance frequency is done by looking for a peak in the frequency scan when a TES is

operated in the superconducting state. Then, we fix the frequency and choose an appropriate phase delay for remodulation that allows us to close the BBFB loop stably. This process is called locking a pixel.

When all 61 TES pixels are simultaneously locked in their superconducting to normal transition, we take the current–voltage (IV) curve and the current noise spectrum of each pixel for a general health check of the FDM readout system and then start to characterize the ECT. Fig 5.3 (a) shows an enlarged picture of the wiring on the TES array chip and the LC filter chip, where the Nb coplanar wiring is defined on the TES array and is electrically connected to the LC filter chip by wire bonds. On the LC filter chip, the wiring is made of microstrip lines, which are the superconducting Nb wires, sandwiched with an SiO_2 insulating layer. To decrease the mutual inductance between the coils in the LC filters, the TES pixel neighbors in the frequency space are not the physical neighbors, as shown in Fig. 5.3 (c). Meander structures in the coplanar wires are introduced to compensate for different wiring lengths to fix the frequency spacing. Those long coplanar wires that are bundled in parallel and marked by the same color in Fig. 5.3 (b) cause potential ECT among the corresponding pixels due to the mutual inductance of the closely packed wire loops.

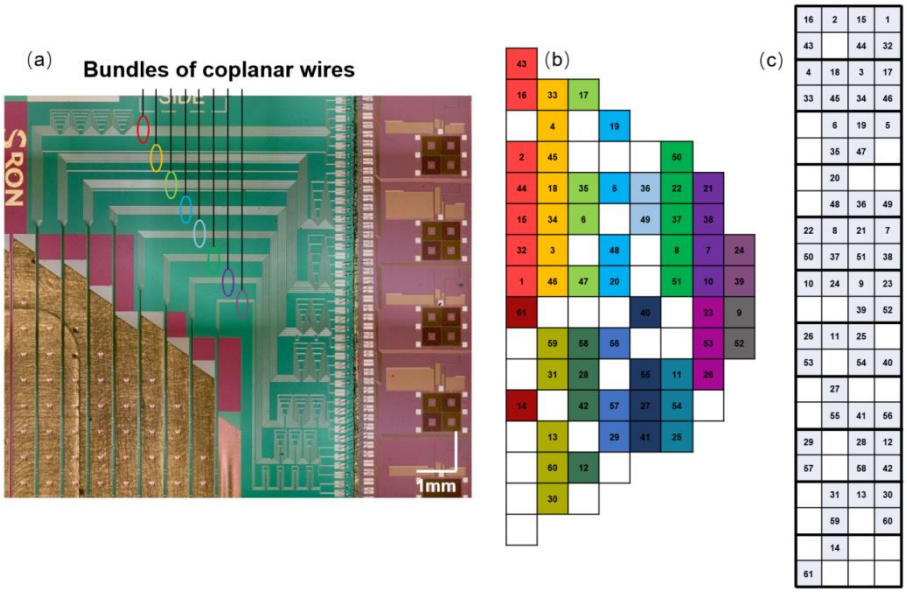

Fig. 5.3 (a) Zoomed photo of long, parallel coplanar wires in a number of bundles to connect TES bolometers to the bond pads. The coplanar wires are several centimeters long and have additional meander structures to adjust all the wires in the same bundle to have the same length. Different bundles of wires are circled in different colors. (b) Map of the connected pixels in the half array; pixels sharing the same bundle for the wiring are indicated by backgrounds of the same colors. (c) Map of the LC filters with the numbers corresponding to those of the pixels in the array in (b).

5.4. Forms of Electrical crosstalk

5.4.1. Carrier leakage

Due to carrier leakage, parts of the bias currents intended for other detectors leak into each detector. These are off-resonance bias currents with various frequencies that add up quadratically and can potentially destabilize the detector biasing when the total sum becomes comparable to the detector's own on-resonance bias current. The carrier leakage current ratio between the on-resonance pixel and a neighboring pixel approximately equals to $\left|\frac{R_{TES}^2}{(2\Delta\omega L)^2}\right|$, where $\Delta\omega = 2\pi\Delta f$, Δf is the frequency separation between two adjacent pixels, L is the inductance of the LC filters and equals 3 ± 0.1 μH, and R_{TES} is the resistance of the TES at its operating point [6]. Our bolometers are usually biased in the transition with the resistance at 30% of the normal state resistance R_n, which is 200 mΩ. The relative carrier leakage current is calculated to be 0.25% if the frequency separation is 32 kHz. This number increases to 1.0% if the frequency spacing decreases to 16 kHz, which is the case if the full array is connected. The carrier leakage comes not only from the neighboring pixels but also from the others in the array. To account for all the carrier leakage contributions, we need to consider all the off-resonance pixels by the following equations. The impedance of a TES and its connected LC filter as a unit in Fig 5.1 can be expressed as:

$$Z_n = \frac{1}{\frac{1}{j2\pi f_n L + R_{TESn}} + j2\pi f_n C_{fn}} + \frac{1}{j2\pi f_n C_{bn}}, \quad (5.1)$$

where f_n is the resonance frequency of the LC filter, and C_{fn} and C_{bn} are the capacitances of the capacitor in the LC filter and the bias capacitor, respectively. The leakage current amplitude through the TES and LC filter unit can be written as a unit voltage divided by the impedance Z_n:

$$Y_n = \frac{1}{Z_n}. \tag{5.2}$$

Then, the leakage current through the TES branch can be seen as the shunt of the total current through the TES and LC filter unit:

$$I_n = Y_n \cdot \frac{1}{\frac{1}{j2\pi f_n L + R_{TESn}} + j2\pi f_n C_{fn}} \cdot \frac{1}{j2\pi f_n L + R_{TESn}}. \tag{5.3}$$

Fig 5.4 (a) shows the calculated currents in 88 detectors using Equations (5.1)-(5.3) with the 32 kHz frequency spacing. The frequency span is chosen to be from 1MHz to 4 MHz, which is similar to our experiment. All the pixels are biased at 30% in their transition. The pixels are numbered sequentially in the frequency span, where pixel 1 is at the lowest frequency and pixel 88 at the highest. Pixel 44, which is in the middle of the frequency span, is chosen to illustrate the carrier leakage current in Fig. 4 because it has the highest number of neighbors on both sides. This leads to a higher carrier leakage than the pixels at the two ends of the frequency span as shown by Fig. 5.4 (c), where the neighbors from only one side contribute. Fig 5.4 (b) shows the calculated ECT of pixel 44 due to carrier leakage, contributed by all the other pixels. ECT from each pixel to pixel 44 in this case is calculated by quadratically dividing the leaking current of this particular pixel by the current of pixel 44 since the leaking current is off-resonance. The highest ECT, which is 0.25%, comes from the nearest neighbors. The total leaked current from all the other pixels to each pixel can be calculated by quadratically adding individual leaked currents; this is ≤0.8% of the total bias current, as shown in Fig. 5.4 (c). The ECT value due to carrier leakage will decrease with increasing frequency spacing and will increase with increasing bias voltage, causing the TES to operate higher in the transition. For example, the ECT level will become 0.69% when a detector is biased at 50% of the normal resistance.

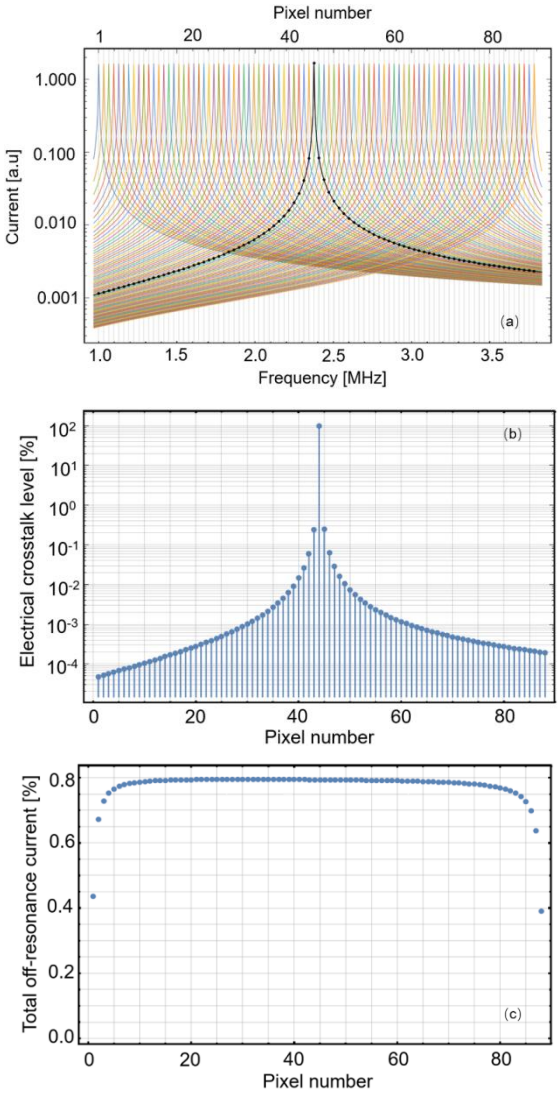

Fig. 5.4 (a) Simulated currents of 88 TES pixels, biased in the transition with 30% of the normal state resistance, are plotted in colors as a function of frequency. The black curve is the current of pixel 44 in the middle of the frequency span, which has a maximum carrier leakage from neighbors on both sides. (b) The calculated ECT due to carrier leakage from all the other pixels to pixel 44. (c) The ratio of the total off-resonance leakage current to the total bias current for each pixel expressed as a percentage. The first and the last

pixel are at the two ends of the frequency span and have the lowest crosstalk levels because they have neighbors on only one side in frequency space.

5.4.2. Mutual inductance

To bias and readout each bolometer in the array, two superconducting wires are required. They form a current loop through the TES, which consists of the wires connecting the TES through two Si_3N_4 legs, long coplanar wires to further connect bonding pads, bonding wires, and microstrip wires on the LC filter chip, as shown in Fig. 5.3 (a). Because of the mutual inductance between these loops, part of the bias current from one detector couples to the other detectors, causing crosstalk. The closer the loops, the higher the mutual inductance between them, while for the ones that are far apart, the coupling is negligible. The mutual inductance contributed by coplanar wiring in the array chip has been simulated previously [21], where the long coplanar wires that connect TES bolometers to LC filters can introduce a relatively high mutual inductance, which accounts for 59% of the total mutual inductance. It is important to note that in the simulation, the mutual inductance due to LC filters accounts for 31% of the total mutual inductance, but this value is significantly lower in our experiment. This is due to the fact that the LC filter chips have been redesigned here so that the resonators that are neighbors in resonance

frequency are not physical neighbors. The same simulation also shows that microstrip wires make a small contribution (1.4%) to the total mutual inductance. Therefore, the mutual inductance that comes from coplanar wires is expected to be the dominant factor in our case.

5.4.3. Common inductance

Due to common inductance, the resonance frequencies of the circuit, including TES, LC filter, and SQUID, are slightly different from the frequencies of the LC filter in series with the detectors. Large common inductance forces us to operate the detectors far off-resonance, which enhances the crosstalk level, so it is important to keep that as low as possible. The common inductance includes coupled inductance of SQUID feedback coil, inductance from wire bonds, and geometric inductance of the lines [6,29]. In our case, the common inductance is dominated by the input coupling inductance of the SQUID. The common inductance in our setup can be probed by a Network Analyzer (NWA)

scan through the feedback line [24]. As shown in Fig. 5.5, each LC filter appears as a peak and a valley in such a scan. It is known [24] that the frequencies corresponding to the peaks are determined by the sum of the inductance of the LC filters and the common inductance, while the valleys are the signature of the resonance frequencies of the LC filters only (f_0). The common inductance can then be derived from the following expression:

$$L_{com} = L[\left(\frac{f_0}{f_0 - \Delta f_0}\right)^2 - 1], \tag{5.4}$$

where L is the inductance, f_0 is the resonance frequency an LC filter ,and Δf_0 is the frequency difference between a peak and a valley. Looking closely at f_0=2236 kHz (Fig 5.5 inset), Δf_0 is 0.61 kHz, and with L=3 μH; using Equation (5.4) we find that our setup has a common inductance of only 1.64 nH. In the absence of any common inductance, the resonance frequencies are solely determined by the capacitances and the inductances (LC filters) that are in series with the TES detectors. However, in the presence of a common inductance, the same number of resonators are observed but all the resonance frequencies are slightly shifted. When $L_{com} \ll L$, the frequency shift can be written as $\Delta f_0 \approx 0.5 f_0 L_{com}/L$. When we operate at these resonance frequencies, we are slightly off-resonance in reference to what is defined by the LC filters. This translates to an additional impedance (Z_{com}) in series with the detectors in the same

branch circuit, which is $Z_{com} = 4\pi\Delta f_0 L$, and substituting the Δf_0 value mentioned above, it can also be written as $Z_{com} = 2\pi f_0 L_{com}$. If this impedance becomes comparable to the TES resistance at the operating point, it will affect the level of crosstalk by increasing the carrier leakage as illustrated by the formula $\left|\frac{R_{TES}^2 + Z_{com}^2}{(2\Delta\omega L)^2}\right|$. The Z_{com} provides a negligible increase in carrier leakage in the low-frequency range due to the low value of Zcom. This impedance will become large (about 40 mΩ) at the high end of our bias frequency range. When we bias the high-frequency detectors at 50% transition (about 100 mΩ),

the ECT level will increase from 0.69% to 0.79% due to this common impedance. Therefore, even in the highest bias frequency, the influence of common inductance is very small. In addition, the common inductance will indirectly affect the ECT through the off-resonance and frequency separation argument. The off-resonance due to common inductance in our highest

frequency of 3900 kHz is only 1.07 kHz, which means that this largest frequency shift gives 3.3% shift in frequency with respect to the 32 kHz separation in our case. In summary, the 1.64 nH common inductance will give a negligible influence on the ECT in the operating frequency range of 1 MHz-4 MHz.

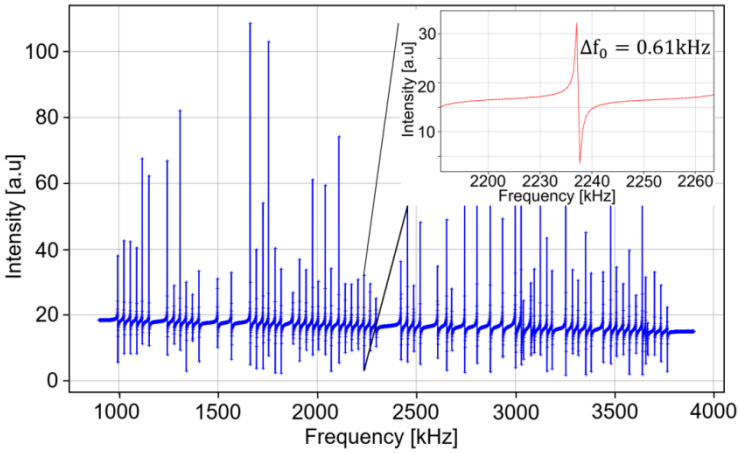

Fig. 5.5 Network analyzer scan through the feedback line. The inset focuses on the resonance of pixel 29 at f_0 = 2236 kHz, where the frequency difference Δf_0 between the peak and the valley is 0.61 kHz, which corresponds to a common inductance of 1.64 nH.

5.5. Experimental results and discussions

5.5.1. Three-pixel measurement

Our technique for characterizing the ECT is as follows: We choose three bolometers first, pixel 24 in the middle and its two adjacent pixels 23 and 25. First, we bias all three detectors at their usual operating point, 50% in the transition. In our FDM system, it is possible to set a low-frequency amplitude modulation of different kinds on a fraction of the full amplitude of the AC bias signal. This is a powerful tool that can be used for triggering or other diagnostic purposes such as measuring the complex impedance of the

detectors [30]. We use this to excite pixel 24 by sine-wave modulating 1% of its bias voltage at a frequency of 120 Hz injected next to the carrier. We choose 1% because it gives us a sufficiently large signal, well above the noise level but at the same time creates no obvious harmonics that disturb the noise spectra. There is nothing special about the 120 Hz other than being well within the detector response speed and away from the power line frequency of 50 Hz and its harmonics. Since this modulation frequency is much lower than the AC bias frequency (i.e., 1 MHz–4 MHz), the measured ECT is independent of the exact modulation frequency, and any frequency within the detector band serves our purpose. We now record the current noise spectra of these pixels simultaneously. In the absence of the ECT, only the excited pixel is expected to have a peak at 120 Hz in its noise spectrum. If peaks at 120 Hz also appear in the noise spectra of other pixels, it means that part of the modulated bias of the excited pixel also biases other pixels, and the ratio of peaks can be used as a measure of the crosstalk. Fig 5.6 (a) shows the demodulated noise spectra of these three pixels in a frequency span from 1 kHz to 100 kHz, where we will focus on the peaks at 120 Hz. We define the peak at 120 Hz in the spectrum of pixel 24 as the excited peak and in the spectrum of pixel 23 or 25 as the responding peak. The ratio of a responding peak to the excited peak is attributed to the level of ECT between two pixels. Fig 5.6 (b) shows the normalized peaks on a logarithmic scale, where the ECT for pixels 23 and 25 is measured as 0.7% and 1.0%, respectively. The ECT level can be well explained by the carrier leakage simulation, which gives a 0.69% ECT level with detectors biased at 50% in the transition. The higher ECT between pixel 24 and pixel 25 is expected since the frequency space between these two pixels is 30 kHz and slightly less than the frequency spacing between pixel 23 and 24, which is 35 kHz.

Furthermore, the operating point of the TES can also influence the ECT, because the crosstalk due to carrier leakage decreases as the operating point goes lower in transition. First, our TES bolometers are typically operated in a range of 30%-50% of the resistance transition. When we start with the three-pixel experiment, we bias them at 50% transition. Because of the higher resistance at this bias point, a higher ECT due to carrier leakage is expected. Then, for the measurement with the entire array, ideally we want to bias all our detectors at the 30% transition but we were not able to do so due to the fact that the detectors' response speed was too fast at this bias point and caused oscillations. To avoid this, some of the pixels were biased at 50% transition or higher.

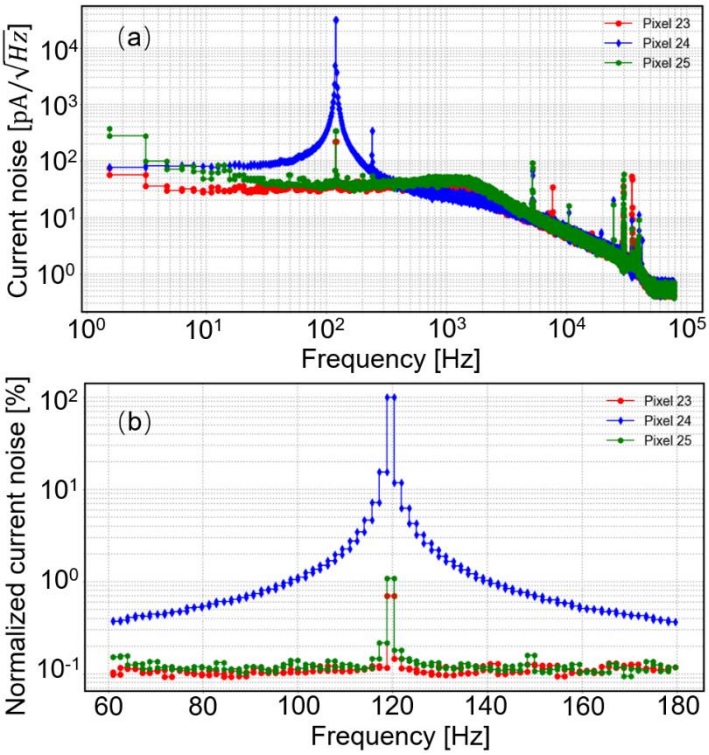

Fig. 5.6 (a) Current noise spectra of three neighboring pixels, where pixel 24 is excited by 1% modulation at 120 Hz on its AC (MHz) bias voltage. The spectra are recorded simultaneously using the FDM readout. The line at 240 Hz in pixel 24 is a harmonic of the modulation. Some lines beyond 5 kHz are the noise lines due to DEMUX and FEE electronics. (b) The current noise spectra of the three pixels around 120 Hz normalized to the peak at 120 Hz in pixel 24.

5.5.2. 61-pixel TES array measurement

Now, we extend the method to map the ECT across the TES array. Once all the pixels are biased in the transition and are locked, the FDM system can measure the current noise spectra of all connected pixels in the array simultaneously. Then, we apply the same method as that for the three-pixel

measurement to the whole array, going from the first pixel to the last. For each excited pixel, we record

the ECT levels in the other 60 pixels and form a 1×61 array, shown as one row in Fig. 5.7. We assign a value of 100% for the excited pixel itself that is marked in black in that row. In this way, we can summarize the ECT level for all 61 pixels to generate the 61×61 matrix, as shown in Fig. 5.7. Pixel 1 corresponds to the lowest frequency of 1 MHz, while pixel 61 corresponds to the highest frequency of 3.9 MHz in this case. The noise level around 120 Hz, which we call the background noise, can influence the accuracy of the measurement, especially for those pixels that are far away from the excited pixel in frequency and show a weak response. Therefore, before calculating the ratio of the peaks, we quadratically subtract the background noise from all the peaks.

We repeat this process by exciting each pixel one by one and reading out the noise of the entire array to map out the ECT as shown in Fig. 5.7. In each row, the excited pixel number is the same as the row number and marked in black. The levels of the ECT observed in other pixels when this one is excited are illustrated by colors in that row. Similarly, in each column, the responding pixel number is the same as the column number and marked in black. The levels of the ECT observed in this pixel when others are excited are illustrated by colors in that column. About 94% of the squares in the 61×61 ECT matrix are blue, meaning that they are below the 0.4% level, suggesting that some of them approach zero. The pixels that are far away from the excited pixel in the frequency space are expected to show a negligibly low crosstalk level if the carrier leakage is the dominant mechanism. Those pixels adjacent, for example, to pixel 8 in the matrix have an ECT level around 0.4%. This value can be explained by the overall carrier leakage level in our setup with a nominal frequency spacing of 32 kHz and with TES bolometers biased at 30%–50% in the transition region.

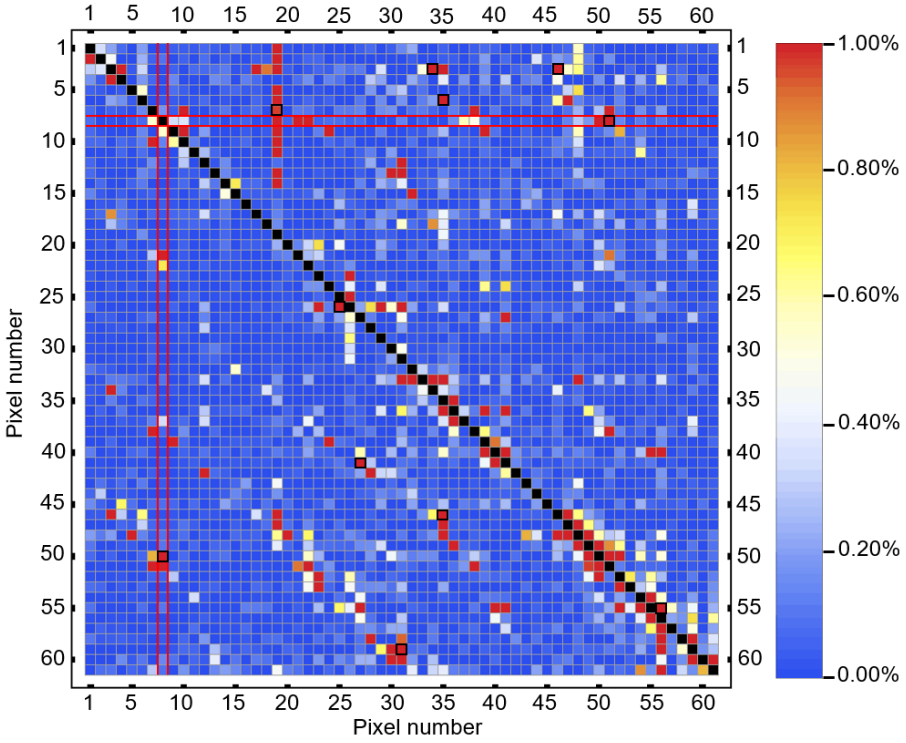

Fig. 5.7 Electrical crosstalk level of 61 pixels out of a TES array readout simultaneously in a multiplexing mode by using an FDM system. In this 61×61 matrix, each row presents the crosstalk level of the pixels, caused by one of the pixel with black color. The number represents the pixel from 1 to 61, which follows the order of the biasing voltage frequency from 1 MHz to 4 MHz. The level of the crosstalk is indicated by color, quantified by the color bar in the figure, where we plot the level only up to 1% for clarity. If the level is above 1%, the color will be the same as that for 1%. We add a black boundary "□" to the filled red square "■" for the points with the ECT higher than 10%. The column presents the crosstalk level of the pixels, which contribute the crosstalk to the pixel in black. Row 8 and column 8 are marked to stress the comparison in their level distributions.

A number of high-frequency biased pixels, or the high pixel numbers from 46 to 61, show high ECT levels of 0.4%-1% to their adjacent pixels. We refer to the right bottom corner of the matrix in Fig. 5.7. This is partly because the crosstalk due to the mutual inductance increases with the resonance

frequency. Another reason is that the higher the frequency, the larger the frequency shift due to the common inductance, leading to a higher carrier leakage. This can be seen by rewriting Equation (5.4) as:

$$\Delta f_0 = \frac{f_0\left(\sqrt{\frac{L_{com}}{L}+1}-1\right)}{\sqrt{\frac{L_{com}}{L}+1}}. \tag{5.5}$$

Since the common inductance is constant, the frequency shift is proportional to the resonance frequency. Therefore, the bolometers with higher bias frequencies, e.g., 3 MHz, will have a larger shift of resonance frequency than those with lower bias frequencies of 1 MHz. In column 19, the high ECT levels that appear between row 1 and 14 are due to pixel 19 that was not biased stably when pixel 1-14 were excited.

In Fig. 5.8, we focus on pixel 8 and take a closer look at the data in the eighth row and column of the crosstalk map. We see that although there are similarities between Figs. 5.8 (a) and 5.8 (b), they are not exactly the same. This means that the ECT caused by pixel 8 to the rest of the array is different from that caused by the rest of the array to pixel 8. This is expected in our system because of the nonuniformity of the TES array and the fact that not all the pixels are biased at the exact same point in the transition. Thus, the bolometers have a different responsivity, and therefore, the ECT map is nonsymmetric.

In addition, the crosstalk due to mutual inductance is proportional to the resonance frequency, which means that the crosstalk from a high-frequency pixel to a low-frequency pixel is higher than the other way around. In other words, even if all the bolometers were the same and also operated under the same bias condition, we would not have expected a symmetric ECT map. It is interesting to note that, although some of the pixels have a large frequency separation from the excited one, they show a high level of ECT of 1% or more and together form approximately diagonal patterns across the crosstalk map, visible in Fig. 5.7. For example, there are high levels of ECT between pixels 8, 21, 22, 50, and 51.

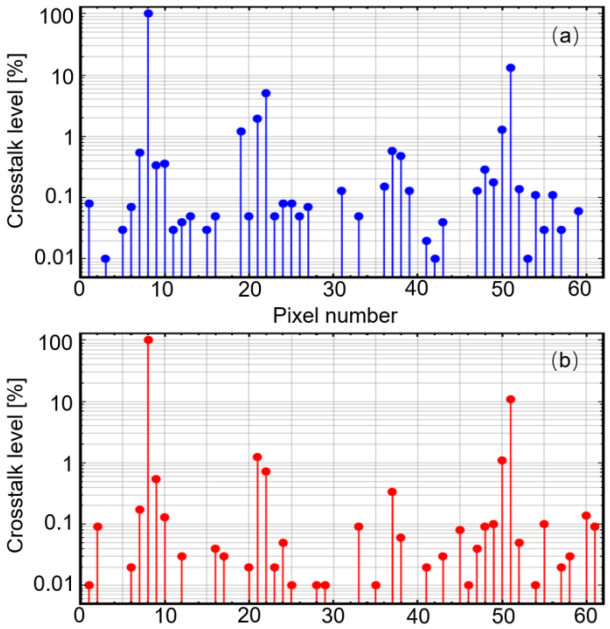

Fig. 5.8 (a) Measured crosstalk level of 61 pixels except for pixel 8, which is used as the excitation. The dataset is the same as row 8 in Fig. 5.7, but is now plotted numerically. (b) Crosstalk level of 61 pixels from column 8 in Fig. 5.7.

The high ECT level is most likely due to the high mutual inductance in the coplanar wires that connect bolometers to LC filters. In our setup, pixels 8, 21, 22, 50, and 51, which appear to have a high level of ECT, make use of long, parallel coplanar wires, which are closely packed in a bundle as circled in Fig. 5.3 (a) and grouped in the same color in Fig. 5.3 (b). To prove this hypothesis, we assume a high ECT level among the bolometers that use the long coplanar wires in a common bundle, but no difference in the amplitude. These pixels are marked in black in a new 61×61 matrix in Fig. 5.9 (a). As we can see, these pixels form approximately parallel, diagonal patterns in the matrix. To have a comparison with the measurement, we now over plot Figs. 5.7 and 5.9 (a), resulting in Fig. 5.9 (b). We find that the parallel, diagonal-lined distribution matches reasonably well with the measured high ECT pixels distributed along or in the vicinity of the simulated diagonal lines, although the pixels from the measurement are slightly scattered. Therefore, we believe that we have confirmed that those pixels observed with a high ECT level in Fig. 5.7 are due to higher mutual inductances contributed by the bundled long, coplanar wires.

One could simulate the effect of the mutual inductances in detail by considering the width, length, and distribution of all the coplanar wires to quantify the magnitude of the ECT in order to compare with the measurement. However, this is beyond the scope of this paper. The high ECT for the pixels with long coplanar wires in a bundle is expected from the earlier simulation [21]. However, this is the first time experimental confirmation of this effect. To reduce this particular form of the ECT, one should introduce wires with low mutual inductances. Microstrip wires seem to be the best choice, as they are used in the LC filter chips. Furthermore, the microstrip wiring allows dense packing of many wires, making connections for more pixels feasible for a given array size. A microstrip wire is a "sandwich" structure: a superconductor on the top, a dielectric layer in the middle, and another superconductor on the bottom, while coplanar wires mean parallel superconducting wires on the top of a substrate.

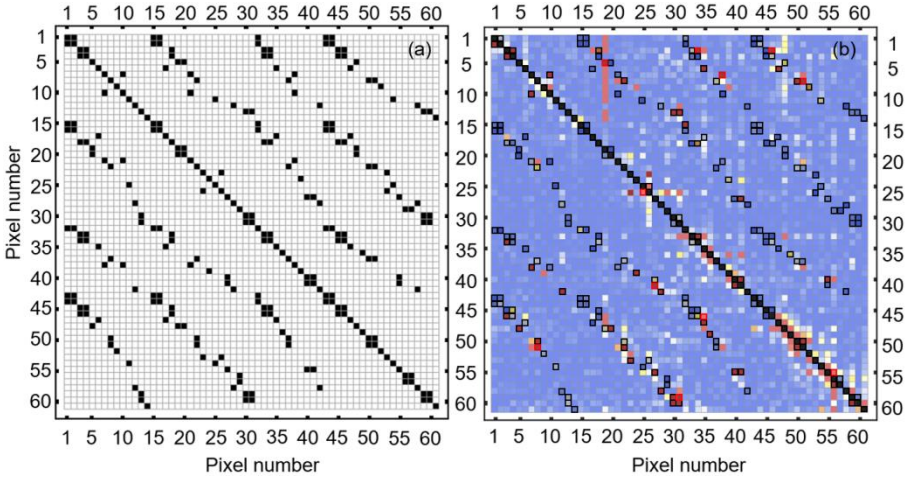

Fig. 5.9 (a) Pixels (represented by filled squares in black) connected with long, coplanar wires in a bundle, assumed to have a high crosstalk due to mutual inductance, are shown on a 61×61 matrix; their distribution is characterized by a number of parallel, diagonal lines. (b) The pixels with the high crosstalk in (a) are now represented by empty squares with a black boundary "□" and are superimposed with 50% transparency to the measured crosstalk matrix from Fig. 7, where the measurement data also show the parallel, diagonal line

distribution as in (a). For clarity, those pixels with the ECT level above 10% are illustrated by empty squares with a red boundary "□."

Our study is also a part of the experimental demonstration of an FDM prototype for the SAFARI instrument on SPICA. Through reading out half of the array, we have established the following understanding. First, the common inductance has a negligible effect on the ECT; second, carrier leakage can cause the ECT, which depends strongly on the inter-pixel frequency spacing. In our experiment, we have shown that only adjacent pixels have a strong effect, which can cause the ECT to be 0.4%, but the remaining pixels have a negligibly low level of the ECT. The 0.4% ECT is slightly higher than the theoretical value (0.25%) due to the fact that many pixels are biased in higher than 30% of the normal resistance at the transition or have the frequency spacing smaller than 32 kHz. Although no measurement has yet been performed, with the full array connected, due to the reduction of the inter-pixel frequency spacing by a factor of 2, we expect the ECT of neighbors to reach 1.0% and the total off-resonance bias current level to be 3.2%. The total off-resonance bias current is the quadratic summation of all off-resonance bias currents due to carrier leakage calculated using Equation (5.3), as shown in Fig. 5.4 (c). Finally, the higher mutual inductances contributed by long coplanar wires closely packed in a group can introduce a severe ECT. Therefore, the overall ECT level is dominated by the high ECT caused by mutual inductance. However, this can be mitigated by using microstrip wiring in a TES array. Furthermore, the length of the wires will become significantly shorter in practice, which also helps reduce the mutual inductance.

The latest design of the SAFARI instrument (SAFARI 4.2) requires a multiplexing factor of 120 with the same frequency span of 1 MHz–4 MHz, implying a frequency spacing of 25 kHz between pixels. Based on our current study, we expect the leakage current to dominate the ECT so that the level of the ECT of nearest neighbors is only 0.45%, while the total off-resonance bias current level will be around 1.3%. This is relatively small and is considered acceptable for the instrument.

5.6. Conclusions and Outlook

We have developed a new method to characterize and map the ECT of an FDM system with a TES bolometer array, which is a SAFARI FDM readout prototype. By introducing a small modulation at 120 Hz in the AC bias voltage to one pixel, and measuring the response in the noise spectra of other pixels, we have for the first time mapped the ECT level of 61 pixels in an array, with a nominal frequency spacing of 32 kHz in a 61×61 matrix. We have found that about 94% of pixels show an ECT level of less than 0.4%. Among them, only the adjacent pixels reach that level, while the ECT level of the remaining pixels is less than 0.1%. For cases with ECT levels below 0.4%, the carrier leakage dominates the ECT. We also observe a higher ECT level, up to 10%, from the pixels that have bundled long, parallel coplanar wires. Those pixels contribute to the ECT in the 61 × 61 matrix with a unique distribution characterized by a number of parallel, diagonal lines, which match reasonably well with the hypothesis of the high mutual inductance. To mitigate the ECT due to high mutual inductances, the coplanar wires should be replaced by microstrip wires. Our study suggests that our FDM can have a relatively low ECT level, e.g., around 0.4% if the frequency spacing is about 30 kHz. Since the base line for the SAFARI instrument is to have a frequency spacing of 25 kHz-30 kHz in the FDM readout and microstrip wiring on the detector arrays, our results promise low ECT levels in the eventual system.

In practice, all detectors are exposed to light and their carriers are modulated at the same time. We argue that our experiment reflects the right levels of electrical crosstalk in practice when the detectors are exposed to very weak optical signals, which were the prime science case for SAFARI/SPICA. Since the excited modulation signals in our case are very small, we are certainly within the small signal regime and the system operates linearly. This was confirmed by applying 1%, 5%, and 10% modulation excitation and seeing that the measured ECT levels scaled with the level of excitation. This means in first order that, if multiple pixels are excited at the same time, the total crosstalk signal on the other pixels will be the linear sum of the crosstalk signals of those excited pixels, when excited one by one. We were not able to confirm this experimentally, since our firmware only allows for modulation of one carrier at a time but this is something that can be implemented in the future.

The study of the crosstalk and non-linear effects under relatively high optical load that brings the detectors to near saturation is vital and has a major impact on calibration philosophy of the instrument. We recognize that a thorough crosstalk analysis needs to address such conditions, too, but this is beyond the scope of this manuscript.

To fully characterize the crosstalk of a TES array–FDM system, one should also include an optical crosstalk. In the case of the SAFARI instrument, the leak of an optical signal from one feedhorn to others in the array can cause an optical crosstalk. Unlike the ECT, the optical crosstalk occurs mainly in physical neighbors. To measure the optical crosstalk, our setup needs to be upgraded by adding a feedhorn array in combination with an optical source, which is considered to be the next step toward a full demonstration of the SAFARI prototype.

References

[1] D. Farrah, K. E. Smith, D. Ardila, C. M. Bradford, M. Dipirro, C. Ferkinhoff, et al., "Review: Far-infrared instrumentation and technological development for the next decade," J. Astron. Telesc., Instrum. Syst. **5,** 1 (2019).

[2] K. W. Christopher, "Terahertz Astronomy", CRC Press, Boca Raton (2016).

[3] K. D. Irwin and G.Hilton, "Transition-edge sensors", Springer Berlin Heidelberg. 63 (2005).

[4] Y. Zhao, "Characterization of Transition Edge Sensors for the Millimeter Bolometer Array Camera on the Atacama Cosmology Telescope", Ph.D. thesis, Princeton University (2010).

[5] D. Rigopoulou, F. Helmich, L. Hunt, J. Goicoechea, P. Hartogh, D. Fedele, et al., "The European far-infrared space roadmap", arXiv:1701.00366 [astro-ph.IM] (2017).

[6] M. A. Dobbs, M. Lueker, K. A. Aird, A. N. Bender, B. A. Benson, L. E. Bleem, et al., "Frequency multiplexed superconducting quantum interference device readout of large bolometer arrays for cosmic microwave background measurements", Rev. Sci. Instrum. **83,** 073113 (2012).

[7] W. B. Doriese, J. A. Beall, S. Deiker, W. D. Duncan, L. Ferreira, G. C. Hilton, et al., "Time division multiplexing of high-resolution x-ray microcalorimeters: Four pixels and beyond", Appl. Phys. Lett. **85,** 4762-4764 (2004).

[8] D. Prêle, F. Voisin, M. Piat, T. Decourcelle, C. Perbost, C. Chapron, et al., "A 128 multiplexing factor time-domain SQUID multiplexer", J. Low Temp. Phys. **184,** 363-368 (2016).

[9] B. D. Jackson, P. A. J. de Korte, J. van der Kuur, P. D. Mauskopf, J. Beyer, M. P. Bruijn, et al., "The SPICA-SAFARI detector system: TES detector arrays with frequency division multiplexed SQUID readout", IEEE Trans. Terahertz Sci. Technol. **2,** 12-21 (2012).

[10] D. Schwan, P. A. R. Ade, K. Basu, A. N. Bender, F. Bertoldi, H.-M. Cho, et al., "Invited Article: Millimeter-wave bolometer array receiver for the Atacama pathfinder experiment Sunyaev-Zel'dovich (APEX-SZ) instrument", Rev. Sci. Instrum. **82,** 091301 (2011).

[11] J. S. Avva, P. A. R. Ade, Z. Ahmed, A. J. Anderson, K. Aylor, R. Basu Thakur et al., "Particle physics with the cosmic microwave background with SPT-3G," arXiv:1911.08047 [astro-ph.CO] (2019).

[12] H. Logan, "The POLARBEAR-2 Cryogenic Receiver for Cosmic Microwave Background Polarization Science", Ph.D. thesis, University of California, San Diego (2019).

[13] G. Signorelli, A. M. Baldini, C. Bemporad, M. Biasotti, F. Cei, V. Ceriale, et al., "A 16 channel frequency domain-modulation readout system with custom superconducting LC filters for the SWIPE instrument of the balloon-borne LSPE experiment," Nucl. Instrum. Methods Phys. Res., Sect. A **824,** 184-186 (2016).

[14] A. Tartari, A. M. Baldini, F. Cei, L. Galli, M. Grassi, D. Nicolò, et al., "Development and testing of the FDM read-out of the TES arrays aboard the LSPE/SWIPE balloon-borne experiment", J. Low Temp. Phys. **199,** 212-218 (2020).

[15] P. R. Roelfsema, H. Shibai, L. Armus, D. Arrazola, M. Audard, M. D. Audley, et al., "Spica-a large cryogenic infrared space telescope: Unveiling the obscured universe", Publ. Astron. Soc. Aust. **35,** E030 (2018).

[16] G. de Lange, P. Roelfsema, M. Giard, F. Najarro, K. Wafelbakker, W. Jellema, et al., "The SAFARI Grating Spectrometer for the SPICA Space Observatory", Proc SPIE. **107081N** (2018).

[17] D. Barret, J. W. den Herder, L. Piro, L. Ravera, R. Den Hartog, C. Macculi, et al., "The hot and energetic Universe: The X-ray integral field unit (X-IFU) for Athena+", arXiv:1308.6784 [astro-ph.IM] (2013).

[18] L. Gottardi, H. Akamatsu, D. Barret, M. P. Bruijn, R. H. den Hartog, J. den Herder, et al., "Development of TES-based detectors array for the X-ray Integral Field Unit (X-IFU) on the future x-ray observatory ATHENA", Proc SPIE. **91442M** (2014).

[19] G. C. Jaehnig, K. Arnold, J. Austermann, D. Becker, S. Duff, N. W. Halverson, et al., "Development of space-optimized TES bolometer arrays for LiteBIRD", J. Low Temp. Phys. **199,** 646 (2020).

[20] R. den Hartog, C. Kirsch, C. de Vries, H. Akamatsu, T. Dauser, P. Peille, et al., "Crosstalk in an FDM laboratory setup and the athena X-IFU end-to-end simulator", J. Low Temp. Phys. **193,** 533-538 (2018).

[21] X. Yan, M. P. Bruijn, H. J. van Weers, R. A. Hijmering, J. van der Kuur, and J. R. Gao, "Modeling inductances of wiring for a TES array read by FDM", IEEE Trans. Appl. Supercond. **25,** 1-5 (2015).

[22] M. P. Bruijn, L. Gottardi, R. H. Hartog, J. van der Kuur, A. J. van der Linden, and B. D. Jackson, "Tailoring the high-Q LC filter arrays for readout of kilo-pixel TES arrays in the SPICA-SAFARI instrument", J. Low Temp. Phys. **176,** 421-425 (2014).

[23] K. Sakai, Y. Takei, R. Yamamoto, N. Y. Yamasaki, K. Mitsuda, M. Hidaka, et al., "Baseband feedback frequency-division multiplexing with low-power dc-SQUIDs and digital electronics for TES X-ray microcalorimeters", J. Low Temp. Phys. **176,** 400-407 (2014).

[24] R. A. Hijmering, R. den Hartog, M. L. Ridder, A. J. van der Linden, J. van der Kuur, J. R. Gao, et al., "Readout of a 176 Pixel FDM System for SAFARI TES Arrays", Proc SPIE. **99141C** (2016). note we used the same TES array as described in this paper, but the correct thickness of Si_3N_4 should be 0.25 μm.

[25] Janis Products, https://www.janis.com/products/janis-products, 2020.

[26] T. Suzuki, P. Khosropanah, M. L. Ridder, R. A. Hijmering, J. R. Gao, H. Akamatsu, et al., "Development of ultra-low-noise TES bolometer arrays", J. Low Temp. Phys. **184,** 52–59 (2016).

[27] M. D. Audley, Q. Wang, R. A. Hijmering, P. Khosropanah, G. de Lange, A. J. van der Linden, et al., "SQUID noise in a 176-pixel FDM demonstrator for the SAFARI far-infrared spectrometer," J. Low Temp. Phys. **199,** 723-729 (2020).

[28] Q. Wang, M. D. Audley, P. Khosropanah, J. van der Kuur, G. de Lange, A. Aminaei, et al., "Noise measurements of a low-noise amplifier in the FDM readout system for SAFARI", J. Low Temp. Phys. **199,** 817-823 (2020).

[29] J. van der Kuur, P. A. J. de Korte, P. de Groene, N. H. R. Baars, M. P. Lubbers, and M. Kiviranta, "Implementation of frequency domain multiplexing in imaging arrays of microcalorimeters", Nucl. Instrum. Methods Phys. Res., Sect. A **520,** 551-554 (2004).

[30] E. Taralli, P. Khosropanah, L. Gottardi, K. Nagayoshi, M. L. Ridder, M. P. Bruijn, et al., "Complex impedance of TESs under AC bias using FDM readout system", AIP Adv. **9,** 045324 (2019).

Chapter 6

Frequency division multiplexing readout of 60 low-noise transition-edge sensor bolometers

Based on

Q. Wang, P. Khosropanah, J. van der Kuur, G. de Lange, M. D. Audley, A. Aminaei, M. L. Ridder , A.J. van der Linden, M. P. Bruijn, F. van der Tak, and J.R. Gao, Appl. Phys. Lett. 119, 182602 (2021).

We demonstrate multiplexing readout of 60 transition edge sensor (TES) bolometers operating at 90 mK using a Frequency Division Multiplexing readout chain with bias frequencies ranging from 1 to 3.5 MHz and with a typical frequency spacing of 32 kHz. The readout chain starts with a two-stage SQUID amplifier and has a noise level of 9.5 pA/$\sqrt{\text{Hz}}$. We compare the current-voltage curves and noise spectra of the TESs measured in single-pixel mode and in multiplexing mode. We also map the noise equivalent power (NEP) and the saturation power of the bolometers in both modes, where there are 43 pixels that show not more than 10% difference in NEP and 5% in saturation power when measured in single pixel and multiplex mode. We have succeeded in reading out a TES with an NEP of 0.45 aW/$\sqrt{\text{Hz}}$ in the multiplexing-mode, which demonstrates the capability of reading out ultra-low noise TES bolometer arrays for space applications.

6.1. Introduction

Frequency division multiplexing (FDM) is one of the most promising techniques for the read-out of transition edge sensor (TES) bolometers arrays [1-3]. The FDM readout technique has the advantage of being able to bias each TES in the array individually for optimum settings and shows a competitive performance [4] compared to other promising readout techniques such as the time division multiplexing (TDM) [5] and the microwave superconducting quantum interference device (SQUID) readout [6,7]. FDM techniques are currently being developed for ground-based observatories [8,9], balloon-borne observatories [10,11] and considered for space observatories, such as Lite satellite for the studies of B-mode polarization and Inflation from cosmic background Radiation Detection (LiteBIRD) [12] and the far-infrared spectrometer (SAFARI) proposed for the recently cancelled Space Infrared Telescope for Cosmology and Astrophysics (SPICA) [13,14]. The spacecraft platforms usually have limited resources of power, mass and volume [4,13] which could restrict the use of ground based FDM technology. The requirements of SAFARI, for example, not only impose a different configuration of the FDM readout chain than that of the ground-based system, but also demand different LC (inductor-capacitor) filter designs, e.g., small frequency spacing and a compact chip design [15].

An FDM system suitable for space platforms has three key requirements: (a) it requires a higher multiplexing factor, i.e. a narrow frequency spacing between two adjacent pixels, determined by the array of LC filters [16], and a small number of readout chains. The latter decreases the dissipation power from the SQUID amplifiers and the readout electronics, and also the complexity of the system [16] ; (b) the noise level of the readout must be lower than that of the TES detectors, implying noise current spectral density ($A/\sqrt{Hz}$) $S_{I,read} < \sqrt{S^2_{I,ph} + S^2_{I,Jo}}$, where $S_{I,read}$ is the current noise level in the SQUID input, while $S_{I,ph}$ and $S_{I,Jo}$ are the phonon noise and Johnson noise of the detectors, respectively [3]; (c) the crosstalk between detectors should be sufficiently low [17], i.e., the measured characteristics of a TES, which are read out in a multiplexing mode (MM), namely measuring several bolometers simultaneously, should be the same as when read out in a single-pixel mode (SPM). The SPM is well calibrated and has no crosstalk issue.

The required noise equivalent power (NEP) of TES bolometers for SAFARI is 0.2 $aW/\sqrt{Hz}$. The challenge of a low NEP readout system is to satisfy the

requirements on crosstalk while adding minimal noise. Bolometers with the required NEP have already been realized: a single pixel TES was reported with an NEP as low as 0.1 aW/$\sqrt{\text{Hz}}$ [18]. The state of the art of the FDM technology is reported in reference [9], where 206 pixels were successfully read out with six SQUID amplifiers with an NEP of ~30 aW/$\sqrt{\text{Hz}}$. Another work that reported 176-pixel FDM readout system suffered from high readout noise and crosstalk [19]. Until now, a low readout noise FDM system suitable for readout of multiple pixels with a low NEP (≤ 0.2 aW/$\sqrt{\text{Hz}}$) has not been demonstrated.

In this letter, we report simultaneous readout of 60 low NEP TES bolometers using an FDM readout demonstrator, with a nominal frequency spacing of 32 kHz and a low readout noise level of 9.5 pA/$\sqrt{\text{Hz}}$. The TES array contains detectors with various sensitivities, which allow us to demonstrate the FDM for detectors with different NEPs down to 0.45 aW/$\sqrt{\text{Hz}}$. Our focus is to compare the performance of TES bolometers when they are operated in SPM or MM.

6.2. Experimental setup

Fig. 6.1 shows the cold electronics part of our FDM demonstrator that contains a TES array of 176-pixels, two LC filter chips with 88 resonators each, and SQUID amplifiers. Both the TES array and the filter chips are exactly the same as used in our previous work to address the crosstalk [17]. Co-planar wiring lines connect all the bolometers on the detector array chip for easy fabrication, while microstrip lines are used on the LC filter chips and to connect the LC filter chip to the SQUID for low mutual inductance. Nowadays microstrip lines are also used for TES arrays. All the wire bonds are Aluminum, which is superconducting at the operating temperature. All parts are mounted inside a copper sample enclosure, which is physically closed, but has been found not to be fully light-tight based on the results in [18]. An adiabatic demagnetization refrigerator (ADR) [17] is used to cool down the enclosure. Our measurements were performed at 90 mK and the background magnetic field of the TES was nulled by applying a magnetic field using a Helmholtz coil [17]. In practice, we cannot finish all measurements within one cool-down cycle. Therefore, due to the instability of the cooling power and the presence of 50-Hz noise between two cooling cycles, we observed a maximum 5% and 10% measurement error in current-voltage (IV) curve and noise spectrum, respectively.

Compared to our setup described in reference [17] we have changed the SQUID amplifier and added a resistor-capacitor low-pass filter (LPF), both of which are operated at the bath temperature. The decoupled two-stage SQUID amplifier [20] decreases the readout noise, minimizes the common inductance that is due to inductive coupling of the SQUID, and eliminates the back-action effect [21]. The latter refers to a phenomenon where the feedback noise is added to the input signal. Applying the SQUID calibration tone method described in [22], we measured the readout noise to be 9.5 $pA/\sqrt{Hz}$, a factor of 2.5 lower than the readout noise reported in reference [22], which focuses on SPM. The LPF has a cut off frequency of 7 MHz, and is introduced to minimize the unwanted out of band resonance peaks at 20 MHz and 100 MHz. The series resistance in the circuit when the TES is superconducting is 1.9±0.3 mΩ, which comprises the shunt resistance (1 mΩ) and a parasitic resistance. The common inductance in the SQUID input coil is ≤3 nH. The details of the warm electronics can be found in reference [23], while a diagram of FDM system is also available in the supplementary materials.

We connect half of the TES array to one of the LC filter chips with resonance frequencies ranging from 1 to 3.5 MHz, and frequency spacing of 32 ± 3 kHz. 60 out of 88 resonators had Q-factors higher than 10^4 and were therefore chosen for our FDM experiment. Other pixels either had resonator Q-factor that was too low or an unusable TES, due to defects in the Si_3N_4 legs or issues with wire bonds.

The bolometers are made from $50 \times 50\ \mu m^2$ Ti/Au (16/65 nm) TESs connected to $100 \times 100\ \mu m^2$ Ta absorbers that are 9 nm thick and suspended on top of a 250-nm-thick Si_3N_4 membrane island using four 400-μm-long 2-μm wide Si_3N_4 legs. More device parameters can be found in reference[17]. For this experiment, we measured the DC normal resistance (R_n) of some pixels (pixels 1, 17, 29, 58) in the array separately and found it to be 200 ± 10 mΩ. We also found the critical temperature (T_c) of the TESs to be 113 ± 3 mK and to be relatively constant within the array. The latter is found by fitting the measured saturation power (P_{sat}) of the TESs at different operating temperatures.

An NEP of 0.7 $aW/\sqrt{Hz}$ is expected from the nominal values of the designed T_c (100 mK) and thermal conductance (G; 0.8 pW/K). However, by performing IV measurements at different bath temperatures we found that G varies from 0.16 to 1.10 pW/K, a factor of 6.8. These data were taken from seven pixels across the entire bias frequency range. The variation in G could not be explained by deviations in the width of the legs since they are found to be

constant and close to the nominal value. Therefore we attribute the variation in G to the wet-etching process [24,25] used to fabricate the TESs.

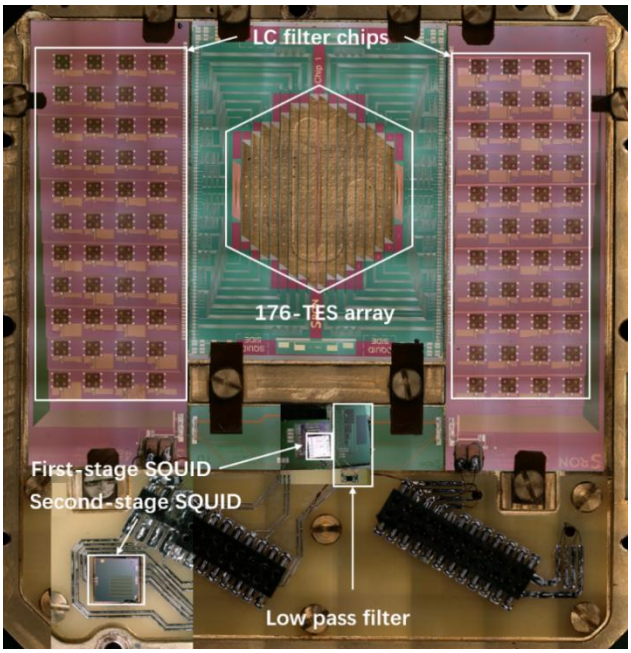

Fig. 6.1 Photo of the cold electronics part of an FDM readout demonstrator with two SQUID chips at the bottom. One half array of 88-pixels is connected to one of the LC filter chips. An RC low pass filter is introduced to eliminate the out-of-band resonance peaks.

6.3. Results and Discussions

Before addressing the properties of the 60 pixels from the array, we focus first on one pixel, i.e. pixel 29, as an example, operated at a biasing frequency of 2.2 MHz. Fig. 6.2 shows comparisons of the detector characteristics measured in either SPM or MM. The calibrated IV curves of pixel 29 are shown in Fig. 2 (a) and are essentially same in the two modes. However, there is a small deviation (<5%) between the two modes when the TES is biased at a low voltage (≤25 nV), which corresponds to a relatively low part of the transition

region ($R_{TES}/R_n < 20\%$) and does not affect detector operation in practice. Fig. 2 (b) shows the observed saturation power (P_s) at different bias points along the resistive transition, measured in both modes. The P_s at 90 mK is 7.83 fW in SPM and 7.93 fW in MM, with a relative difference of only 1.2%. Thus they agree within the measurement error. The inset of Fig. 6.2 (b) shows a fit of measured P_{sat} at different bath temperatures in SPM to the equation, $P_{sat} = K(T_c^n - T_{bath}^n)$ [26], for the power flow to the bath, where K is a scaling parameter for the heat flux and n is a factor reflecting the thermal characteristics of the legs, which ranges from 2 to 4 (~2.5 for this pixel). G is found to be 0.43 pW/K, derived from the expression: $G = \frac{dP}{dT} = nKT_c^{n-1}$, where the T_c is 113 mK. Now, the phonon noise limited NEP, which is given by $\sqrt{4\gamma k_B G T_c^2}$, with $\gamma = 1$ (for our case according to reference [26]) and k_B being Boltzmann's constant, is estimated to be 0.54 aW/$\sqrt{Hz}$.

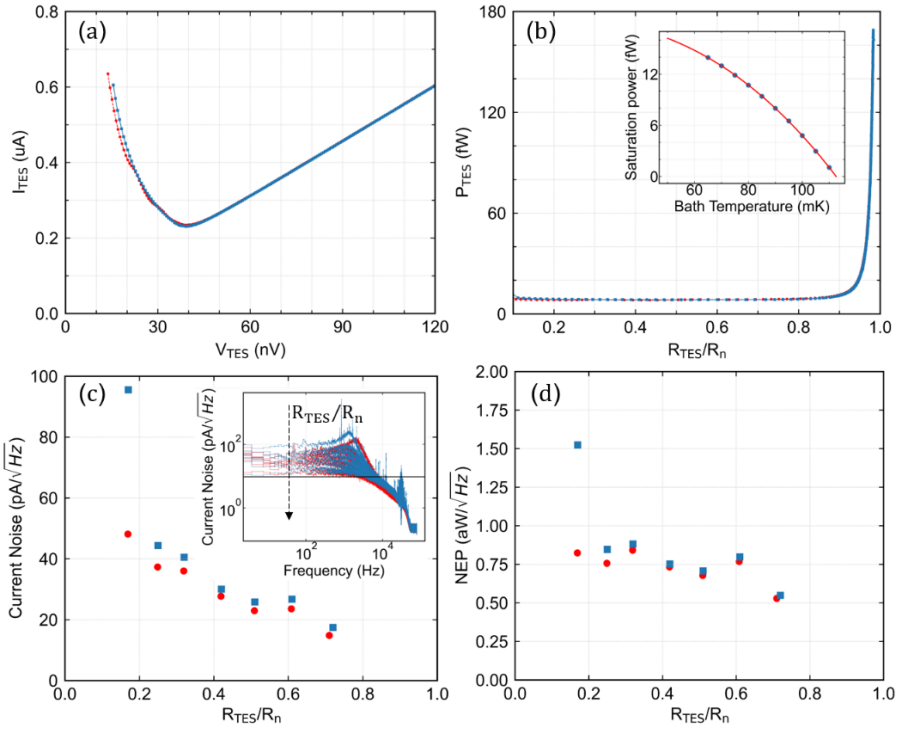

Fig. 6.2 (a) IV characteristics of a TES bolometer (pixel 29) in SPM (dashed lines in red) and MM (solid lines in blue). (b) Saturation power at different transition points, R_{TES}/R_n, compared in SPM and MM. The inset of (b) is the

power plateau fit with saturation power measured at different operating temperatures. (c) Current noise spectra in SPM (red filled circles) and MM (blue filled squares). Inset in (c) : Current noise spectra in SPM and MM. The constant line indicates the readout noise level of 9.5 pA/$\sqrt{\text{Hz}}$; (d) NEP plot at different transition points measured in SPM and MM. There is a significant difference in the first data point between SPM and MM because the noise increases due to oscillations in MM when the TES is biased in $R_{TES}/R_n \sim 0.17$.

The inset in Fig. 6.2 (c) shows the full current-noise spectra of pixel 29 at various bias points in SPM and MM. When the detector is biased low in the transition, there can be oscillations that appear in the noise spectra because the TES response time ($\tau_{eff} \sim \frac{C}{\alpha G} \approx 0.2$ ms) is too close to that of the readout electronics ($\tau_{el} \sim \frac{L}{R_{TES}} \approx 0.17$ ms), causing an underdamped response. Fig. 6.2 (c) plots the average current noise values between 20 and 200 Hz at bias points in the range $R_{TES}/R_n = 17\%$ to 71% in both modes. We notice that the measured current noise levels are the same in both modes except for bias points low on the transition ($R_{TES}/R_n < 25\%$), in good agreement with what we observed in the IV curves. When pixel 29 is biased below 25% in transition, the time constant of this pixel is comparable to the electrical response time constant. In MM, a small current leakage decreases the bias voltage of this pixel, and thus may cause oscillations and raise the current noise level .

Fig. 6.2 (d) shows the NEP versus bias point, derived from the average current noise values from Fig. 6.2 (c) after subtracting the readout noise. Here the NEP is calculated by dividing the current noise by the responsivity of $\frac{1}{V_{TES}}$, where V_{TES} is the TES bias voltage. We found that the differences in NEP between SPM and MM are small and less than 10% except for the data at the low bias of $R_{TES}/R_n \leq 25\%$. The latter are expected from the corresponding current noise. The data at the bias of 51% for R_{TES}/R_n shows that the NEP is 0.72 aW/$\sqrt{\text{Hz}}$ in SPM and 0.79 aW/$\sqrt{\text{Hz}}$ in MM with a difference of 0.07 aW/$\sqrt{\text{Hz}}$. We noticed that the NEP either in SPM or MM is higher than the phonon noise limited NEP of 0.54 aW/$\sqrt{\text{Hz}}$, as given earlier. The difference is likely due to the excess noise [26] and photon noise in the setup, to be discussed later. We also find a clear drop of NEP at R_{TES}/R_n=71% in the same figure. In this case the NEP is underestimated due to the use of the responsivity of $\frac{1}{V_{TES}}$, which is not applicable at the high bias points. The correct way to estimate the responsivity uses the expression, $\frac{1}{V_{TES}}(1 + \frac{1+\beta}{\mathcal{L}})^{-1}$, where β is the

current responsivity and $\mathcal{L}$ the loop gain [26]. At a bias of 71% or higher, as the bias increases, $\mathcal{L}$ decreases and approaches 1, while β approaches 0, so the responsivity can be no less than half of the value used at R_{TES}/R_n<70%. As will be mentioned later, this underestimation contributes to the scattering of measured NEPs in the array.

Next, we measured the properties of the full array. The NEP and P_{sat} of all 60-pixels, biased in the frequency range from 1 to 3.5 MHz and measured in both SPM and MM, are shown in Fig. 6.3 (a) and (b), respectively. We found the NEPs to be in a range between 0.3 and 1.8 aW/$\sqrt{\text{Hz}}$ among the 60 pixels, while P_{sat} varies from 2 to 25 fW. 20 out of these 60 pixels could not be biased below R_{TES}/R_n= 70%, due to oscillations. Therefore, the NEP values of these pixels have been underestimated in both SPM and MM by the same factor.

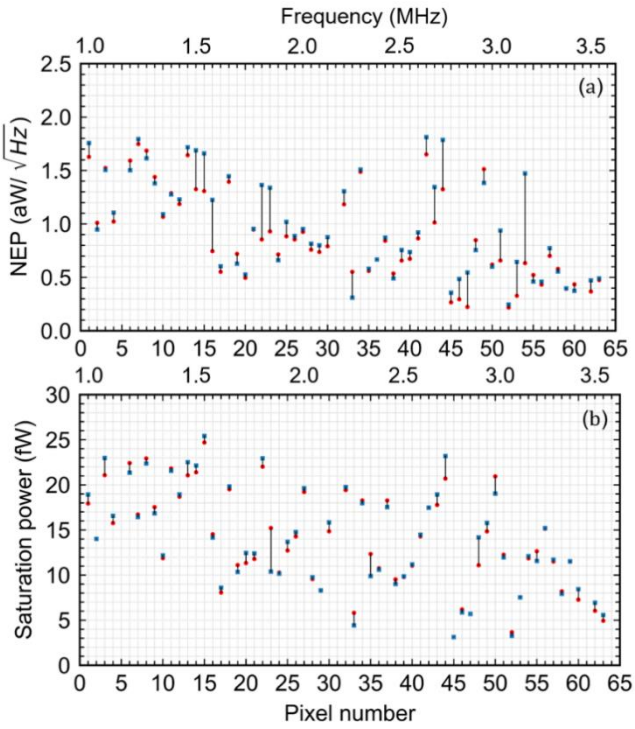

Fig. 6.3 (a) Measured NEPs of 60 TES pixels in both SPM (filled circles in red) and MM (filled squares in blue), where the abscissa in the bottom panel is the

pixel number, while that in the top panel is the bias frequency for the pixel. The black lines between two squares indicate the differences measured between two modes. (b) Saturation power of 60 pixels in both SPM and MM.

The key result of our study is presented in Fig. 6.4, which shows a detailed comparison of the NEP and P_{sat} of 60 pixels measured in SPM and MM according to the layout of TES pixels in the array.

We found that 43 pixels out of 60 have shown a difference of not more than 10% in NEPs and 5% in P_{sat} between SPM and MM. Both of these differences could be calibrated out by measuring the response of the detectors to a known optical source [27]. These results show that our FDM demonstrator is able to measure multiple bolometers simultaneously. Among these 43 pixels, one pixel (pixel 56) has an NEP of 0.45 $aW/\sqrt{Hz}$. This low NEP was confirmed by a separate analysis using the full expression in reference [26] for the NEP, using α, β from the measured complex impedance [28] and other parameters (e.g. T_c, G) of the pixel. The latter gives a NEP of 0.43 $aW/\sqrt{Hz}$. This particular result thus suggests our FDM is able to read out a low NEP level, approaching the requirement for SAFARI ($\sim$0.2 $aW/\sqrt{Hz}$).

There are 17 pixels that show more than 10% difference in the measured NEPs between SPM and MM, and even up to 78% in the worst case, while the difference in P_{sat} is near zero or much less significant. The large differences in NEPs are caused by high crosstalk, previously discovered and characterized in those pixels [17]. Pixels 15, 16, 33, 43-47, and 53 (nine pixels in total) have high crosstalk due to carrier leakage and to mutual inductance in the co-planar wires, which could be minimized by microstrip wiring [17]. Pixels 14, 22, 23 and 31 (four pixels) are biased at the edge of oscillations, i.e. the TES time constant is comparable to the electrical response time constant. In this case, a small current leakage will decrease the bias voltage of those pixels, which in turn causes oscillations and raises the current noise level. Pixels 51, 54, 60 and 62 (four pixels) are operated at the higher bias frequencies and have a narrow frequency spacing of $\sim$26 kHz. This narrower frequency spacing could lead to higher carrier leakage, thus increasing the measured NEP.

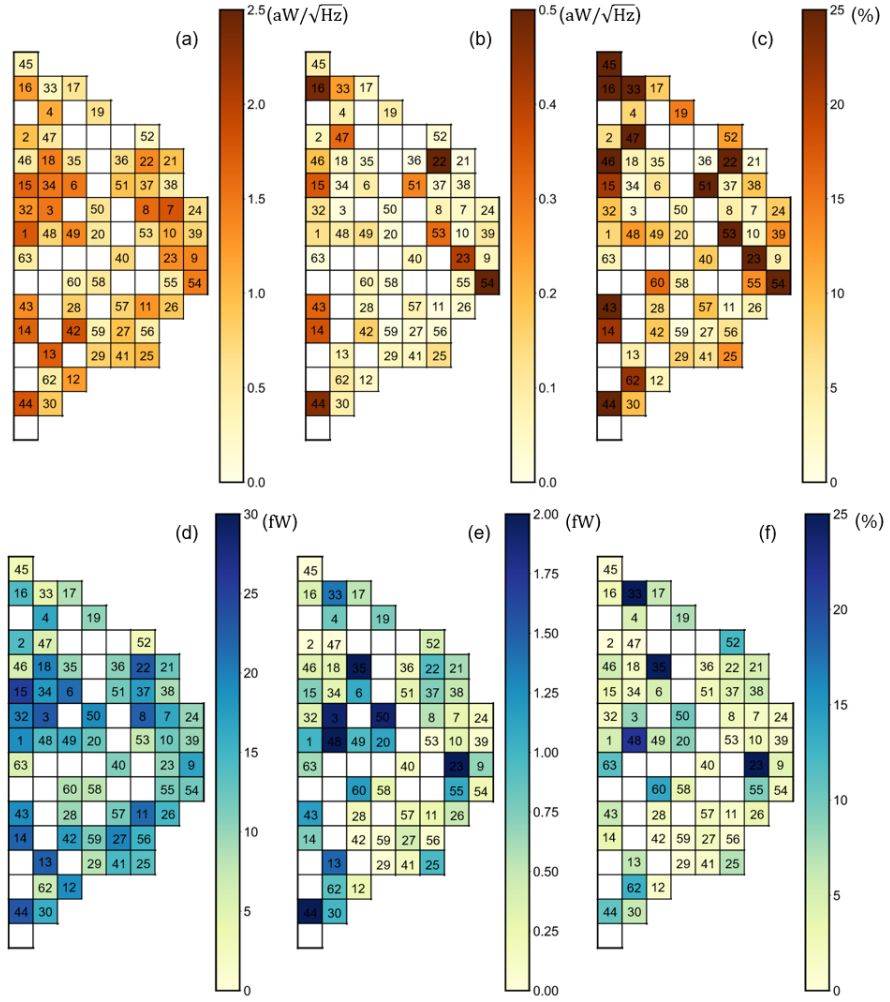

Fig. 6.4 (a) Map of NEP according to the layout of the TES array, measured in MM. The number inside each square denotes the pixel number; (b) Mapped differences of the NEPs between SPM and MM; (c) Mapped differences of NEP in percentage between single-pixel and multiplexing modes derived from (b) with respect to the NEP in (a); (d) Mapped saturation power according to the layout of TES array in the MM; (e) Saturation power differences measured between the two modes. (f) Map of percentage differences of the saturation power between the two modes.

We noticed a large variation in the measured NEPs and P_{sat} among the 60 pixels. The known variations in G from a limited number of tested pixels can cause the phonon-noise dominated NEPs to vary at least from 0.3 to 0.9 $aW/\sqrt{Hz}$. This range becomes larger if we include the influence of the excess noise [29]. Furthermore, there are two other mechanisms that can increase the variation in NEP. First, the photon noise due to optical loading from non-uniformly distributed stray light can increase NEPs. The stray light can also lead to the underestimation of G. However, the latter should be a small effect because of limited loading power [25]. Second, the NEPs of the pixels that could not be biased lower than 70% in the transition can be underestimated. A further discussion is beyond the scope of this letter.

6.4. Conclusions

In conclusion, we have succeeded in demonstrating a low noise FDM system to read out 60 TES pixels of an array by comparing the NEPs and P_{sat} measured in single-pixel mode and multiplexing mode. The readout noise is below the noise from the detectors. We find 43 of 60 pixels to have a difference in NEPs of less than or equal to 10% and a difference in the saturation power is ≤ 5%, both of which are within the measurement error range. For these 43 pixels, the low NEP is 0.45 $aW/\sqrt{Hz}$. The other 17 pixels show large differences in NEPs between the single-pixel mode and multiplexing mode that is due to the high crosstalk level. To advance the demonstrator to an FDM system that satisfies the requirements for space applications like SAFARI, we need to produce an array with slower and lower-NEP TES bolometers (≤ $0.2aW/\sqrt{Hz}$) and perform the measurement in a fully light-tight setup. Furthermore, we expect to be able to use our readout system up to 5 MHz [4], which enables a multiplexing factor of ≥ 130.

References

[1] T. M. Lanting, H.-M. Cho, J. Clarke, W. L. Holzapfel, A. T. Lee, M. Lueker, et al., "Frequency-domain multiplexed readout of transition-edge sensor arrays with a superconducting quantum interference device", Appl. Phys. Lett. 86, 112511 (2005).

[2] M. A. Dobbs, M. Lueker, K. Aird, A. Bender, L. Bleem, J. Carlstrom, et al., "Frequency multiplexed superconducting quantum interference device readout of large bolometer arrays for cosmic microwave background measurements", Rev. Sci. Instrum. 83, 073113 (2012).

[3] B. D. Jackson, P. de Korte, J. van der Kuur, P. Mauskopf, J. Beyer, M. Bruijn, et al., "The SPICA-SAFARI Detector System: TES Detector Arrays With Frequency-Division Multiplexed SQUID Readout", IEEE Trans. Terahertz Sci. Technol. 2, 12 (2012).

[4] L. Gottardi and K. Nagayashi, "A Review of X-ray Microcalorimeters Based on Superconducting Transition Edge Sensors for Astrophysics and Particle Physics", Appl. Sci. 11, 3793 (2021).

[5] W. B. Doriese, J. A. Beall, S. Deiker, W. D. Duncan, L. Ferreira, G. C. Hilton, et al., "High-resolution gamma-ray spectroscopy with a microwave-multiplexed transition-edge sensor array", Appl. Phys. Lett. 85, 4762 (2004).

[6] J. A. B. Mates, G. C. Hilton, K. D. Irwin, L. R. Vale, and K. W. Lehnert, "Demonstration of a multiplexer of dissipationless superconducting quantum interference devices", Appl. Phys. Lett. 92, 023514 (2008).

[7] Y. Nakashima, F. Hirayama, S. Kohjiro, H. Yamamori, S. Nagasawa, A. Sato, et al., "Low-noise microwave SQUID multiplexed readout of 38 x-ray transition-edge sensor microcalorimeters", Appl. Phys. Lett. 117, 122601 (2020).

[8] D. Schwan, P. A. R. Ade, K. Basu, A. N. Bender, F. Bertoldi, H.-M. Cho, et al., "Frequency multiplexed superconducting quantum interference device readout of large bolometer arrays for cosmic microwave background measurements", Rev. Sci. Instrum. 82, 091301 (2011).

[9] J. Montgomery, A. J. Anderson, J. S. Avva, A. N. Bender, M. A. Dobbs, D. Dutcher, et al., "Performance and characterization of the SPT-3G digital frequency multiplexed readout system using an improved noise and crosstalk model", Proc. SPIE. 114530X (2020).

[10] G. Signorelli, A. Baldini, C. Bemporad, M. Biasotti, F. Cei, V. Ceriale, et al., "A 16 channel frequency-domain-modulation readout system with custom superconducting LC filters for the SWIPE instrument of the balloon-borne LSPE experiment", Nucl. Instrum. Methods Phys. Res. 824, 184 (2016).

[11] A. Tartari, A. Baldini, F. Cei, L. Galli, M. Grassi, D. Nicolo, et al., "Development and Testing of the FDM Read-Out of the TES Arrays Aboard the LSPE/SWIPE Balloon-Borne Experiment", J. Low Temp. Phys. 199, 212 (2020).

[12] G. Jaehnig, K. Arnold, J. Austermann, D. Becker, S. Duff, N. Halverson, et al., "Development of Space-Optimized TES Bolometer Arrays for LiteBIRD", J. Low Temp. Phys. 199, 646 (2020).

[13] P. R. Roelfsema, H. Shibai, L. Armus, D. Arrazola, M. Audard, M. D. Audley, et al., "SPICA-A Large Cryogenic Infrared Space Telescope: Unveiling the Obscured Universe", Publ. Astron. Soc. Aust. 35, e030 (2018).

[14] M. D. Audley, G. de Lange, J. R. Gao, B. D. Jackson, R. A. Hijmering, M. L. Ridder, et al., "The SAFARI detector system", Proc. SPIE 107080K (2018).

[15] M. L. Ridder, P. Khosropanah, R. A. Hijmering, T. Suzuki, M. P. Bruijn, H. F. C. Hoevers, et al., "Fabrication of Low-Noise TES Arrays for the SAFARI Instrument on SPICA", J. Low Temp. Phys. 184, 60 (2016).

[16] M.P. Bruijn., A. J. van der Linden, L. Ferrari, L. Gottardi, J. v. d. Kuur, R. H. d. Hartog, et al., "LC Filters for FDM Readout of the X-IFU TES Calorimeter Instrument on Athena", J. Low Temp. Phys. 193, 661 (2018).

[17] Q. Wang, P. Khosropanah, J. van der Kuur, G. de Lange, M. D. Audley,A. Aminaei, et al., "Electrical crosstalk of a frequency division multiplexing readout for a transition edge sensor bolometer array", Rev. Sci. Instrum. 92, 014710 (2021).

[18] T. Suzuki, P. Khosropanah, M. L. Ridder, R. A. Hijmering, J. R. Gao, H. Akamatsu, et al., "Development of Ultra-Low-Noise TES Bolometer Arrays", J. Low Temp. Phys. 184, 52 (2016).

[19] R. Hijmering, R. d. Hartog, M. Ridder, A. J. v. d. Linden, J. v.d Kuur, J.R. Gao, et al., "Readout of a 176 pixel FDM system for SAFARI TES arrays", Proc SPIE. 99141C (2016).

[20] K. Mikko, G. Leif, and S. Hannu, "Two-stage locally linearized SQUID readout for frequency domain multiplexed calorimeter arrays", Supercond. Sci. Technol. 24, 049501 (2011).

[21] P. Falferi, M. Bonaldi, M. Cerdonio, A. Vinante, and S. Vitale, Appl. Phys. Lett. 73, 3589 (1998).

[22] M. Audley, Q. Wang, R. Hijmering, P. Khosropanah, G. de Lange, A. J. van der Linden, et al., "SQUID Noise in a 176-Pixel FDM Demonstrator for the SAFARI Far-Infrared Spectrometer", J. Low Temp. Phys. 199, 723 (2020).

[23] Q. Wang, M. Audley, P. Khosropanah, J. v d Kuur, G. de Lange, A. Aminaei, et al., "Noise Measurements of a Low-Noise Amplifier in the FDM Readout System for SAFARI", J. Low Temp. Phys. 199, 817 (2020).

[24] In the wet-etching process we first removed the Si substrate with a KOH solution and further processing is done on the thin Si3N4 membrane. We suspect that during the RIE etching of the Si3N4 legs also the backside of the legs was attacked by the etching gas leading to changes in surface roughness of the legs which could give additional scattering.

[25] D. J. Goldie, A. V. Velichko, D. M. Glowacka, and S. Withington, "Ultra-low-noise MoCu transition edge sensors for space applications", J. Appl. Phys. 109, 084507 (2011).

[26] K. Irwin and G. Hilton, Berlin, "Transition-Edge Sensors", Heidelberg: Springer, 63 (2005).

[27] M. D. Audley, G. de Lange, J-R. Gao, P. Khosropanah, R. Hijmering, M. Ridder, et al., "Optical performance of an ultra-sensitive horn-coupled transition-edge-sensor bolometer with hemispherical backshort in the far infrared", Rev. Sci. Instrum. 87, 043103 (2016).

[28] E. Taralli, P. Khosropanah, L. Gottardi, K. Nagayoshi, M. L. Ridder, M. P. Bruijn, et al., "Complex impedance of TESs under AC bias using FDM readout system", AIP Adv. 9, 045324 (2019).

[29] P. Khosropanah, T. Suzuki, M. L. Ridder, R. A. Hijmering, H. Akamatsu, L. Gottardi, et al., "Ultra-low noise TES bolometer arrays for SAFARI instrument on SPICA", Proc SPIE. 99140B (2016).

Supplementary materials

A. The diagram of FDM readout electronics

The diagram of FDM readout system is shown in Fig. S 6.1. The difference in this setup is we change the single-stage SQUID to two-stage SQUID. The parameters of the FDM readout system is shown in Table S1.

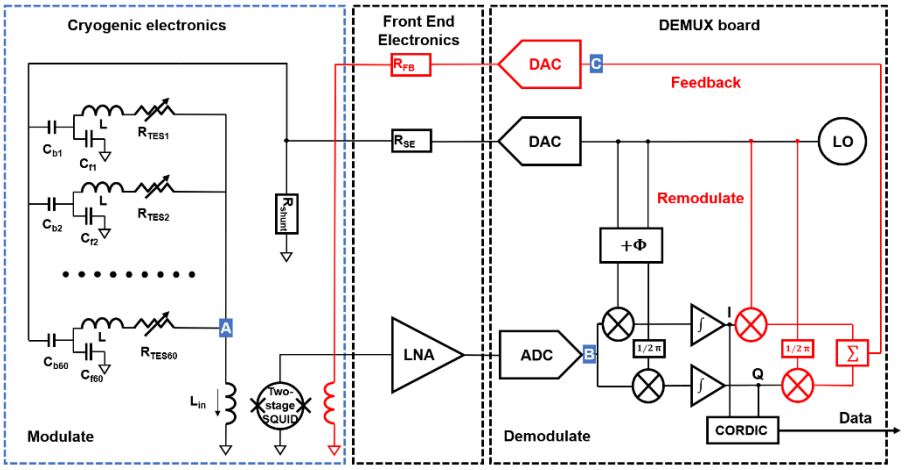

Fig. S 6.1. FDM readout electrical schematic with baseband feedback (BBFB). The DAC provides AC bias voltages in the frequencies corresponding to the resonance frequencies of LC filters for the TES bolometers. The currents through TES bolometers are summed at the input coil of the SQUID amplifier, indicated by point A. The SQUID amplifies the amplitude-modulated signals at its output. After further amplification by the room-temperature LNA, the signal (at point B) is demodulated to I and Q information, then collected by using a CORDIC (COordinate Rotation DIgital Computer). In the feedback process, these signals are re-modulated and applied to the feedback coil (at point C) of the SQUID with appropriate phase shifts to cancel out the SQUID output.

Table S 6.1 FDM system parameters

TES normal state resistance: 200 ± 10 mΩ	Yield of TES and LC filters: 60 out of 84
TES critical temperature:113 ± 3 mK	Inductance of LC filters: 3 μH
TES Ti/Au bolometer size: 50 × 50 μm^2	Capacitance of LC filters: 1 nF–9 nF
TES Ta absorber size: 100 × 100 μm^2	Carrier frequency f_0: 1 MHz–3.5 MHz
TES Ta absorber thickness: 9 nm	Frequency spacing Δf: 32 ± 3 kHz
TES Si_3N_4 legs volume: 400 × 2 × 0.25 μm^3	$\Delta f / f_0$: 0.09–0.32
Designed NEP level: 0.7 $aW/\sqrt{Hz}$	SQUID common inductance: ≤ 3 nH
Shunt resistance: 1 mΩ	Readout current noise: 9.5 $pA/\sqrt{Hz}$
First-stage SQUID mutual inductance: 13 $\mu A/\Phi_0$	Second-stage SQUID mutual inductance: 34 $\mu A/\Phi_0$
First-stage SQUID self-inductance: 70 pH	Second-stage SQUID self-inductance: 40 pH
First-stage SQUID dissipation power: 2 nW	Second-stage SQUID dissipation power: 750 nW

We have 84 TESs and 4 simple resistors (for calibration purposes) connected to 88 resonators. Among these 84 pixels, some TES detectors legs are damaged

(some fab related and some due to transport and handling) and some bonding pads are not working. So we eventually successfully connected 70 pixels with LC filters. Then we performed NWA scan, and quantified Q-factors of all the resonators. Finally, we chose the 60 pixels that were connected to well behaving LC resonators with Q factors higher than 10^4 and increase with resonance frequency as described in reference[1].

B. The power consumption of warm electronics

The warm electronics is based on a VIRTEX V FPGA, which is for the lab demonstrator. At the moment, the warm electronics will dissipate totally about 130 W for a 3600-pixel bolometer array. For the space application, the power consumption can be considerably lowered by using an ASIC (Application Specific Integrated Circuit) based system.

References

[1] M.P. Bruijn., A. J. van der Linden, L. Ferrari, L. Gottardi, J. v. d. Kuur, R. H. d. Hartog, et al., "LC Filters for FDM Readout of the X-IFU TES Calorimeter Instrument on Athena", J. Low Temp. Phys. **193**, 661 (2018).

Chapter 7

Frequency division multiplexing readout of a microstrip wired, slow TES bolometer array

Based on

Q. Wang, P. Khosropanah, J. van der Kuur, G. de Lange, M. D. Audley, A. Aminaei, M. L. Ridder, S. Ilyas, A.J. van der Linden, M. P. Bruijn, F. van der Tak, and J.R. Gao, to be submitted to Rev. Sci. Instrum. (2021).

We demonstrate multiplexing readouts of 43 slow transition edge sensor (TES) bolometers operating at 90 mK using a Frequency Division Multiplexing (FDM) readout chain with a bias frequency ranging from 1 to 3.5 MHz and with a typical frequency spacing of 32 kHz. We improve the performance of our FDM system by two important steps. Firstly, we replace the coplanar wire with microstrips, which minimize the crosstalk from mutual inductance. From the measured electrical crosstalk (ECT) map, the ECT of all pixels is carrier leakage dominated. Only 5 pixels show an ECT level higher than 1%. Secondly, we increase the thermal response time of the TES detectors by a factor of 20, by increasing the heat capacity of the TESs, which allows us to bias all TES detectors below 50% in transition without oscillations. We compare the current-voltage curves and noise spectra of the TESs measured in single-pixel mode and multiplexing mode. We also compare the noise equivalent power (NEP) and the saturation power of the bolometers in both modes, where 38 pixels show less than 10% difference in NEP and 5% in saturation power when measured in single pixel and multiplex mode. The measured noise spectrum is in good agreement with the simulated noise based on measured parameters from an impedance measurement, confirming that our TES is dominated by phonon noise.

7.1. Introduction

Transition edge sensor (TES) bolometer arrays are important for the next generation of far-infrared space observatories [1,2]. TES has some advantages over kinetic inductance detectors (KIDs) such as technological maturity and versatility in readout schemes [2]. Multiplexing techniques are essential to read out TES arrays due to the fact that they can decrease the number of cold wires, thus, minimizing heat load on the cold stage [2,3]. Frequency division multiplexing (FDM) is one of the most promising techniques for the readout of TES bolometer arrays [3,4]. In an FDM readout system, each detector is in series with a specific LC (inductor-capacitor) filter and an array of TESs is AC voltage biased with a comb of frequencies at the resonance frequencies of those LC-filters, typically within a bandwidth of a few MHz [4,5]. The resulting comb of currents is measured by a superconducting quantum interference device (SQUID) and amplified by the rest of the readout chain. In order to increase the number of pixels per SQUID a digitally generated nulling feedback signal is applied to the SQUID [6]. Limited by the bandwidth of the feedback electronics, one readout chain can maximally accommodate the order of 100 pixels. The maximal number of pixels that can be read out by one chain is called the multiplexing factor. Thus, dozens of such readout chains must operate in parallel to read out a large array of 10^3-10^4 detectors. Compared to other promising readout techniques such as time division multiplexing (TDM) [7-9] and microwave-SQUID readout [10-12], the FDM readout techniques show a competitive performance [13,14].

Over the past decade, several FDM readout systems for TES arrays have been developed for ground-based observatories, such as the Atacama pathfinder experiment Sunyaev-Zel'dovich (APEX-SZ) [15], the Third generation South Pole Telescope (SPT-3G) [16] and the Polarization of Background Radiation (POLARBEAR) [17]. The state of the art of the FDM technology is reported in [16], where 206 pixels were successfully read out with six SQUID amplifiers, leading to a multiplexing factor of ~35. Furthermore, this FDM system has a relatively large frequency spacing, which varies from about 40 kHz in the low-frequency range (≤2 MHz) to over 60 kHz in the high-frequency range (≥3 MHz). FDM readout techniques are currently being developed for balloon-borne observatories [18,19,20] and considered for space observatories, such as the Lite satellite for the studies of B-mode polarization and Inflation from cosmic background Radiation Detection (LiteBird) [21,22] and the previously proposed Far-infrared Instrument

(SAFARI) on board of the recently cancelled Space Infrared Telescope for Cosmology and Astrophysics (SPICA) [23,24]. Compared to ground-based instruments, spacecraft platforms usually have limited resources of power, mass and volume [14,23]. Those requirements could restrict the use of the heritage from ground based FDM technology. The requirements of SPICA/SAFARI, for example, not only impose a different configuration of the FDM readout chain than that of ground-based systems, but also require different LC filter designs, e.g., a small frequency spacing and a compact chip design [25]. Up to now, neither a TES array nor an FDM readout system has been flown to space.

Our previous work demonstrated an FDM system that has successfully read out 60 low-noise TES bolometers [26]. However, we also learned from the previous experiment that the crosstalk between pixels connected by coplanar wires in the same bundles is very high due to their mutual inductance. Also, some pixels cannot be biased lower than 70% in transition due to the too fast response of the TES. Furthermore, the noise spectra show some excess noise probably due to stray-light. To mitigate those issues, we have designed and fabricated a new TES array where microstrip wires instead of coplanar wires to connect all the TES are used, an Au structure to enlarge the detector response time is added, and the FIR absorber is removed.

In this paper, we report an FDM experiment, in which 43 slow TES bolometers were simultaneously read out. We mapped the electrical crosstalk (ECT) level of all 43-TES detectors using our FDM system with all the detectors biased in their normal operating transition. The ECT level is dominated by carrier leakage from neighbor pixels with less than 1%, while the other pixels show a level being less than 0.1%. We have successfully increased the TES response time by a factor of 20, which enables us to bias all our pixels lower than 50% in transition without any unwanted oscillations. Since no absorber is present in the TES bolometers, the measured noise spectra match well with those expected by phonon noise.

7.2. Experimental setup

Fig. 7.1 (a) shows the TES array, LC filters, and first-stage SQUID in our FDM setup. A zoomed photo of one TES bolometer from the array is shown in Fig. 7.1 (b). A gold (Au) layer is introduced to increase the heat capacitance and thus increase the response time of the detector. There is no absorber in

the bolometers, so our detector is not sensitive to any optical light. Therefore, our TES bolometer will not suffer from stray light as found in the previous study [26], and the noise will be dominated by phonon noise or other excess noise. Fig. 7.1 (c) shows the decoupled second-stage SQUID from the Technical Research Centre of Finland (VTT), which is located in the same bracket with the TES array. The decoupled two-stage SQUID amplifier [27] decreases the readout noise, minimizes the common inductance that is due to the inductive coupling of the SQUID, and eliminates the back-action effect. The latter refers to a phenomenon where the feedback noise is added to the input signal [26]. The power dissipation of the first-stage SQUID and the second-stage SQUID is 2 nW and 750 nW, respectively. Microstrip wires are used between each TES detector and the bonding pad to decrease mutual inductance in comparison with the coplanar wires in the same bundles in our earlier array [28]. Aluminum wire bonding is applied to connect the TES chip with the LC filter chip, which will be superconducting during measurements. An adiabatic demagnetization refrigerator (ADR) [28] is used to cool down the bracket. Our measurements were performed at 90 mK and the background magnetic field of the TES is nulled. Due to the instability of the cooling power and the presence of 50 Hz noise, we observed a measurement error bar of 5% and 10% in the current-voltage (IV) curve and noise spectrum, respectively [26].

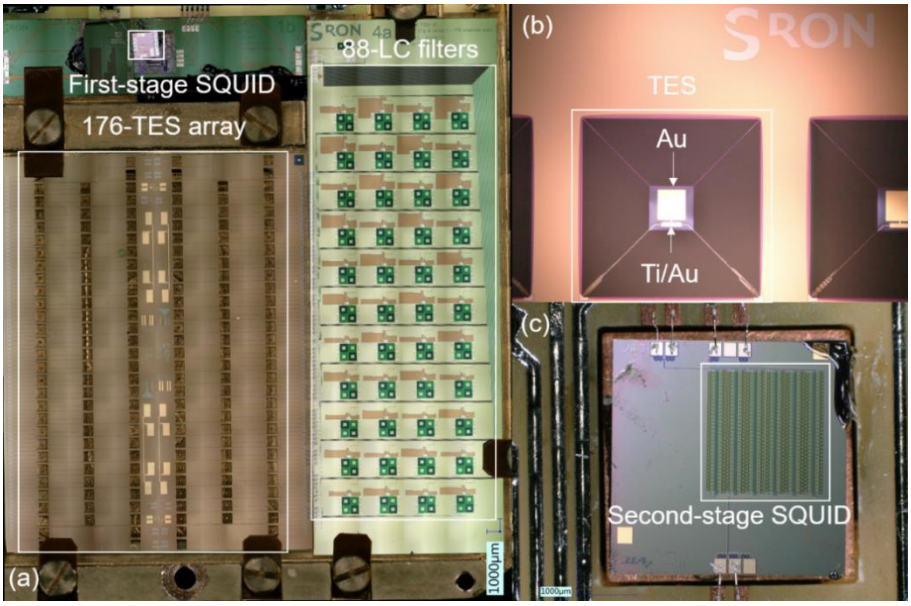

Fig. 7.1 (a) Photo containing the 176-pixel TES array and an 88-LC filter chip, half of the TES array and 88-LC filters being connected via wire bonding. The first-stage SQUID is shown on the top. (b) Zoomed photo of one TES pixel, which contains a 200 nm thick structure to increase heat capacity. There are some structures on some of the Si_3N_4 legs, which might potentially introduce non-uniformity to the thermal conductance. (c) Photo of the second-stage SQUID, which is formed by hundreds of SQUIDs in series.

Although we could have a higher multiplexing factor up to 176 if we connect the whole TES array, the ECT level will be a factor of 4 higher than the case when only half of the TES array is connected. Therefore, to simplify the experiment we chose to connect only half of the TES array to one of the LC filter chips (with 88 resonators) with the resonance frequencies ranging from 1 to 3.5 MHz, and a frequency spacing of 32 ± 4 kHz. After performing an initial network analyzer scan (NWA) via an AC bias line from 1 to 3.5 MHz, we found 70 high-quality-factor ($\geq 10^4$) LC filters among the connected 88 resonators. However, because the yield of a slow TES is relatively low, likely due to the deposition of additional Au, eventually only 43 TES pixels with relatively sharp transitions together with their corresponding LC filters are chosen for our FDM experiment. The relation between pixel number and resonance frequency is shown in Fig. 7.2 (a). Pixel 1 corresponds to the lowest frequency of 1 MHz, while pixel 43 corresponds to the highest frequency of 3.5 MHz in this case. To find the precise resonance frequency, we perform a fine current scan (with feedback on) within 200 Hz around the resonance frequency estimated from the NWA scan. Then, by fitting the measured data, the Q factor of this pixel can be calculated according to $Q = f_0/\Delta f$. f_0 is the resonance frequency and Δf is the frequency bandwidth at full width at half maximum, as shown in Fig. 7.2 (b). The power intensity is normalized with the peak amplitude at the resonance frequency. The Q factor of every pixel is shown in Fig. 7.2 (c), the Q-factors increase with frequency according to $Q \propto 2\pi L f_0/R_s$, where L is the inductance of the LC filters (3μH), and R_s is the series resistance of the circuit when a TES is superconducting, which consists of the shunt resistance (~1 mΩ) and parasitic resistance. L is a constant, and R_s has a relatively constant value in each TES circuit. There is a scattering behavior of the Q factor performance in Fig 7.2 (c), which are mainly due to the variation of series resistance. The value of our series resistance ranges between 1.6 and 2.7 mΩ, as plotted in Fig. 7.2 (d).

The bolometers are based on a Ti/Au (35/185 nm) TES with an area of 20 (Length) × 80 (Width) μm^2 side by side of a 125 × 125 μm^2 thick Au square on a 195 × 195 μm^2 Si_3N_4 membrane island, which is suspended from the Si substrate through four long (400 μm), narrow (2 μm) and thin (250 nm) Si_3N_4 legs. The normal resistance (R_N) is 150 $\pm$ 10 mΩ according to the resistance-temperature (RT) measurement of a witness chip taken from the same TES detector wafer. The critical temperature (T_c) of the TES is 127 $\pm$ 3 mK, which is derived by fitting the measured P_s of the TESs at different bath temperatures. This value is fairly constant (with $\pm$2.5% variation) within the array. The R_s is 2.2 $\pm$ 0.5 mΩ, and the common inductance is $\leq$ 3 nH from VTT's technical note [29]. The details of the warm electronics can be found in [30].

According to the thermal time constant $\tau = C/G$, where C is the heat capacity and G is the thermal conductance of the TES, the response time is proportional to C. Therefore, we decided to introduce a 200 nm Au layer instead of the Tantalum (Ta) absorber in the previous TES array [31] to increase the heat capacity, which is increased by a factor of 6.5 [32]. In practice, we measured the fall time of such a TES as 20 ms when the TES is biased at 70% of R_{TES}/R_nin transition, while the previous TES fall time is 1 ms when it was at the same transition [26]. We measured a larger slow-down factor (20) than the designed one (6.5) due to the fact that the effective time constant depends very strongly on the thermal responsivity (α) of a TES. Although we successfully slowd down our TES, the additional deposition of Au may affect the characteristics of the TES. For example, some pixels showed a wider superconducting- normal transition than what we usually observe. Therefore, those pixels were excluded in our measurements, as mentioned in the choice of pixels for measurement. We noticed additional structures around some Si_3N_4 legs, which could influence the value of G. The material of the additional structure is Si_3N_4, presumably caused by insufficient etching [33].

The normal resistance of the previous TESs is 200 mΩ. Many TES can only be biased higher than 70% in transition, which makes the TES resistance (R_{TES}) to be $\geq$ 140 mΩ. In the new array, all pixels can be biased lower than 50% in transition, which ensures the R_{TES} to be $\leq$ 75 mΩ. Therefore, the bias current electrical bandwidth of the TES, which is defined by $\frac{R_{TES}}{2\pi L}$ becomes at least a factor of 2 smaller than the previous experiment since the R_{TES} is less than half of the previous value. For the slow TES, the bandwidth ratio ($Ratio_{bw}$) of the frequency spacing df_0 (32 kHz) and the electrical bandwidth (4 kHz) is 8, which is a factor of 2 higher than that of the previous TES. Since the carrier

leakage between the neighbor pixels approximately equals $(\frac{R_{TES}}{4\pi df_0 L})^2$ [4,26], a factor of 2 increased in the $Ratio_{bw}$ will cause a factor of 2^2 decrease in the carrier leakage.

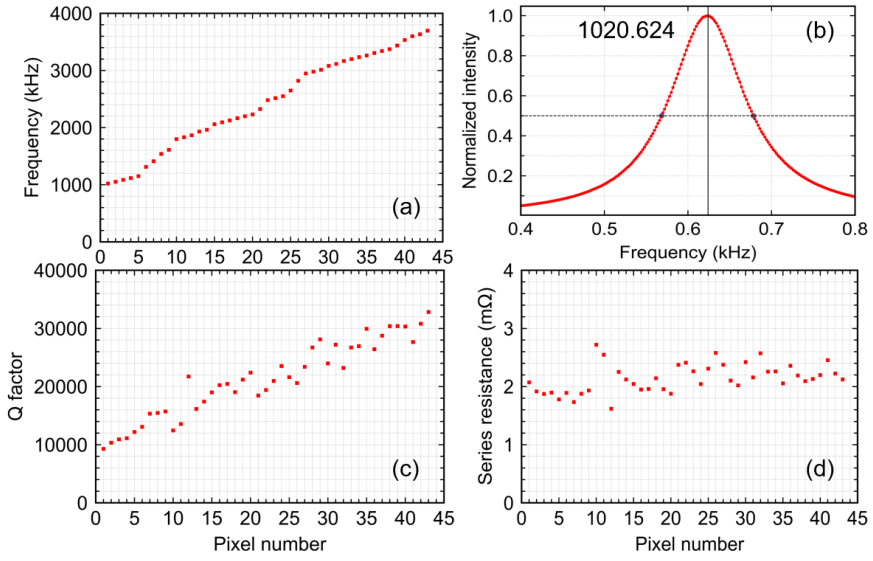

Fig. 7.2 (a) Resonance frequency of the LC filter for each TES is plotted with different pixel numbers. (b) The measured resonance pixel 1 to determine the frequency and Q factor. The resonance frequency of pixel 1 is 1020.624 kHz. (c) The Q factor of all 43 resonators at 90 mK. (d) The series resistances of the circuit when a TES is superconducting for all the pixels.

7.3. Results and Discussion

7.3.1. Map of electrical crosstalk

All 43 TES pixels in the array are biased in the transition of R_{TES}/R_n, which ranges between 10% and 50%, at 90 mK. By applying the ECT mapping technique described in [28], we generate an ECT map of 43 TESs, as shown in Fig. 7.3. Here, we chose 24 Hz as our modulation frequency for ECT

measurements since the thermal roll-off frequency of the TES bolometers is about 50 Hz and since there is low-frequency noise present below 10 Hz.

The ECT map is formed by a 43 × 43 matrix. In each row of the ECT map, the excited pixel number is the same as the row number with 100% level of the ECT (dark blue). The levels of the ECT observed in other pixels when this one is excited are indicated by colors in that row. Similarly, in each column, the responding pixel number is the same as the column number and marked in dark blue. The levels of the ECT observed in this pixel when others are excited are indicated by colors in that column. To highlight the pixels with an ECT larger than 1%, we plot the ECT values that are below 0.1% in the same color as for 0.1%. In other words, in Fig. 7.3, we do not make a difference for ECT values between 0 and 0.1. We find 92.6% of the squares in the 43 × 43 ECT matrix to be light yellow, meaning that their ECT levels are below 0.1%, and some of them even approach zero (according to measured data, as low as 0.01%) although they are not indicated because of the way we plot. Those 92.6% squares with less than 0.1% ECT are the pixels that are far away from the excited pixel in frequency space. This negligibly low ECT level is expected. Because in a carrier leakage dominated system, a factor of 2 increase in the frequency spacing will decrease the ECT by a factor of 2^2. We also observe that about 6.5% of the squares show an ECT level between 0.1% and 1%. Those squares are formed by adjacent pixels in frequency. The expected ECT level between neighbor pixels varies between 0.4% to 0.7% according to the difference in the bias points in transition. Therefore, the measured ECT matches well with the expected ECT. However, we also find that there are about 0.9% of squares showing an ECT level higher than 1%. Those 0.9% of squares correspond to five pixels that have high carrier leakage (pixel 13, 29, 32-33, 41). One reason could be that those pixels have a narrower frequency spacing (i.e. 24 kHz) than the nominal frequency spacing of 32 kHz. The other reason could be that those pixels are not biased in a proper transition region, as to be discussed in section 7.3.3.

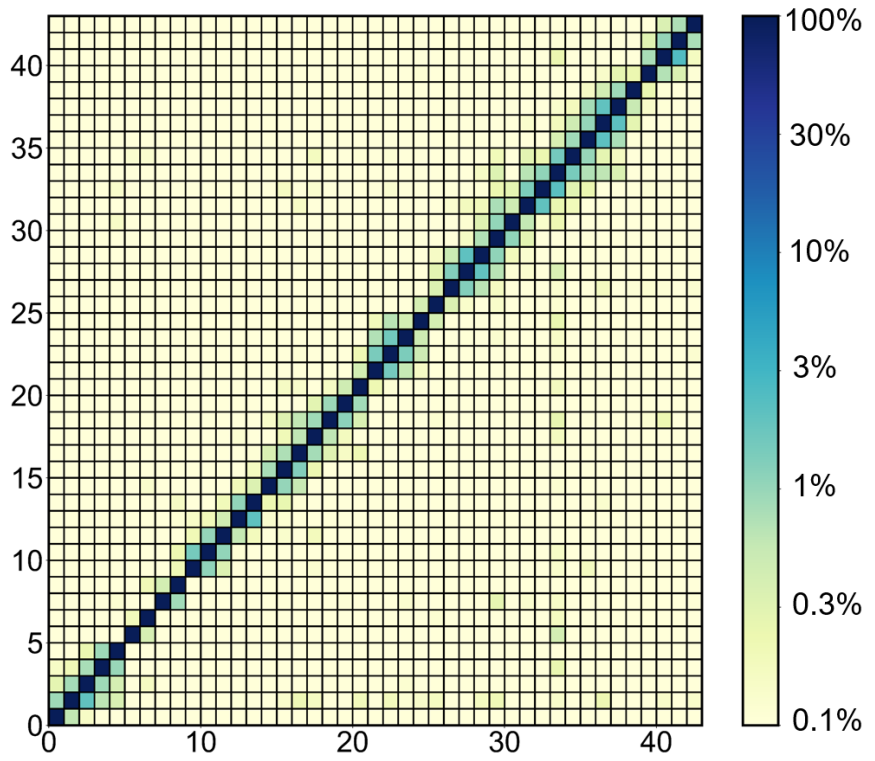

Fig. 7.3 Electrical crosstalk (ECT) map of 43 pixels with a frequency spacing of 32 kHz. In this 43 × 43 matrix, each row presents the ECT level of the pixels, caused by one of the pixels with dark blue color. The number represents the pixel from 1 to 43, which follows the order of the biasing voltage frequency from 1 to 3.5 MHz. The level of the ECT is indicated by color, quantified by the color bar in the figure. The column presents the ECT level of the pixels, which contributes the ECT to the pixel in dark blue (100%). The ECT value of < 0.1% is not different from the level of 0.1% to make higher crosstalk more visible in the map.

7.3.2. Measurements of one pixel

In practice, if ECT levels are sufficiently low, there will be negligible differences in the measured characteristics and the performance of a TES

between single-pixel mode (SPM) and multiplexing mode (MM). Before we show the results of all 43 pixels in the array, we first focus on presenting and analyzing the results of one pixel (pixel 1). The measured raw current-voltage (IV) curves of pixel 1 at 90 mK in single-pixel mode (red line) and multiplexing mode (blue line) are shown in Fig. 7.4 (a). The difference between the two modes is negligible. By using the normal resistance measured from the witness chip, and the current in the feedback circuit, the raw IV can be calibrated and is plotted in Fig. 7.4 (b). The deviation between two IV curves becomes observable only when the TES is biased very low in transition (≤ 5%), because the current leakage from neighbor pixels is comparable to its current [26]. Fig. 7.4 (c) shows the observed saturation power (P_s) at different bias points along with the resistive transition R_{TES}/R_n, measured in both modes. The P_s is 44 fW in SPM and 46 fW in MM, respectively, where the difference of 2 fW accounts for 4.5%, which is within the measurement uncertainty of 5% in IV measurements.

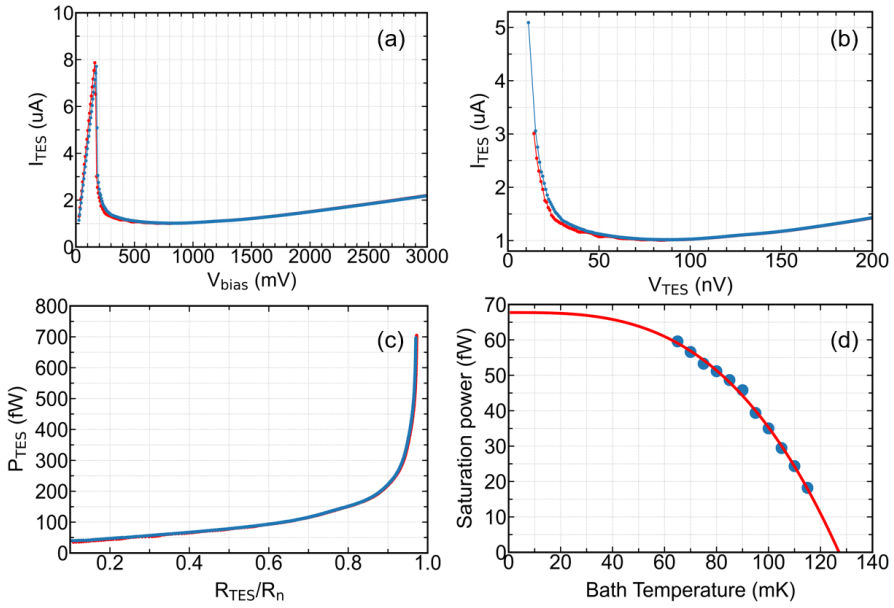

Fig. 7.4. (a) Measured raw IV curve of pixel 1, where the red line means the data measured in single-pixel mode and the blue line means the data measured in multiplexing mode. (b) Calibrated IV from the raw IV curve. (c) PR curve of this pixel. (d) The fitting of measured saturation power as a function of bath temperature. The fitted T_c is 127 mK.

Fig. 7.4 (d) shows the power fit to the P_s data at different bath temperatures, measured in SPM, with the equation: $P_{bath} = K(T_c^n - T_{bath}^n)$. This equation describes the power flow from the TES to the bath, where K is a parameter scaling with the heat flux ($\sim 2.8 \times 10^{-11}$ W/K^n) and n a factor reflecting the characteristic of the thermal legs, which ranges from 2 to 4 ($\sim$3.0 of this pixel). The G is found to be 1.5 ± 0.1 pW/K, derived from the expression: $G = \frac{dP}{dT} = nKT_c^{n-1}$, where the T_c is 127 ± 1 mK. Now, the phonon noise-limited NEP [1], which is given by $\sqrt{4\gamma k_B G T_c^2}$ with $\gamma = 1$ and k_B the Boltzmann constant, is estimated to be 1.2 ± 0.1 aW/$\sqrt{\text{Hz}}$.

We further study the noise performance of pixel 1, which is biased at 20 % of R_{TES}/R_n, as plotted in Fig. 7.5 (a). The readout noise level is 15.5 pA/$\sqrt{\text{Hz}}$, as shown by the green line in the plot. The measured current noise in black matches very well with the simulated current noise (red). The simulated current noise includes phonon noise (blue), Johnson noise (orange), and readout noise (green). The phonon noise is calculated with the parameters extracted from the measurements in Fig. 7.4 (i.e. G, T_c) and the impedance measurement [34]. From the impedance measurement of this pixel, we derive α to be 205, and the current responsivity β to be 1.7. Below the detector roll-off frequency (50 Hz), phonon noise of the blue line contributes mostly to the red line, suggesting that the TES bolometer is phonon noise dominated in the relevant frequency range. The only deviation between the simulated and measured noise occurs at frequencies below 10 Hz, which is probably due to excess noise and 1/f noise. Fig. 7.5 (b) shows the responsivity of this pixel with a value of 2.5×10^7 A/W. Fig. 7.5 (c) shows the estimated NEP of 1.3 ± 0.1 aW/$\sqrt{\text{Hz}}$ from the simulated noise, which is the same as the phonon noise dominated NEP, estimated from G and T_c.

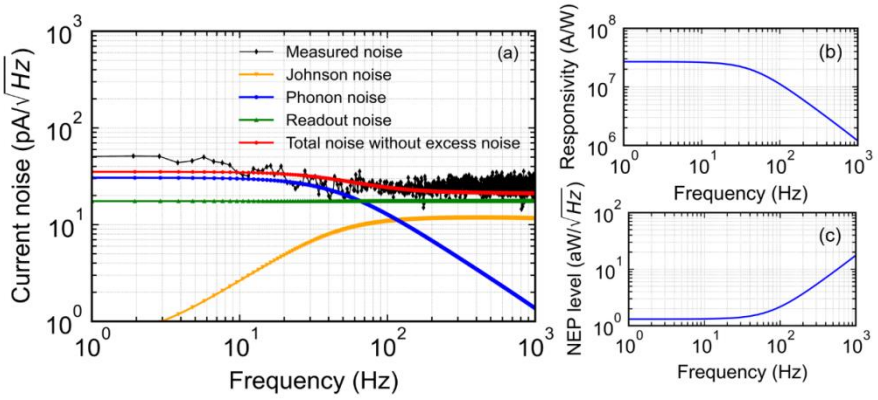

Fig. 7.5 (a) Plot of the measured noise of pixel 1 at 20% in transition and expected noise according to the parameters derived from an impedance measurement. The expected and measured noise match well except for the low-frequency range (< 10Hz); (b) Calculated responsivity of this pixel. (c) NEP calculated with expected noise and responsivity. The NEP is 1.3 aW/$\sqrt{\text{Hz}}$.

7.3.3. Measurements of 43 pixels

Now we turn to the performance of the 43-TES bolometers in SPM and MM. As shown in Fig. 7.6 (a), all detectors are biased in the range between 10% and 50% in transition. Compared with the previous 'fast' TES measurement [26,35], now we are able to bias all detectors below 50% in transition without any oscillations. To increase the signal-to-noise ratio (SNR) in the readout circuit as well as to minimize the carrier leakage, it is preferred to bias our TES as low as possible in transition. However, some TES detectors have unwanted bumpy structures when they are biased at low transition. Therefore, we choose an appropriate bias point where the transition is low and the IV curve is smooth as well. Most pixels behave normally when they are biased between 10% and 50% in transition. However, as we noticed from the ECT map, 5 pixels are likely not biased in a stable operating position in its transition.

Fig. 7.6 (b) shows the TES voltage for each TES when it is biased in the usual operating point. In principle, to calculate the NEP, we need to calculate the current noise divided by the responsivity:

$$\mathrm{NEP_{measured}} = \frac{\sqrt{S^2_{I,\mathrm{measured}} - S^2_{I,\mathrm{read}}}}{s_{AC}}, \tag{7.1}$$

where $\mathrm{NEP_{measured}}$ is the NEP derived from experiment, $S_{I,\mathrm{measured}}$ is the measured current noise, $S_{I,\mathrm{read}}$ is the readout noise, and s_{AC} is the responsivity of the TES. The s_{AC} can be expressed as [1]:

$$s_{AC} = -\frac{1}{V_{TES}}\left(\frac{L}{\tau_{ele} R_{TES} \mathcal{L}} + \left(1 - \frac{R_s}{R_{TES}}\right) + i2\pi f \frac{L\tau}{R_{TES}\mathcal{L}}\left(\frac{1-\mathcal{L}}{\tau} + \frac{1}{\tau_{ele}}\right) - \frac{(2\pi f)^2 \tau}{\mathcal{L}} \frac{L}{R_{TES}}\right)^{-1}, \tag{7.2}$$

where τ_{ele} is the electrical response time that can be represented by $\frac{L}{R_s + R_{TES}(1+\beta)}$ with $\mathcal{L}$ being the loop gain, and f the signal frequency. Since we are only interested in the frequency range smaller than 50 Hz, and $R_s \ll R_{TES}$, Equation (7.2) can be simplified to:

$$s_{AC} = -\frac{1}{V_{TES}}\left(\frac{1+\beta}{\mathcal{L}} + 1\right)^{-1}. \tag{7.3}$$

In practice, the loop gain $\mathcal{L}$ is much larger than 1, so we use V_{TES} and replace $\frac{1}{s_{AC}}$ to derive the $\mathrm{NEP_{measured}}$ by:

$$\mathrm{NEP_{measured}} = V_{TES} \times \sqrt{S^2_{I_{\mathrm{measured}}} - S^2_{I_{\mathrm{read}}}}. \tag{7.4}$$

Fig. 7.6 (c) plots the TES current of each pixel in both SPM and MM. The tendency to the decrease of the TES current corresponds to the tendency to the increase of the transition range in Fig. 7.6 (a) since the TES current is larger when a TES is biased lower in transition. We also notice that the difference in TES current between two modes becomes larger when a TES is biased lower in transition, which is due to the fact that the detector is more sensitive to current change when it is biased lower in transition.

The measured current noise of each pixel in both modes is shown in Fig. 7.6 (d). Most of the current noise values are between 20 and 40 pA/$\sqrt{\text{Hz}}$, which is close to the expected phonon noise values of our TESs, corresponding to the operating region of the transition. Despite that most pixels show the same values in SPM and MM within the measurement error, five of them (pixel 13, 29, 32-33, 41) show a relatively large difference (>10%) between the two modes, which are actually the pixels with a relatively high carrier leakage.

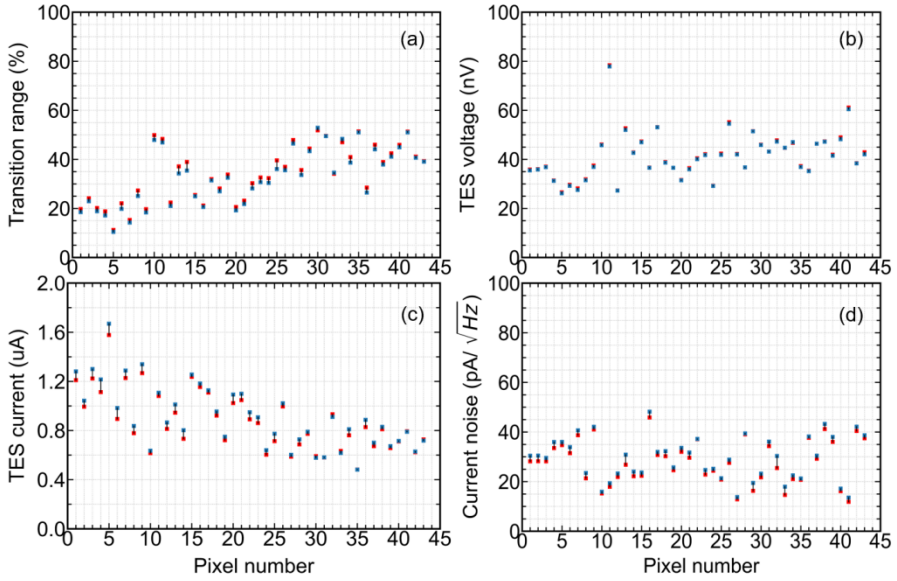

Fig. 7.6 (a) Operating transition range of 43 pixels in SM (red squares) and MM (blue squares). Each pixel has the same bias voltage in both modes. In MM, the transition is slightly lower due to crosstalk although they are very close. (b) The voltage of each TES in both modes. (c) The current of each TES in both modes. The current is a bit higher in MM because it is slightly lower in transition. (d) Current noise of each pixel in both modes. Similar to TES current, the current noise is higher in MM due to the TES is lower in transition.

The P_s is calculated from the calibrated IV curve of each pixel at 90 mK. The NEP and P_s of all 43-pixels, biased in the frequency range from 1 to 3.5 MHz, measured in both SPM and MM are shown in Fig. 7.7 and Fig. 7.8, respectively.

We found the NEPs to be between 0.6 and 1.8 aW/$\sqrt{\text{Hz}}$ among the 43 pixels with a mean value of 1.2 aW/$\sqrt{\text{Hz}}$, while the P_s varies from 20 to 50 fW, with a mean value of 35 fW. The measured NEP and P_s of most pixels is the same in both SPM and MM, which is consistent with the crosstalk measurement, described in section 7.3.1.

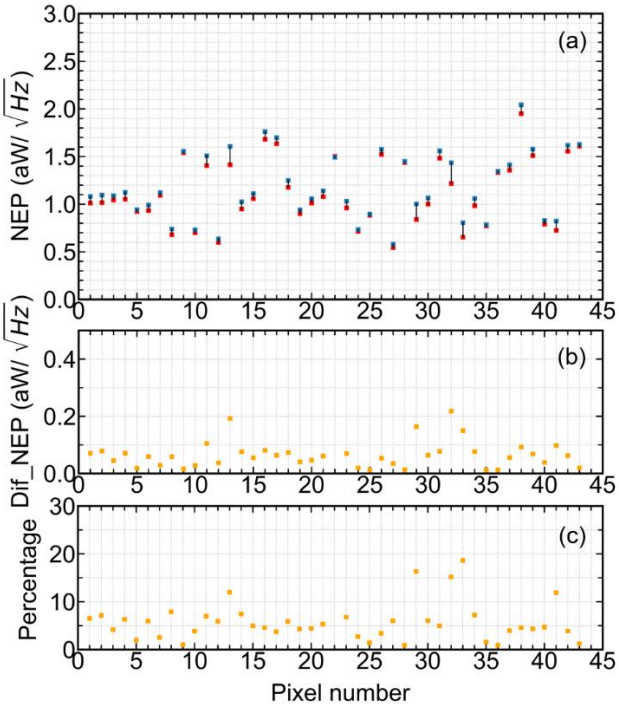

Fig. 7.7 (a) Measured NEP of 43 pixels in SM (red squares) and MM (blue squares). Most NEPs are scattered around 1.2 aW/$\sqrt{\text{Hz}}$, but the value is the same in both modes. (b) Difference between the NEPs in two modes. (c) Difference of NEP in percentage between SM and MM, derived from (b) with respect to the NEP in MM, only five pixels show the difference to be higher than 10% because of the high ECT level (>1%).

Compared with the previous TES array fabricated with the wet-etching process[26], the uniformity of this TES array improves. However, the thermal

conductance is still scattered in a relatively large range (up to a factor of 9). The reason is likely the non-uniformity of TES in the array, which could be caused by remaining structures on some of the Si_3N_4 legs in some TES, as shown in Fig. 7.1 (b). Introducing the Au structure in our TES could be another source of the non-uniformity. It is generally known that TES can be sensitive to any changes in the standard fabrication. As we discussed earlier, no contribution from stray light is expected since no absorber is in the TES detectors. Also, it cannot be due to the crosstalk because its level is low (<1%). Furthermore, since the scattering is not frequency-dependent, any influence from the readout system can be excluded as well.

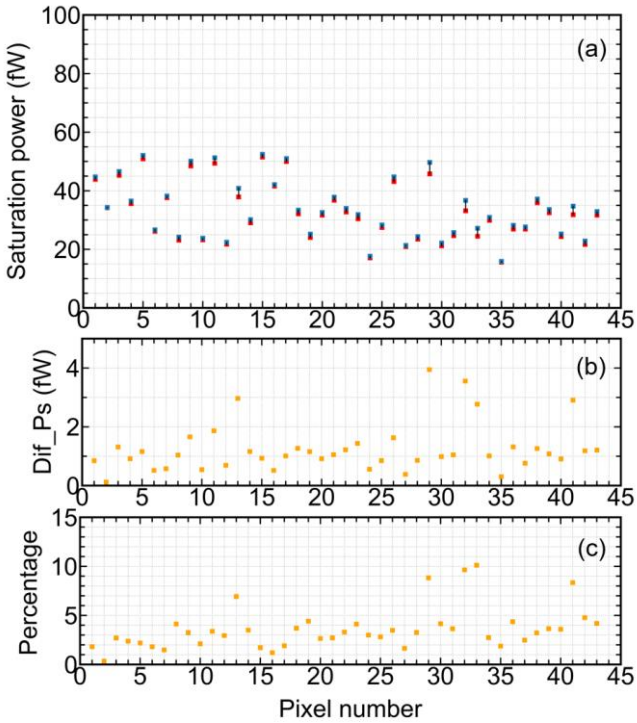

Fig. 7.8 (a) Measured saturation power of 43 pixels in two modes. The P_s value of each pixel is taken from 20% transition. Most saturation powers are scattered around 35 fW, and the values are the same in both modes. (b) The differences of P_s are measured in two modes. (c) Difference of P_s in percentage between SM and MM, derived from (b) with respect to the P_s in MM, only five pixels show the difference to be higher than 5 % because of high ECT level (>1%).

7.4. Conclusions

In conclusion, we have mapped the electrical crosstalk of 43 pixels in an array, with a nominal frequency spacing of 32 kHz. We have found that 38 pixels show an electrical crosstalk level of less than 1%, which is dominated by the carrier leakage. Reduced crosstalk is attributed to the microstrip wiring in the array, which minimizes the mutual inductance. We also observed 5 pixels with a crosstalk level higher than 1% due to the reduced frequency spacing and structured IV curves. Our study suggests that our FDM can have a low enough ECT level such as what was required for SPICA/SAFARI.

We succeeded in increasing the response time of our TES by a factor of 20, achieving an effective time constant of 20 ms at a transition of 70% for R_{TES}/R_n, by adding an Au structure to the TES. Therefore, we not only have a much larger bandwidth ratio (frequency spacing/electrical bandwidth) of 8 but also allow the TES to be biased at a low transition without oscillations.

We have read out 43 pixels simultaneously in the frequency range 1-3.5 MHz, with an NEP level ranging from 0.6 to 1.8 $aW/\sqrt{Hz}$ and with a saturation power varying between 20 and 50 fW. All the pixels show the same results in single-pixel mode and multiplexing mode except for 5 pixels with a high crosstalk level. The measured noise spectrum is in good agreement with the simulated noise based on measured parameters from an impedance measurement, confirming that our TES is dominated by phonon noise.

That 43 pixels were chosen out of the half array (88) for our experiment is unfortunately due to the nonuniformity of the available TES batch. In the future, with a more uniform TES bolometer array and a larger readout bandwidth (up to 5 MHz), we can foresee our FDM reading out 130 pixels in one SQUID readout channel.

References

[1] K. Irwin and G. Hilton, "Transition-Edge Sensors", Berlin, Heidelberg: Springer. 63–150 (2005).

[2] D. Farrah, K. E. Smith, D. Ardila, C. M. Bradford, M. J. DiPirro, C. Ferkinhoff, et al., "Review: far-infrared instrumentation and technological development for the next decade", J. Astron. Telesc. Instrum. Syst. **5,** 1– 34 (2019).

[3] T. M. Lanting, H.-M. Cho, J. Clarke, W. L. Holzapfel, A. T. Lee, M. Lueker, et al., "Frequency-domain multiplexed readout of transition-edge sensor arrays with a superconducting quantum interference device", Appl. Phys. Lett. **86,** 112511 (2005).

[4] M. A. Dobbs, M. Lueker, K. Aird, A. Bender, L. Bleem, J. Carlstrom, et al., "Frequency multiplexed superconducting quantum interference device readout of large bolometer arrays for cosmic microwave background measurements", Rev. Sci. Instrum. **83,** 073113 (2012).

[5] B. D. Jackson, P. de Korte, J. van der Kuur, P. Mauskopf, J. Beyer, M. Bruijn, et al., "The SPICA-SAFARI Detector System: TES Detector Arrays With Frequency-Division Multiplexed SQUID Readout", IEEE Trans. Terahertz Sci. Technol. **2,** 12–21 (2012).

[6] R. den Hartog, J. Beyer, D. Boersma, M. Bruijn, L. Gottardi, H. Hoevers et al., "Frequency Domain Multiplexed Readout of TES Detector Arrays With Baseband Feedback", IEEE Trans. Appl. Supercond. **21,** 289-293 (2011).

[7] K. D. Irwin, L. R. Vale, N. E. Bergren, S. Deiker, E. N. Grossman, G. C.Hilton, et al., "Time-division SQUID multiplexers", AIP Conf. Proc. **605,** 301–304 (2002).

[8] W. B. Doriese, J. A. Beall, S. Deiker, W. D. Duncan, L. Ferreira, G. C.Hilton, et al., "Time-division multiplexing of high-resolution x-ray microcalorimeters: Four pixels and beyond", Appl. Phys. Lett. **85,** 4762–4764 (2004).

[9] D. Prele, F. Voisin, M. Piat, T. Decourcelle, C. Perbost, C. Chapron, et al., "A 128 Multiplexing Factor Time-Domain SQUID Multiplexer", J. Low Temp. Phys. **184,** 363–368 (2016).

[10] K. D. Irwin and K. W. Lehnert, "Microwave SQUID multiplexer", Appl. Phys. Lett. 85, 2107–2109 (2004).

[11] J. A. B. Mates, G. C. Hilton, K. D. Irwin, L. R. Vale, and K. W. Lehnert, "Demonstration of a multiplexer of dissipationless superconducting quantum

interference devices", Appl. Phys. Lett. **92,** 023514 (2008).

[12] Y. Nakashima, F. Hirayama, S. Kohjiro, H. Yamamori, S. Nagasawa, A. Sato, et al., "Low-noise microwave SQUID multiplexed readout of 38 x-ray transition-edge sensor microcalorimeters", Appl. Phys. Lett. **117,** 122601(2020).

[13] H. Akamatsu, D. Vaccaro, L. Gottardi, J. van der Kuur, C. P. de Vries, K. Ravensberg, et al., unpublished work (2021).

[14] L. Gottardi, K. Nagayashi, "A Review of X-rayMicrocalorimeters Based on Superconducting Transition Edge Sensors for Astrophysics and Particle Physics", Appl. Sci. **11,** 3793 (2021).

[15] D. Schwan, P. A. R. Ade, K. Basu, A. N. Bender, F. Bertoldi, H.-M. Cho, et al., "Millimeter-wave bolometer array receiver for the Atacama pathfinder experiment Sunyaev-Zel'dovich (APEX-SZ) instrument", Rev. Sci. Instrum. **82,** 091301 (2011).

[16] J. Montgomery, A. J. Anderson, J. S. Avva, A. N. Bender, M. A. Dobbs, D. Dutcher, et al., "Performance and characterization of the SPT-3G digital frequency multiplexed readout system using an improved noise and crosstalk model", Proc. SPIE **114530X** (2020).

[17] H. Logan, "The POLARBEAR-2 Cryogenic Receiver for Cosmic Microwave Background Polarization Science", Ph.D. thesis, University of California, San Diego (2019).

[18] G. Signorelli, A. Baldini, C. Bemporad, M. Biasotti, F. Cei, V. Ceriale, et al., "A 16 channel frequency-domain-modulation readout system with custom superconducting LC filters for the SWIPE instrument of the balloon-borne LSPE experiment", Nucl. Instrum. Methods Phys. Res. A **824,** 184–186 (2016).

[19] A. Tartari, A. Baldini, F. Cei, L. Galli, M. Grassi, D. Nicolo, et al., "Development and Testing of the FDM Read-Out of the TES Arrays Aboard the LSPE/SWIPE Balloon-Borne Experiment", J. Low Temp. Phys **199,** 212–218 (2020).

[20] K. MacDermid, A. M. Aboobaker, P. Ade, F. Aubin, C. Baccigalupi, K. Bandura, et al., "The performance of the bolometer array and readout system during the 2012/2013 flight of the E and B experiment (EBEX)", Proc. SPIE. **9153,** 915311 (2014).

[21] M. Hazumi, P. A. R. Ade, Y. Akiba, D. Alonso, K. Arnold, J. Aumont,·et al., "LiteBIRD: A Satellite for the Studies of B-Mode Polarization and Inflation from Cosmic Background Radiation Detection", J. Low Temp. Phys. **194,** 443–452

(2019).

[22] G. Jaehnig, K. Arnold, J. Austermann, D. Becker, S. Duff, N. Halverson, et al., "Development of Space-Optimized TES Bolometer Arrays for LiteBIRD", J. Low Temp. Phys **199,** 646-653 (2020).

[23] P. R. Roelfsema, H. Shibai, L. Armus, D. Arrazola, M. Audard, M. D. Audley, et al., "Spica-a large cryogenic infrared space telescope: Unveiling the obscured universe", Publ. Astron. Soc. Aust. 35, E030 (2018).

[24] M. D. Audley, G. de Lange, J. R. Gao, B. D. Jackson, R. A. Hijmering, M. L. Ridder, et al., "The SAFARI detector system", Proc. SPIE. **107080K** (2018).

[25] M. L. Ridder, P. Khosropanah, R. A. Hijmering, T. Suzuki, M. P. Bruijn, H. F. C. Hoevers, et al., "Fabrication of Low-Noise TES Arrays for the SAFARI Instrument on SPICA", J Low Temp Phys. **184,** 60-65 (2016).

[26] Q. Wang, P. Khosropanah, J. van der Kuur, G. de Lange, M. D. Audley, A. Aminaei, et al., "Frequency division multiplexing readout of 60 low-noise transition-edge sensor bolometers", submitted to Appl. Phys. Lett. (2021).

[27] K. Mikko, G. Leif, and S. Hannu, "Two-stage locally linearized SQUID readout for frequency domain multiplexed calorimeter arrays", Supercond. Sci. Technol. **24,** 049501(2011).

[28] Q. Wang, P. Khosropanah, J. van der Kuur, G. de Lange, M. D. Audley, A. Aminaei, et al., "Electrical crosstalk of a frequency division multiplexing readout for a transition edge sensor bolometer array", Rev. Sci. Instrum. **92,** 014710 (2021).

[29] M. Kiviranta, "SQUID development: current status", Pixel-CTP meeting, Utrecht (2018).

[30] Q. Wang, M. Audley, P. Khosropanah, J. van der Kuur, G. de Lange, A. Aminaei, et al., "Noise Measurements of a Low-Noise Amplifier in the FDM Readout System for SAFARI", J. Low Temp. Phys. **199,** 817-823 (2020).

[31] The deposition of the Au layer was done using Electron Beam deposition in combination with in lift-off process. We use AZ-5214 image reversal photoresist for pattern definition and deposit first a 3 nm Titanium (Ti) layer for adhesion followed by 200 nm Au. The gap between TES and the Au structure is 10 um.

[32] The nominal parameter of C/V (heat capacity/volume) is 7 $J/(K \cdot m^3)$. The previous heat capacity is 4 fJ/K. After depositing 200 nm Au on area of 125 ×

125 μm^2, the current heat capacity is 26 fJ/K. Therefore, the heat capacity increase a factor of 6.5.

[33] The etching of Si_3N_4 legs are performed from the front side, which is usually takes 5 minutes. However, in this fabrication process, even we performed an 8 minutes etching, there is still some Si_3N_4 structure left in the legs. So the etching time is not long enough.

[34] E. Taralli, P. Khosropanah, L. Gottardi, K. Nagayoshi, M. L. Ridder, M. P. Bruijn, et al., "Complex impedance of TESs under AC bias using FDM readout system", AIP Adv. **9,** 045324 (2019).

[35] R Hijmering, R. den Hartog, M. Ridder, A. J. van der Linden, J van der Kuur, J. R. Gao, et al., "Readout of a 176 pixel FDM system for SAFARI TES arrays", Proc. SPIE **99141C** (2016).

Chapter 8
Conclusions

The study of far-infrared (FIR) radiation (30-300 μm) is essential to understand a wide range of cosmic questions, among which the evolution of galaxies, and the origins of stars and planets are interesting and important [1]. Since the Earth's atmosphere is opaque to FIR radiation, space-based observations are required, motivating the development of FIR space telescopes. In past decades, space telescopes like Herschel, Planck [2], and Spitzer [3] have shown very exciting outcomes. However, in those space applications, the detection sensitivity was limited by the background noise of the warm telescope. The next generation of FIR space telescopes is aiming for background-limited sensitivity by combining a large (>2 m) and cold telescope (<10 K) with instruments employing state-of-the-art sensitive detector arrays. The transition edge sensor (TES) is a very attractive choice for FIR space telescopes due to its high sensitivity and matureness. In the FIR, TES detectors are approaching the photon statistics limit, which means their performance is dominated by the fluctuations in the arrival rate of photons at the detector, and not by the intrinsic noise of the detectors themselves [4].

To increase the mapping speed and field of view, a TES bolometer array with thousands of pixels could be applied in planned FIR space applications such as SPace Infrared telescope for Cosmology and Astrophysics/SpicA FAR-infrared Instrument (SPICA/SAFARI) [5] and Origins Space Telescope (OST) [6]. Multiplexing techniques are essential to read out such large arrays especially, for space applications. Multiplexing limits the number of cold wires and, thus, minimizes the heat load on the cold stage, which is particularly vital for space telescopes, where the cooling power is limited by the available electrical power and the restrictions on the total mass.

Frequency division multiplexing (FDM) is one of the most appealing multiplexing techniques. Over the past decades, there have been many developments in FDM systems. However, a systematic study and development for TES bolometers FDM readout system is still missing. This thesis reports the study and development of the FDM readout system for TES bolometers. In

particular, many studies are based on the requirement of the former European Space Agency middle-level mission (ESA-M5) candidate SPICA/SAFARI. Some initial requirements for SAFARI are: (1) noise equivalent power (NEP) should reach 0.2 aW/$\sqrt{\text{Hz}}$; (2) the readout current noise level should be below 10 pA/$\sqrt{\text{Hz}}$; (3) the electrical crosstalk level should be lower than 0.1%. Although the SPICA/SAFARI mission was canceled recently (October 2020), our work for the FDM system is still valid for space applications that need a multiplexing readout for a large TES bolometer array (>1000 pixels).

A fundamental requirement of an FDM readout system is that the readout noise level should be lower than the noise from the detectors, which includes the intrinsic noise of the TES and signal from the sky. In the FIR bolometer for SAFARI, the current noise level of a TES bolometer is about 30 pA/$\sqrt{\text{Hz}}$, depending on the characteristics of the TES itself and where the TES is biased in its transition. Our FDM system consists essentially of inductor-capacitor (LC) filters, superconducting quantum interference devices (SQUIDs), a low noise amplifier (LNA), and a demultiplexer (DEMUX). The LC filters and SQUIDs operate at a cryogenic temperature, while the LNA and DEMUX work at room temperature.

We firstly study the noise from electronics at room temperature. In Chapter 3, to quantify the noise level from the warm electronics, we build a noise model based on the electrical circuit of our readout chain, which consists of the voltage noise from the DEMUX, and the current noise as well as the voltage noise from the LNA. Combining our proposed model with the measured experimental data, we extract the noise value of the warm electronics, which is low enough to read out our TES arrays. The noise model can be used to quantify the noise contribution from other warm electronics setups, which is an important method to check their performance.

In an FDM system, all the signals from TES detectors are summed up and amplified by the SQUID. The current noise referred to the SQUID input coil represents the total readout noise, which consists of the noise from the warm electronics and the SQUID. Therefore, it is essential to understand and optimize the SQUID performance during the operation. In Chapter 4, we introduce a calibration tone method to characterize the noise performance of the FDM readout system. With the help of the calibration tone method, we not only can quantify the noise level of an FDM system but are also able to have an optimized SQUID setting.

Electrical crosstalk (ECT) among pixels in an array is unavoidable when they are read out by an FDM system. It is essential to minimize the ECT. In Chapter 5, we have characterized and mapped the ECT of an FDM system with a 61-pixel TES bolometer array. By applying a small modulation to the AC bias voltage of one TES and measuring the crosstalk response in the current noise spectra of the others simultaneously, we have for the first time mapped the ECT level of 61 pixels with a nominal frequency spacing of 32 kHz in a 61×61 matrix and a carrier frequency ranging from 1 MHz to 4 MHz. In the ECT map, about 40 pixels out of 61 TES detectors show an ECT level of less than 0.4%. Only the adjacent pixels reach this level, and the ECT for the rest of the pixels is less than 0.1%. However, high ECT levels of up to 10% are also observed. In this case, the ECT is dominated by high mutual inductances, caused by the long coplanar wires in the same bundles. To mitigate this source of ECT, the coplanar wires should be replaced by microstrip wires in the array. The ECT map suggests that our FDM system with about 30 kHz frequency spacing can have a low enough ECT level for FIR instruments like SAFARI. Our results successfully demonstrate the low electrical crosstalk needed for space FDM technology.

As a successful FDM readout demonstration, the performance of detectors read out in multiplexing mode (all the pixels are measured simultaneously) should be the same as what is measured in single pixel mode. In Chapter 6, we demonstrate an FDM readout of a 60-pixel array by comparing the current-voltage (IV) curves and noise spectra of the TESs measured in single-pixel mode (SPM) and in multiplexing mode (MM). By replacing the single-stage SQUID with a two-stage SQUID, we decrease the readout noise level from ~20 pA/$\sqrt{\text{Hz}}$ to ~10 pA/$\sqrt{\text{Hz}}$. We also map the noise equivalent power (NEP) and the saturation power of the bolometers in both modes, where there are 43 pixels that show not more than 10% difference in NEP and 5% in saturation power when measured in SPM and MM. We have succeeded in reading out a TES with an NEP of 0.45 aW/$\sqrt{\text{Hz}}$ in the MM, which demonstrates the capability of reading out ultra-low noise TES bolometer arrays for space applications. We noticed that 17 pixels in the array show a different performance between SPM and MM due to high ECT levels, which could be solved by replacing coplanar wires with microstrips. We also find that many pixels cannot be biased lower than 70% in transition due to the too fast response of the TES, which can be solved by increasing the heat capacity of the TES.

In Chapter 7, we update the FDM setup described in Chapter 6 by replacing it with a new TES array, which has microstrip wiring and has TESs with a longer response time in order to reduce the ECT and also to allow operation at the preferred biasing points. Due to the nonuniformity of the available TES batch, we can only choose 43 TES bolometers for our FDM readout study. We have read out all these 43 pixels simultaneously in the frequency range 1-3.5 MHz. The measured noise spectrum is in good agreement with the simulated noise based on measured parameters from an impedance measurement, confirming that our TES is dominated by phonon noise. We have found that 38 TES pixels out of the 43-pixel TES array show an electrical crosstalk level of less than 1%, which is dominated by carrier leakage. The up to 10% high ECT reported in Chapter 5 is no longer present, since the mutual inductance is minimized by using the microstrip wiring in the array. By adding an Au structure in the TES, we have increased the response time of our TES by a factor of 20, which enables all the TESs to be biased lower than 50% in transitions. With a more uniform TES bolometer array and a larger readout bandwidth (up to 5 MHz), we can foresee our FDM reading out 130 pixels in one SQUID readout channel.

A brief outlook of our FDM readout system for now, for the next few years, and for the next decade is given in the following paragraphs.

1. The following steps are ongoing development of our FDM system:

(a) Study the stability of the FDM system by applying Allan variance analysis. Allan variance analysis of the time series data shows the stability of the measurement over time, with the lowest variance value corresponding to the highest system stability. In addition, a 1/f noise analysis is performed based on the frequency series data. With the use of Allan variance and 1/f analysis, we could discover the most and least stable components of the FDM system. Knowing this we can improve the overall system stability and determine the best integration time for observing with TES arrays.

(b) Measurement and analysis of out-of-band resonances (OBR) in the readout chain up to 500 MHz. OBR could constrain the bandwidth of the FDM readout of the bolometers. In particular, OBR can be caused by the long harness (~5 m) for the flight model.

(c) Optical measurement of TES bolometers array-FDM system. By adding a feedhorn array in combination with an optical source, we could measure optical signals with the FDM readout system. This measurement can help

characterize the optical cross-talk of the readout system and eventually toward a full demonstration of an FDM system for space applications.

2. In the next years, some improvements to the FDM system should be performed:

(a) Have a precise resonance frequency of each LC filter. The main cause for deviations of the designed resonance frequency is a non-uniform distribution of capacity, formed during dielectric deposition. We should improve the fabrication process of the LC filters.

(b) Build an automatic measurement and analysis system based on Python. We have a standard measurement and analysis process. It is wise to package all those programs into a system, which is more effective for the measurement and analysis of thousands of TES bolometer arrays.

3. Until now, we have demonstrated an FDM system to read out TES bolometers of the order of 100 pixels in one readout chain. However, for future space applications like OST, thousands of TES pixels need to be read out. Thus, dozens of such readout chains must operate in parallel to read out such a large array. Therefore, in the next decade, the design and measurement of multiple FDM readout chains is needed.

References

[1] D. Farrah, K. E. Smith, D. Ardila, C. M. Bradford, M. J. DiPirro, C. Ferkinhoff, et al., “Review: far-infrared instrumentation and technological development for the next decade”, J. Astron. Telesc. Instrum. Syst. **5**, 1– 34 (2019).

[2] D. Doyle, G. Pilbratt and J. Tauber, "The Herschel and Planck Space Telescopes", Proc. IEEE, **97,** 1403-1411 (2009).

[3] M. W. Werner, T. L. Roellig, F. J. Low, G. H. Rieke, M. Rieke, W. F. Hoffmann, et al., “The Spitzer Space Telescope Mission”, Astrophys. J., Suppl. Ser. **154,** 1 (2004).

[4] M. A. Dobbs, M. Lueker, K. A. Aird, A. N. Bender, B. A. Benson, L. E. Bleem, et al., "Frequency multiplexed superconducting quantum interference device readout of large bolometer arrays for cosmic microwave background measurements", Rev. Sci. Instrum. **83,** 073113 (2012).

[5] P. R. Roelfsema, H. Shibai, L. Armus, D. Arrazola, M. Audard, M. D. Audley, et al., “Spica-a large cryogenic infrared space telescope: Unveiling the obscured universe”, Publ. Astron. Soc. Aust. **35,** E030 (2018).

[6] M. Meixner, L. Armus, C. Battersby, J. Bauer, E. Bergin, A. Cooray, et al., “Overview of the Origins Space telescope: science drivers to observatory requirements”, Proc.SPIE. **106980N** (2018).

Nederlandse samenvatting

"Hoe is de sterrenhemel ontstaan?". Deze vraag houdt de mensheid al eeuwenlang bezig. Zelfs nu, met moderne theoretische modellen en geavanceerde astronomische waarneemtechnieken, zijn er nog veel vragen over de ontstaansgeschiedenis van het heelal. In lijn met de vraag over het ontstaan van het heelal is het ook belangrijk om de ontstaansgeschiedenis en evolutie van sterrenstelsels en sterren te begrijpen. Volgens de Big-Bang theorie en sterrenkundige waarnemingen, is het heelal 13.8 miljard jaar geleden ontstaan. Om naar de ontstaansgeschiedenis van het heelal te kijken, moeten we dus terugkijken in het verleden. Door roodverschuiving kan het zichtbare licht uit het verleden nu gedeeltelijk worden waargenomen in het ver-infrarood golflengte gebied (Far-InfraRed, FIR) met golflengtes tussen 30-300 μm. Het ver-infrarood bevat daarmee essentiële informatie om vragen te beantwoorden over de oorsprong van het heelal.

Aangezien onze dampkring niet transparant is voor ver-infrarood licht, kunnen er in dit golflengtegebied geen waarnemingen op aarde worden gedaan. Gebruik van ver-infrarood ruimtetelescopen is dus noodzakelijk. Voor het waarnemen van de zwakke signalen wordt gebruik gemaakt van ultra-gevoelige sensoren die worden afgekoeld tot milli-kelvin temperaturen. Voor het maken van een beeld is het ook nodig om veel pixels te kunnen gebruiken, vergelijkbaar met een camera in een mobiele telefoon.

De in dit proefschrift beschreven sensoren zijn Transition Edge Sensors (TES). Dit zijn supergeleidende detectoren die gebruik maken van de sterke toename in weerstand in een supergeleider als functie van temperatuur. In een TES bolometer wordt de temperatuurverandering veroorzaakt door de energie van het binnenkomende ver-infrarood licht. De temperatuursverandering door de invallende fotonen zorgt voor een verandering in weerstand, die uiteindelijk wordt gemeten als een verandering in de stroom door de sensor.

De uitdagingen voor de ontwikkeling van TES detectoren voor een ruimtevaartmissie zijn niet alleen de ultieme gevoeligheid, maar ook de multiplex uitlees-elektronica. Zonder multiplexing zou elke sensor enkele draden nodig hebben om te worden aangestuurd en uitgelezen. Veel pixels zou dan ook veel bedrading inhouden, en dat is niet verenigbaar met de benodigde milli-kelvin temperaturen en het beperkte koelvermogen op deze lage temperatuur.

Gevoelige TES bolometers in combinatie met multiplex uitlees-elektronica zijn een optie voor een aantal toekomstige ver-infrarood en sub-millimeter ruimte-missies, zoals LiteBIRD (Lite satellite for the studies of B-mode polarization and Inflation from cosmic background Radiation Detection) geleid door JAXA (Japan Aerospace Exploration Agency), OST (Origin Space

Telescope) geleid door NASA (National Aeronautics and Space Administration), en SPICA (SPace Infrared telescope for Cosmology and Astrophysics) geleid door de European Space Agency (ESA) en JAXA. Helaas heeft ESA de SPICA-missie onlangs geannuleerd.

Frequency Division Multiplexing (FDM) is een heel aantrekkelijke multiplex technologie. Gedurende de laatste twee decennia is er veel ontwikkeling geweest op het gebied van TES detectoren en FDM systemen, maar een systematische experimentele demonstratie van FDM uitleeselektronica met TES bolometers is nog niet gedaan. Dit proefschrift beschrijft de eerste experimenten waarin dit wel gedaan wordt.

Mijn proefschrift beschrijft vijf onderzoeksprojecten, die zich richten op de systematische opbouw van een prototype uitlees systeem. Het FDM systeem is opgebouwd uit een aantal basis elementen; de inductie-capaciteits filters (LC-filters), Superconducting Quantum Interference Devices (SQUIDS), een Low-Noise Amplifier (LNA) en een demultiplexer (DEMUX). De LC filters en SQUIDs werken bij cryogene temperaturen, de LNA en DEMUX werken bij kamertemperatuur. Een basis vereiste voor de uitleeselektronica is dat de ruis van de elektronica lager is dan uitgangsruis van de detectoren. De ruis van de detectoren is opgebouwd uit intrinsieke detector ruis en foton ruis van het gedetecteerde signaal.

In Hoofdstuk 3 worden de resultaten gepresenteerd van het onderzoek naar de ruis van de warme elektronica. Voor het bepalen van de ruisbijdragen in de elektronica heb ik een ruismodel gemaakt, gebaseerd op de spanningsruis van de DEMUX en de spannings- en stroomruis van de LNA. Op basis van een vergelijking van dit model met gemeten data is de ruisbijdrage van de warme elektronica bepaald, en deze blijkt laag genoeg om arrays van TES detectoren uit te lezen. Het gebruikte ruismodel kan ook worden gebruikt voor andere uitleeselektronica, en is een belangrijke controle voor de werking van de elektronica.

In een FDM system worden de signalen van de TES detectoren samengevoegd en versterkt met een SQUID versterker. De equivalente totale stroomruis aan de ingang van de SQUID versterker is opgebouwd uit de ruis van de warme elektronica en de ruis van de SQUID. Het is dus essentieel om een goed begrip te hebben van de SQUID instellingen, en deze te optimaliseren voor minimale ruisbijdrage. In Hoofdstuk 4 wordt een kalibratiemethode met behulp van een kalibratietoon beschreven, om de ruis van het totale FDM systeem te bepalen. Met behulp van deze methode kan ik niet alleen het ruisniveau van de uitleeselektronica bepalen, maar ook de instellingen van de SQUID optimaliseren.

Elektrische overspraak (Electrical Cross Talk, ECT) tussen verschillende pixels in een FDM systeem is niet te voorkomen. Het is belangrijk om deze overspraak te minimaliseren. In Hoofdstuk 5 heb ik de overspraak tussen

verschillende pixels in een TES bolometer array geanalyseerd en in kaart gebracht. Voor het merendeel van de pixels is de ECT verwaarloosbaar laag. Er zijn echter enkele pixels met veel overspraak. Dit wordt veroorzaakt door onderlinge inductie. Door het visueel in kaart brengen van de overspraak kon de oorzaak voor de overspraak worden aangegeven, en op basis hiervan ook een methode om dit verder te verbeteren. Deze experimenten tonen aan dat FDM technologie kan worden gebruikt voor het ontwikkelen van uitleeselektronica met lage overspraak niveaus.

Voor een succesvolle demonstratie van FDM moet het niet uit maken of een pixel individueel wordt uitgelezen (single-pixel mode), of dat meerdere pixels simultaan worden uitgelezen (multiplexing mode). In Hoofdstuk 6 beschrijf ik de resultaten van een FDM systeem in combinatie met een 60 pixel TES bolometer array, en vergelijk ik de stroom-spanningskarakteristieken (IV) en de ruisspectra van de TES gemeten in single-pixel mode (SPM) en mulitiplexing mode (MM). Door het vervangen van de eentraps SQUID versterker door een tweetraps SQUID versterker, is de ruis van de uitleeselektronica met een factor 2 verlaagd, hetgeen een aanzienlijke verbetering geeft in de uitlezing. Ik ben hiermee in staat geweest om de TES uit te lezen met een lage Noise Equivalent Power (NEP) in de MM uitlees modus. De laagst gemeten waarde van de NEP is 0.45 aW/$\sqrt{\text{Hz}}$. Dit toont aan dat ultra-lage ruis TES bolometer arrays kunnen worden uitgelezen met FDM uitleeselektronica.

In Hoofdstuk 7 beschrijf ik verbeteringen die zijn aangebracht in het FDM prototype zoals beschreven in Hoofdstuk 6. In deze nieuwe configuratie is het TES array vervangen door een recent gefabriceerd TES array dat gebruik maakt van TES detectoren met een langere tijdsconstante en microstrip bedrading. Hierdoor kan de TES op een beter biaspunt worden ingesteld, en wordt de ECT verder gereduceerd. Het gemeten ruisspectrum komt goed overeen met een gesimuleerd ruisspectrum dat is gebaseerd op de parameters die bepaald zijn door een TES impedantie meting. Dit toont aan dat phonon ruis de dominante ruis in deze TES detectoren is. Ongeveer 90% van de TES pixels hebben een verwaarloosbaar laag overspraak niveau. De hogere ECT zoals aangegeven in Hoofdstuk 5 wordt niet langer waargenomen doordat de mutule inductie is geminimaliseerd door het gebruik van de microstrip bedrading. Door gebruik te maken van een gouden structuur op de TES bolometer, is de tijdsconstante van de TES bolometer toegenomen met een factor 20. Dit maakt het mogelijk om alle TES detectoren in een optimaal bias punt in te stellen.

Met een verdere optimalisatie van de TES bolometer uniformiteit en een grotere bandbreedte voor de uitleeselektronica, is het aannemelijk dat de FDM elektronica 130 pixels met 1 SQUID uit kan lezen. Dit opent de mogelijkheid voor toepassing in toekomstige ruimte missies. Onze resultaten tonen aan dat de uitleeselektronica ruimschoots kan voldoen aan de eisen voor de Japanse

LiteBIRD missie en op langere termijn ook voor een mogelijke toepassing van FDM technologie in de OST missie van NASA.

Acknowledgement

Memories flashing in my mind when I start to write this acknowledgment. My four years of Ph.D. study at the University of Groningen (RUG) and Netherlands institute for space research (SRON) coming to the end now. During the last four years, there are so many things are memorable, including the happy time when a designed experiment is done, a good paper is published, and the hard time when the measurement facility is broken. However, today I just want to show my deep thanks to all the people who have helped me during my Ph.D. study. People always say "one has to be independent to obtain a Ph.D. degree", this is true, but in the meantime, help from others is also essential to finish the Ph.D. study, at least for me.

First, I would like to show my sincere appreciation to my supervisor, Prof. Floris van der Tak, for all the help and support during my Ph.D. study, especially for the detailed suggestions on my writing in both paper and thesis. As an astronomer, you have broadened my view of our universe and motivated me to build better astronomical instruments. Knowing the origin of the universe might be as hard as knowing oneself, thank you for helping me try to find the answer for both of them.

I would express my deepest appreciation to my daily supervisor Dr. Jian-rong Gao. It is an amazing and special journey to work with you during my Ph.D. study. During my paper and thesis writing, you have given me enormous support and help, which leads me to a higher level. I always remember your suggestions that "keep the general reader view in mind". Your diligence and patience working attitude are very impressive, setting a model for me in my future career. You always give me a kind hand in my life whenever I needed, it is such luck to have you to be my daily supervisor.

Next, I would like to thank my other daily supervisor Pourya Khosropanah for the excellent collaboration from Groningen to Utrecht. I am very grateful for your help and support in both theory and technique during my measurements as well as during my paper writing. It is a great experience to work together with you since I am not only can obtain a lot of knowledge in work but can also learn a wise attitude to life.

I would also like to show my thanks to all the colleagues in our compact but professional work team: Gert de Lange not only shares the latest information with me but also show me how to be a good leader, he is also very kindly help

me to translate my English abstract and summary to Dutch; Damian Audley gives me detailed help in my first experiment and valuable suggestions in my paper writing; Jan van der Kuur shares with me his professional knowledge in both theory and techniques; Amin Aminaei supports my measurements with his accurate simulations; Marcel Ridder provides great TES bolometers to me for all the measurements; Saad Ilyas provides me quality LC filters; Richard Hijmering guides me to learn the whole FDM system in my first-year study.

There is also one special person I want to thank: Lingyu Wang, she is the first person in RUG to give me the interview and offer, without her, I might miss the chance to come to the Netherlands.

In addition, I would like to thank the useful discussions and technique supports from my colleagues in SRON, including Emanuele Taralli, Hiroki Akamatsu, Davide Vaccaro, and Marcel Bruin. I am also grateful for the support from Kevin Ravensberg in the experiment set up and Marcel van Listenburg in the modification of the system.

I also appreciate the helpful suggestions and support on my lab work from Willem-Jan Vreeling, Axel Detrain, and Dick Boersma. My special thanks also goes to SRON Secretaries and support groups (including Alie Hut, Bert Kramer, Bert Vunderink, Engelien van de Bunte, Jarno Panman, Petra Huizinga, Jens Johansen, Simon Rosmanand, Regina Lennaerts ...) as well as all the other colleagues in both SRON Groningen and Utrecht (including Jan Geralt bij de Vaate, Pieter Dieleman, Russell Shipman, Peter Roelfsema, Edgar Castillo, Ronald Hesper, Jose Silva, Matvey Finkel, Kirill Rudakov, Fangyou Gao, Anqi Li ...) for your help and support during the last four years.

I would also like to show my deep thanks to Lucia van der Voort, Inga Kamp, and my PhD mentor Marc Verheijen, without your help, I cannot going so smoothly during my PhD period.

My deep appreciation also goes to my family and my friends for their encouragement and support all through my studies, without their support I cannot even come to the Netherlands.

Finally, I would like to express my deepest love and special appreciation to my colleague as well as my wife Yuner Gan for accompanying and support me through not only this four-year Ph.D. study but also the seven-year journey since my master's study. It is an amazing and memorable experience to have the defense and obtain a Ph.D. degree on the same day as you, which I will tell our kids in the future.